INFORMATION TO USERS

This manuscript has been reproduced from the microfilm master. UMI films the text directly from the original or copy submitted. Thus, some thesis and dissertation copies are in typewriter face, while others may be from any type of computer printer.

The quality of this reproduction is dependent upon the quality of the copy submitted. Broken or indistinct print, colored or poor quality illustrations and photographs, print bleedthrough, substandard margins, and improper alignment can adversely affect reproduction.

In the unlikely event that the author did not send UMI a complete manuscript and there are missing pages, these will be noted. Also, if unauthorized copyright material had to be removed, a note will indicate the deletion.

Oversize materials (e.g., maps, drawings, charts) are reproduced by sectioning the original, beginning at the upper left-hand corner and continuing from left to right in equal sections with small overlaps.

Photographs included in the original manuscript have been reproduced xerographically in this copy. Higher quality 6" x 9" black and white photographic prints are available for any photographs or illustrations appearing in this copy for an additional charge. Contact UMI directly to order.

Bell & Howell Information and Learning
300 North Zeeb Road, Ann Arbor, MI 48106-1346 USA
800-521-0600

UMI®

CONTROL OF ABNORMAL HEART RHYTHMS

BY
KEVIN HALL
DEPARTMENT OF PHYSICS
MCGILL UNIVERSITY, MONTREAL
FEBRUARY 1999

A THESIS SUBMITTED TO
THE FACULTY OF GRADUATE STUDIES AND RESEARCH
IN PARTIAL FULFULLMENT OF THE REQUIREMENTS
FOR THE DEGREE OF
DOCTOR OF PHILOSOPHY

To my parents for their everlasting love and support,
and to Lori, my best friend, who makes life more beautiful
and more fun than I ever could have imagined.

ABSTRACT

Abnormal heart rhythms are often associated with serious illness and sometimes cause death. A new strategy to control cardiac arrhythmias involves precisely-timed electrical stimulation of the heart in an attempt to restore normal dynamics. In the first part of this thesis, I demonstrate that a particular abnormal heart rhythm is caused by a period-doubling bifurcation. I describe a new control technique that suppresses the abnormal rhythm by directing the timing of electrical stimuli according to a simple feedback algorithm. Subsequent analysis of the feedback controller revealed a rich structure of stability zones that can be used for automatic adaptation of the previously fixed feedback gain parameter.

While electrical stimulation of the heart guided by feedback control is a promising new treatment, the standard means of controlling an abnormal heart rhythm involves accurate diagnosis of the arrhythmia mechanism followed by appropriate medical or surgical intervention. Since different arrhythmia mechanisms often have very different treatments, accurate diagnosis is crucial. In the second part of this thesis, I describe a new diagnostic technique that identifies the different spatio-temporal symmetry properties of electrical wave patterns underlying different mechanisms of cardiac arrhythmia. For one of the arrhythmia mechanisms, the surgical treatment involves locating and destroying an abnormal region of the heart that generates unwanted electrical oscillations. I present new techniques for locating these abnormal regions and I suggest a procedure to confirm when the correct location has been found.

RÉSUMÉ

Les anomalies du rythme cardiaque sont souvent asssociées à des troubles graves et peuvent être mortelles. Une nouvelle stratégie de contrôle des ces arythmies met en jeu des stimulations électriques précisément minutées, dans le but de restorer une dynamique normal. Dans la première partie de cette thèse, je démontre qu'un type particulier d'anomalie du rythme cardiaque est associé à une bifurcation de doublement de période et je décris une nouvelle technique de contrôle qui permet de supprimer le rythme anormal en réglant le moment des stimulations électriques conformément à un algorithme de rétrocontrôle simple. L'analyse subséquente du mécanisme de rétrocontrôle a révélé une grande richesse structurale des zones de stabilité, qui peut être utiliées pour l'adaptation automatique du paramètre de gain du rétrocontrôle précédemment fixé.

Tandis que la stimulation électrique du cœur guidée par rétrocontrôle est un nouveau traitement prometteur, les moyens standard de contrôle des rythmes cardiaques anormaux impliquent un diagnostic précis du mécanisme de l'arrythmie suivi d'une intervention médicale ou chirurgicale appropriée. Les différents mécanismes d'arrythmie demandant souvent des traitements très différents, la précision du diagnostique est un point crucial. Dans la seconde partie de cette thèse, je décris une nouvelle technique de diagnostic qui permet d'identifier les propriétés de symétrie spatio-temporelle des ondes électriques sous-jacentes aux différents mécanismes d'arrythmie cardiaque. Pour l'un de ces mécanismes, le traitement chirurgical implique la localisation et la destruction d'une région anormale du cœur qui génère des oscillations électriques indésirables. Je présente des techniques nouvelles de localisation de ces régions anormales and je suggère une procédure permettant de confirmer l'exactitude de la localisation trouvée.

ACKNOWLEDGEMENTS

I wish to thank my supervisor, Leon Glass, who taught me to identify "cute" and "do-able" scientific problems. He has convinced me that the hardest part of science is asking the right questions. I thank him for his guidance and enthusiasm for the questions I have asked, and attempted to answer, in the years under his supervision.

I express my gratitude to professor Jan Huizinga and Dr. Louis Liu who introduced me to the science of physiology while I was an undergraduate physics student at McMaster University. Without their encouragement and contageous passion for biology, I may have ended up studying particle physics. I would also like to thank my undergraduate physics professor, Dr. Rajat Bhaduri, who wisely advised me to not read so much before attacking a new problem.

I would like to thank professor Jim Collins and Dr. David Christini for their productive collaboration and for introducing me to the field of dynamic control.

I thank Dr. Jacques Billette and Dr. Farid Amellal for introducing me to AV node physiology. I would like to thank professor Michael Mackey for his encouragement and professor Michael Guevara for his tough questions and stimulating conversations.

I would like to thank the students and post-docs at the Center for Nonlinear Dynamics who have made my time here more enjoyable: Tiger Nagai, Gil Bub, Arkady Kunysz, Caroline Haurie, Bhavna Khanna, Colin Hill, Kosta Vasilakos, Lars Petter Endresen, Caroline Chopra, Thomas Mestl, and Taishin Nomura.

I thank the Medical Research Council of Canada for their financial support.

PREFACE

In the course of my doctoral studies, I have benefited from collaborations with researchers trained in chemistry, medicine, physiology, engineering, and physics. Such a research environment provided me with unique interdisciplinary experiences and opportunities. But interdisciplinary research has its share of problems. For example, what journals are best suited for communicating research on controlling abnormal heart rhythms using tools from nonlinear dynamics and geometry? In considering that question, we thought that it was important to report each study to the most appropriate community - to cardiologists when our results could directly influence the interpretation or treatment of an arrhythmia; to physicists when our techniques involved symmetry arguments or dynamic control.

Communicating our results to both physicists and cardiologists has resulted in this manuscript-based dissertation that brings together the style, language, and conventions of both communities. Chapters 2 and 6 are based on papers that have been published in a cardiology journal, whereas chapter 3 has been published in a physics journal and chapter 5 is presently under review in a physics journal. Since this is a physics thesis, I have provided the necessary cardiology background in the Introduction.

Contributions by the various Authors

Chapter 2 is based on the manuscript **Alternation of Atrioventricular Nodal Conduction Time During Atrioventricular Reentrant Tachycardia: Are Dual Pathways Necessary?**, by F. Amellal, K. Hall, L. Glass, and J. Billette, *J. Cardiovasc. Electrophysiol.* **7** 943-951 (1996). All of the authors contributed to the design of the experimental protocols. The experiments were performed in Jacques Billette's laboratory by Farid Amellal with my assistance. I performed all of the data analysis, played a leading role in the interpretation of the results, and wrote the majority of the manuscript. I developed the model of AV nodal conduction presented in the Appendix to Chapter 2 which was not included in the original publication.

Chapter 3 is based on the text of **Dynamic Control of Cardiac Alternans**, by K. Hall, D. J. Christini, M. Tremblay, J. J. Collins, L. Glass, and J. Billette, *Phys. Rev. Lett.* **78**, 4518-4521 (1997). This study was motivated by a previous numerical study by David Christini and Jim Collins who suggested the experiments. I modified their control algorithm and Maurice Tremblay incorporated the new algorithm in an electronic stimulator. David Christini assisted me in the design of the experimental protocols. I performed the experiments in Jacques Billette's laboratory with the help of Karim Jalife, who dissected the rabbit hearts, and Lise Plamondon who provided technical assistance. I analyzed all of the data and wrote the majority of the manuscript.

Chapter 4 is based on a manuscript that is to be submitted for publication. I developed the theory and analyzed the intricacies of the experimental data from the previous chapter. The stability zones presented in this chapter were independently discovered by Joshua Socolar and Daniel Gauthier (J. E. S. Socolar and D. J. Gauthier, *Phys. Rev. Lett.* **79**, 4938 (1997)).

Chapter 5 has been submitted to *Physical Review Letters* and is currently under review. I developed the theory, performed the computer simulations, and wrote the manuscript under the supervision of Leon Glass.

Chapter 6 is based on the manuscript **Locating Ectopic Foci**, by K. Hall and L. Glass, in press *J. Cardiovasc. Electrophysiol.* (1999). I developed the theory, performed the computer simulations, and wrote the manuscript under the supervision of Leon Glass.

TABLE OF CONTENTS

CHAPTER 1
INTRODUCTION

Four weeks into the development of the human embryo, a small cluster of cells begin a cadence that will last a lifetime [1]. These immature cells will eventually form a heart that can beat more than one billion times - but when it fails, the result is deadly.

In addition to its obvious physiological importance, the heart was once thought to be the seat of the human soul, intellect, and emotion [1]. Thus, it is not surprising that this vital organ has been the subject of countless poets, philosophers, and physicians - but physicists have also been intrigued by the heartbeat and its complex rhythms. In particular, cardiac dynamics have been the focus of intensive study using techniques from the field of nonlinear dynamics [2]. Yet, despite the many cases of successful nonlinear analyses of the heartbeat, there has been little progress on the most clinically important problem: control of abnormal heart rhythms.

In this dissertation I hope to make a contribution to the growing field of cardiac control by attacking the problem along two lines: i) investigate the dynamics of an abnormal heart rhythm and devise a practical method to restore normal dynamics, and ii) exploit the spatio-temporal patterns of abnormal cardiac activation to improve diagnostic methods and locate abnormal sources of cardiac activity.

Background and Thesis Outline

1.1 The Normal Heartbeat

The heart is a four chambered pump. The left two chambers are responsible for pumping oxygen-rich blood to the body, while the right two chambers pump deoxygenated blood to the lungs where it is oxygenated. The upper two chambers, called the atria, assist in filling the cavities of the lower, more powerful ventricles.

The rate of the normal heartbeat is set by the transmembrane voltage oscillations, called action potentials, of cells in a small region of tissue called the sinoatrial (SA) node located at the top of the right atrium. For each heartbeat, the SA node

sends out a wave of electrical activity that propagates through the atria causing them to contract. The wave converges on a specialized structure called the atrioventricular (AV) node which is the only normal electrical connection between the atria and ventricles. The remainder of the boundary between the atria and the ventricles is composed of connective tissue which is fibrous and does not conduct electrical impulses. Conduction through the AV node is slow (5 cm/s compared to 100 cm/s in the atria). The slow conduction leads to a delay of 0.1 - 0.2 seconds between the activation of the atria and the ventricles. This delay allows for complete filling of the ventricles thereby improving the heart's pumping efficiency. The massive ventricles are subsequently activated nearly synchronously via rapid conduction of the cardiac impulse through the Purkinje fibre network extending throughout the ventricles.

When the above sequence of electrical events is disrupted, the heart has an abnormal rhythm or an "arrhythmia". Depending on the mechanism of the arrhythmia, the pumping capacity of the heart can be impaired to such an extent that the patient's life may be in jeopardy [3].

1.2 Abnormal Heart Rhythms as a Dynamical Disease

Cardiac arrhythmia is an example of a "dynamical disease" [4] where healthy dynamics are replaced by diseased dynamics because of a change in one or more physiological control parameters. For example, a reduction of blood supply to the heart muscle (myocardial ischemia) can change a normal region of the heart into a rapidly firing spontaneous pacemaker that causes the heart to beat too fast (tachycardia) [3]. In order to understand the origin of abnormal heart rhythms, researchers are developing realistic biophysical models of the heart's electrical activity. The hope is that such models will not only elucidate the mechanisms of disease-causing bifurcations, but also suggest therapies to restore normal dynamics.

1.3 Models of the Heart's Electrical Activity

An early theoretical model of the heart's electrical activity was published in 1928 by van der Pol and van der Mark who likened the heartbeat to an electric circuit whose resistance has a nonlinear dependence on the current [5, 6]. The peculiar "relaxation oscillation" of the system is characterized by a periodic slow storage of energy followed by its rapid release - a pattern that resembles the electric potential across the membrane of a cardiac pacemaker cell [7].

Relaxation oscillators are reminiscent of the heartbeat because of their unique response to external periodic forcing [5, 8].The amplitude of the forced oscillation is relatively insensitive to the frequency of forcing, unlike the well known resonance properties of linear oscillators, and the relaxation oscillation can be entrained to the forcing period for a wide range of forcing frequencies. Since the heartbeat was known to have similar entrainment properties when subjected to periodic electrical stimulation [8], van der Pol suggested that the heart is composed of coupled relaxation oscillators. By coupling three relaxation oscillators together, corresponding to the atria, AV node, and the ventricles, van der Pol and van der Mark were able to mimic the normal heartbeat as well as several clinically observed arrhythmias [6]. Their seminal study paved the way for mathematical modeling in cardiology.

It was soon realized that the underlying mechanism of the heart's relaxation oscillation is the flow of ions through various specialized channels in the cell membrane. The conductance of an ion channel is a nonlinear function of the transmembrane voltage, and each channel only allows the flow of a specific type of ion. Biophysical models of cardiac electrical activity [9] were developed based on Hodgkin and Huxley's Nobel prize winning study of the ionic currents involved in the generation of action potentials in the squid nerve [10]. However, unlike the squid nerve, where only two types of ions (sodium and potassium) are responsible for the principal currents, the heart has many more currents and the resulting mathematical models are very complex – sometimes involving more than 20 coupled nonlinear ordinary differential equations. The daunting complexity of modern biophysical models is believed to reflect the inherent intricacies of the cardiac cell.

1.4 Low-Dimensional Dynamics of the Heartbeat

Despite the complexity of the underlying physiology, the dynamics of the heartbeat can often be described by low-dimensional maps that can be measured experimentally. For example, Guevara *et al.* [11] used an experimentally measured one-dimensional map to predict the complex dynamics of spontaneously beating embryonic chick ventricular cell aggregates in response to periodic electrical stimulation.

Why does this experimental system have low-dimensional dynamics? Although the transmembrane voltage oscillation of a cardiac pacemaker cell is described by many coupled nonlinear ordinary differential equations, the attractor in these equations is a limit cycle. The behavior of a limit cycle oscillation in response to periodic forcing can often be described by an experimentally measurable one-dimensional map as follows.

An isolated perturbation of a limit cycle oscillation alters the timing of the rhythm so that it is shifted relative to an unperturbed oscillation. The magnitude of the phase shift depends on the timing of the perturbation as well as its amplitude. For a fixed amplitude b, the phase shift can be measured as a function of the time when the perturbation was delivered. If the period of the spontaneous rhythm is T_0 then the phase of the oscillation is: $\phi = t/T_0 \bmod 1$, where t is the time since some marker event that defines $\phi = 0$. If a perturbation is applied at a phase ϕ_0, then the resulting phase shift can be measured by examining the timing of subsequent beats relative to where they would have occurred in the absense of a perturbation. If the perturbed rhythm is advanced in time by an amount Δt (after transients have dissipated), then the phase of the rhythm is reset to a new phase ϕ_1 given by: $\phi_1 = \phi_0 + \Delta t/T_0$. Thus, by measuring the time shifts for stimuli applied at different phases ϕ_0, we obtain the so-called phase resetting curve:

$$\phi_1 = g(\phi_0, b) \tag{1.1}$$

for a fixed stimulus magnitude b.

If we assume that the system quickly relaxes back to the limit cycle after a pertur-

bation, then the phase of the oscillation shortly after a perturbation is approximately equal to ϕ_1. Thus, if stimuli are delivered periodically with a period τT_0, then the second stimulus arrives at a phase $\phi_1 + \tau = g(\phi_0, b) + \tau$, and the arrival phases of all subsequent stimuli are given by the map:

$$\phi_{n+1} = g(\phi_n, b) + \tau, \tag{1.2}$$

where ϕ_{n+1} is the arrival phase of the $n+1$ stimulus.

By measuring the phase resetting curve g using isolated stimuli of amplitude b, and given the initial stimulus phase ϕ_0, the one-dimensional map (1.2) predicts the dynamics of the limit cycle oscillation in response to periodic stimulation. The map is effective for a range of stimulation periods long enough so that the system has time to relax back to the limit cycle between successive stimuli.

Experimental observations of phase resetting and entrainment of the electrical oscillations in aggregates of embryonic chick ventricular cells confirm that the dynamics of the system are well described by the one-dimensional map (1.2) [11]. The map exhibits complex bifurcations and chaos that have been observed in the cardiac experiments.

Other examples of low-dimensional cardiac dynamics include the propagation of electrical impulses in Purkinje fibres and ventricular muscle [12], as well as atrioventricular conduction rhythms [13] - all of which can be approximated by experimentally measured one-dimensional maps.

1.5 Dynamic Control Techniques

Traditional control techniques utilize a system's governing equations to control the dynamics [14]. Such techniques work well when the system under control is a mechanical or electronic device whose governing equations are derived from first principles using well-known physical laws. But since the heart is not man-made, the equations of cardiac biophysical models are necessarily based on incomplete information pieced together using ionic current measurements from many different experiments. New

types of ion channels are discovered routinely and the models quickly become outdated. Thus, traditional control techniques are ill-suited for the control of abnormal heart rhythms.

A new class of feedback control techniques [15, 16] could possibly be applied to control abnormal cardiac rhythms because they do not require explicit knowledge of the system's underlying equations. Although these techniques were originally designed for the control of low-dimensional chaos, they can also be applied to control nonchaotic dynamics [17, 18] and therefore may be applicable to low-dimensional cardiac rhythms.

1.5.1 OGY Control

In 1990 Ott, Grebogi, and Yorke (OGY) [15] developed a feedback control technique for the stabilization of unstable periodic orbits embedded in a low-dimensional chaotic attractor. I will describe how the OGY control technique applies to the one-dimensional map: $X_{n+1} = f(X_n, \lambda_n)$, where X_n is a measurable quantity and λ_n is an experimentally accessible parameter. The goal is to stabilize an unstable fixed point $X^* \equiv f(X^*, \lambda_0)$ by applying perturbations $\delta\lambda_n$ to the control parameter $\lambda_n = \lambda_0 + \delta\lambda_n$, where λ_0 is the unperturbed value of the control parameter. The magnitude of the perturbation is chosen to be proportional to the distance from the fixed point:

$$\delta\lambda_n = \frac{\alpha}{2}(X^* - X_n), \tag{1.3}$$

where α is a constant feedback gain parameter.

Notice that only α and X^* need to be specified in order to apply the algorithm. However, for the purpose of choosing α, the original OGY technique assumes that X^*, $\left(\frac{\partial f}{\partial X}\right)\Big|_{X^*} \equiv A$, and $\left(\frac{\partial f}{\partial \lambda}\right)\Big|_{\lambda_0} \equiv B$ are known. For stationary chaotic systems, these quantities can be determined by measuring the return map X_{n+1} versus X_n. The fixed point X^* intersects the identity line $X_{n+1} = X_n$ and because of the ergodic properties of chaotic systems, the system will eventually approach an arbitrarily small neighbourhood around X^*. When this happens, A can be measured by fitting a line

to return map points near X^*. If λ_0 is shifted to $\lambda_0 + \delta\lambda$, where $\delta\lambda$ is a small *constant* perturbation, then B can be measured by observing the new value of the fixed point.

In the vicinity of the fixed point the system is described by the linear map:

$$\xi_{n+1} = A\xi_n + B\delta\lambda_n, \tag{1.4}$$

where $\xi_n \equiv X_n - X^*$. Substituting (1.3) for $\delta\lambda_n$ gives:

$$\xi_{n+1} = (A - \frac{\alpha}{2}B)\xi_n. \tag{1.5}$$

The optimal value for the feedback gain parameter is $\alpha = 2A/B$ so that the next iterate of the map is directed to the fixed point. However, for α in the range:

$$\frac{2(A-1)}{B} < \alpha < \frac{2(A+1)}{B}, \tag{1.6}$$

the linear system (1.5) will approach the formerly unstable fixed point X^*. Since stabilization is only guaranteed for the linear system, the OGY algorithm is turned on only when the chaotic system wanders in the vicinity of the unstable fixed point where the linear approximation is valid.

1.5.2 Delayed Feedback Control

In order to apply the OGY algorithm, the value of the unstable fixed point X^* must be determined prior to initiation of the control. This requirement can be met for stationary chaotic systems where X^* can be identified in a pre-control learning phase. However, biological systems are typically nonstationary and the value of X^* may drift appreciably over the course of an experiment. Furthermore, in the case of nonchaotic dynamics, the system may not approach X^* before the control is initiated which makes it difficult to estimate.

In 1992 Pyragas [16] proposed a delayed feedback controller that does not require

X^* to be specified:

$$\delta\lambda_n = \frac{\alpha}{2}(X_{n-1} - X_n). \tag{1.7}$$

Notice that, like the OGY controller (1.3), the perturbations of the delayed feedback controller (1.7) go to zero as the system approaches the fixed point. The time delayed variable X_{n-1} increases the dimension of the system so that the two-dimensional linearized controlled system is:

$$\xi_{n+1} = (A - \frac{\alpha}{2}B)\xi_n + \frac{\alpha}{2}B\xi_{n-1}, \tag{1.8}$$

which stabilizes X^* when the feedback gain α is in the range:

$$-\frac{2}{B} < \alpha < \frac{(A+1)}{B}, \tag{1.9}$$

provided that $A < 1$.

The delayed feedback controller has the advantage that an unknown fixed point can be stabilized as long as α is in the range given by (1.9). This is advantageous because biological systems typically drift over time, and the location of a drifting fixed point can be tracked. However, this advantage comes at a price: the control technique can only stabilize fixed points where the slope of f at the fixed point is within the range $-3 < A < 1$.

1.6 Previous Studies of Cardiac Control

In 1992, Garfinkel *et al.* modified the OGY control algorithm [15] to control the irregular beating of a piece of rabbit heart [19]. This study, and a similar subsequent study controlling irregular dynamics in a rat brain [20], generated much controversy [17, 21]. One point of contention was whether or not the respective biological systems were, in fact, chaotic as claimed. Furthermore, it is unclear whether or not either study actually utilized the system's underlying dynamics for control. This problem stems from their modification of the OGY control technique that originally called

for small control interventions applied to some accessible experimental parameter. Rather, the biological control studies directly modified the variable they wanted to control.

Other control techniques have been applied to model cardiac systems [18, 21, 22], but most of these studies use an additive forcing term for control that would be difficult to incorporate in a real physiological experiment [22].

We chose to avoid these problems by controlling a nonchaotic cardiac rhythm, called an alternans rhythm, in a piece of rabbit heart. Unlike the previous biological control studies, the dynamics of this system can be well characterized and the control interventions were applied to an accessible experimental parameter. Furthermore, control of cardiac alternans has clinical implications since alternans rhythms are a risk factor for sudden death [23].

1.7 Alternans Rhythms

Alternans rhythms are a class of arrhythmias that are characterized by a sequential alternation of cardiac activity between two patterns. For example, the strength of the heart's mechanical contraction may follow a strong, weak, strong, weak sequence [24], the body surface measurement of the heart's electrical activity (i.e. the electrocardiogram or ECG) may give a signal that alternates between two different patterns [23, 25], or the shapes of sequential action potentials measured from a cardiac cell may alternate from one beat to the next [26].

Particularly intriguing is the observation that ECG alternans are sometimes observed prior to a dangerous arrhythmia called fibrillation. Fibrillation is caused by irregular electrical wave patterns resulting in uncoordinated and inefficient contractions of the heart. Some researchers have suggested that fibrillation is an example of spatio-temporal chaos [27]. Since alternans bear a striking resemblance to a period-doubled rhythm, it is tempting to hypothesize that fibrillation is achieved via a period-doubling cascade and that the observed alternans precursor is simply the first step in the bifurcation sequence [28]. However, there is little evidence to support such a hypothesis.

Nevertheless, there is good evidence suggesting that alternans rhythms are associated with cardiac electrical instability [29] and are a risk factor for sudden cardiac death [23]. Although alternans have been observed in a variety of cardiac preparations [24, 25, 26, 30], period-doubling is a possible unifying mechanism. But cardiologists do not usually associate alternans with a period-doubling bifurcation.

1.7.1 AV nodal Alternans

Alternation of the AV nodal conduction time is often observed during an arrhythmia that occurs in patients with an abnormal accessory electrical pathway connecting the atria and the ventricles in addition to the normal AV nodal connection [31]. In these patients an impulse can propagate normally through the AV node and backwards through the accessory pathway thereby re-exciting the atria and completing a self-exciting reentrant loop (Figure 1.1). This arrhythmia is called orthodromic AV reentrant tachycardia and, when the heart rate is fast enough, conduction through the AV node can alternate in a fast, slow, fast, slow pattern.

The AV nodal conduction time alternans have been attributed to alternating propagation between two parallel pathways [32]. The two pathways are believed to have different conduction properties: one pathway conducts faster than the other, but the slower pathway requires less time to recover between impulses. This implies that for slow heart rates, the fast pathway is the effective pathway since it delivers the cardiac impulse to the nodal output first. However, as the heart rate increases, the cardiac impulse eventually blocks in the fast pathway, due to a short recovery time, and the slow pathway becomes the effective pathway. If the conduction is slow enough then the next impulse may arrive at the atria late enough for the fast pathway to recover, and a fast, slow, fast, slow pattern would be observed.

To test for dual AV nodal pathways during a normal heart rhythm, the atria are electrically stimulated so that the recovery time of the AV node is progressively shortened. If the patient has dual AV nodal pathways then there is a discontinuous increase in the AV nodal conduction time as the effective pathway shifts from the fast to the slow pathway. This discontinuous jump in the measured AV nodal recovery

curve (i.e. the nodal conduction time versus the recovery time) is the clinical criterion for dual AV nodal pathways. Although recovery curves are not usually measured in people with alternating AV nodal conduction times during reentry, dual pathways are sometimes presumed to be the underlying cause.

However, a recent study by Sun *et al.* [33] proposed a mathematical model of AV nodal conduction that demonstrated conduction time alternans in a single pathway arising from a period-doubling bifurcation. The model incorporated experimental observations of how the AV nodal conduction time depends on the rate of the heartbeat. Careful experimentation has revealed that the AV nodal conduction time is determined by three rate-dependent functional properties: recovery, facilitation, and fatigue [34].

The recovery property refers to the observed increase in AV nodal conduction time with a decrease in the recovery time between impulses. The recovery time is usually assessed by the time interval between activation of the His bundle (the nodal output) and the next atrial activation (HA interval). When the recovery time is held fixed, the AV nodal conduction time is a decreasing function of the previous conduction time. This property is called facilitation and, along with the recovery property, accounts for the short-term dynamics of the AV node. The fatigue property is a superimposed slow increase in the AV nodal conduction time as the heart rate is increased.

When these rate-dependant properties were incorporated in a finite difference equation model of AV nodal conduction, Sun *et al.* observed that the AV nodal conduction time could alternate as a result of a period-doubling bifurcation.

So, the question is: Are dual pathways necessary for AV nodal conduction time alternans in a real heart, or are they caused by a period-doubling bifurcation? In Chapter 2, I will describe the results of our rabbit AV node experiments that were designed to answer that question by simulating the reentrant arrhythmia where AV nodal alternans are observed clinically. The retrograde propagation through the accessory pathway was mimicked using a protocol called fixed-delay stimulation. We detected when the cardiac impulse exited the AV node by placing an electrode at the output of the node called the His bundle. After a fixed time interval, corresponding to the desired retrograde accessory pathway conduction time, we stimulated the rabbit

heart at the top of the right atrium. By varying the fixed delay, we simulated accessory pathways with different conduction times and generated AV nodal conduction time alternans when the fixed delay was short enough. Like previous observations of cardiac alternans in other settings, the AV nodal alternans indicated electrical instability in our experiments.

We concluded that dual pathways were not the cause of the alternans in our experiments, but rather the alternans were likely caused by a period-doubling bifurcation. This implies that the dynamics are low-dimensional and that there exists an unstable period-1 fixed point between the alternating conduction times. Thus, it may be possible to stabilize the period-1 fixed point and suppress the alternans rhythm using a control technique like the ones previously described.

1.8 Control of Cardiac Alternans

In Chapter 3, I describe a feedback control technique that was used to suppress AV nodal conduction time alternans in the rabbit heart. Since the dynamics of the AV nodal alternans are described by a slowly-drifting one-dimensional map, the interpretation of the control interventions was clear: stabilization of a formerly unstable period-1 fixed point. Furthermore, our control study was the first example of biological control that adapted to system nonstationarities - a ubiquitous property of biological systems.

The control technique used in our experiments was a modified version of the delayed feedback control discussed above. The modifications were introduced as a result of biological limitations, but subsequent stability analysis of our control algorithm revealed a rich structure of new stability zones. In Chapter 4, I present the results of this analysis and show some examples from the experiments. Finally, I will use the structure of the stability zones to modify the control algorithm so that the feedback gain parameter is automatically adapted.

1.9 Other ways to Control Arrhythmias

Although dynamic control of cardiac arrhythmias is an exciting area of research, clinical implementation of such techniques has yet to be realized. Rather, present-day control of clinical arrhythmias involves accurate diagnosis of the arrhythmia mechanism followed by either medical or surgical intervention.

1.9.1 Diagnosis of Arrhythmia Mechanism

The mechanism of an arrhythmia can often be diagnosed on the basis of body surface measurements of the heart's electrical signal called an electrocardiogram [35]. Intensive study of these electrical signals over the past century has led to a beautiful set of interpretive techniques that are invaluable for the assessment of cardiac health. Indeed, clinical cardiac electrocardiography is one of the most widely-used and informative medical procedures.

However, sometimes different arrhythmia mechanisms produce indistinguishable surface electrocardiograms making it difficult to obtain a definitive diagnosis. More detailed information about the heart's electrical activity can be obtained by threading catheters through blood vessels and placing electrodes at strategic locations on the inner surface of the heart [36]. These electrodes are used to monitor local electrical activity and deliver electrical stimuli. Assessing the heart's response to electrical stimuli is called electrophysiological testing which can be used to assist arrhythmia diagnosis.

1.9.2 New Techniques for Arrhythmia Diagnosis

Despite the success of electrophysiological testing, some arrhythmia mechanisms remain difficult to distinguish. In Chapter 5 we suggest a new procedure that could be used to distinguish between two superficially similar arrhythmias that cause the heart to beat too fast (tachycardia): anatomical reentry and ectopic tachycardia. Since the treatments for these arrhythmias can be radically different, accurate diagnosis is crucial.

Ectopic tachycardia is caused by an abnormal (ectopic) region of the heart that generates rapid oscillatory activity. The resulting abnormal pacemaker region beats faster than the normal SA node pacemaker which becomes entrained to the faster rhythm. Therefore, the origin of the cardiac impulse shifts and the heart rate is set by the rate of the ectopic pacemaker.

Anatomical reentry is caused by an electrical impulse propagating in a circuitous pathway around an obstacle such as a valve, the opening to a blood vessel, or a piece of damaged tissue. Since the period of circulation is usually faster than the intrinsic rate of the SA node, the normal pacemaker is overdriven and a rhythm similar to ectopic tachycardia results.

Presently, diagnosis of the arrhythmia mechanism is based on the following empirical observations [36]: i) Initiation of ectopic tachycardia is often characterized by a gradual increase in heart rate, called "warm-up". Furthermore, the ectopic tachycardia may "cool-down" with a gradual decrease in heart rate before the tachycardia stops; ii) Unlike ectopic tachycardia, anatomical reentry can often be initiated and terminated by electrical stimulation.

Unfortunately, while these criteria are useful, they are not absolute. It is sometimes difficult to terminate reentry using electrical stimuli. Furthermore, terminating a rhythm with a stimulus doesn't necessarily imply a reentrant mechanism since pacemaker activity can also be terminated in this manner [38]. Also, the warm-up phenomenon upon initiation of ectopic tachycardia is sometimes not observed simply because the rhythm may be on-going. Furthermore, the cool-down phenomenon has been observed prior to termination of reentry [33, 37].

Thus, a new technique to differentiate these arrhythmias might improve the accuracy of diagnosis. In Chapter 5, I will present a new diagnostic procedure that identifies the arrhythmia mechanisms based on their different spatio-temporal activation patterns: reentry corresponds to a topological spiral pattern whereas an ectopic pacemaker produces a topological target pattern. In principle, the two patterns could be distinguished by using a large number of electrodes to map the activity on the heart's surface. However, such a procedure is neither practical nor desirable.

We suggest a method for discerning targets from spirals using only two electrodes.

We test the method in computer simulations of targets and spirals in a sheet of excitable media. Our method reveals the different spatio-temporal symmetry properties of topological targets and spirals by measuring local activity and delivering stimuli at two points in space.

1.9.3 Surgical Control of Etopic Tachycardia

If the cause of the tachycardia is an ectopic pacemaker, then the patient can be cured thanks to a recent advance in clinical cardiac electrophysiology. Once the location of the ectopic pacemaker is found, a catheter can be placed at the offending location and the abnormal tissue can be ablated by applying radiofrequency current through the electrode [36]. This process destroys the ectopic pacemaker and the SA node subsequently resumes its normal pacemaking activity.

The trick is finding the ectopic pacemaker. In principle, the localization strategy is simple: find the position that is activated the earliest since this site must correspond to the source of the rhythm. In practice, this requires a lengthy procedure where electrodes are dragged over the endocardial surface until an early activation site is found. The placement of electrodes is directed by a process of trial and error. As a result, it is often necessary to apply radiofrequency current at several early activation sites before targeting the ectopic focus [39].

In Chapter 6 we propose two new localization techniques that were used to locate a pacemaker in a computer simulation. Our techniques are based on the geometry of wave propagation in homogeneous isotropic excitable media. Since the heart is neither homogeneous nor isotropic, we used an iterative procedure to converge on the pacemaker source. Furthermore, we developed a confirmation strategy that could be used to check that the ablation electrode is at the correct location before applying radiofrequency current.

BIBLIOGRAPHY

[1] G.P. Davis, E. Park, *The heart: the living pump* (Torstar books, New York, 1984).

[2] L.Glass, P. Hunter, and A. McCulloch, eds. *Theory of Heart: Biophysics, Biomechanics and Nonlinear Dynamics of Cardiac Function* (SpringerVerlag, New York, 1991).

[3] D. Zipes and J. Jalife eds. *From Cell to Bedside: Cardiac Electrophysiology* (W. B. Saunders, Philadelphia, 1995).

[4] L. Glass and M. C. Mackey, *From Clocks to Chaos: The Rhythms of Life* (Princeton University Press, Princeton, 1988).

[5] B. van der Pol, Phil. Mag. **2**, 978 (1926).

[6] B. van der Pol and J. van der Mark, Phil. Mag. **6**, 763-775 (1928).

[7] M. H. Draper and S. Weidmann, J. Physiol. Lond. **115**, 74-94 (1951); T. C. West, J. Pharmacol. Exptl. Therap. **115**, 283- 290 (1955); H. Irisawa, Physiol. Rev. **58**, 461-498 (1978).

[8] For a review of early cardiac electrical pacing, see D. C. Schechter, New York State J. Med. **72**, 395-404 (1972).

[9] G. W. Beeler and H. Reuter, J. Physiol. **268**, 177- 210 (1977); D. DiFrancesco and D. Noble, Phil. Trans. Roy. Soc. Lond. B. **307**, 353-398 (1985); C. H. Luo and Y. Rudy, Circ. Res. **68**, 1501-1526 (1991); C. H. Luo and Y. Rudy, Circ. Res. **74**, 1071-1096 (1994); A. Nygren, C. Fiset, L. Firek, J. W. Clark, D. S. Lindblad, R. B. Clark, and W. R. Giles, Circ. Res. **82**, 63-81 (1998); M. Courtemanche, R. J. Ramirez, and S. Nattel, Am. J. Physiol. **275**, H301-321 (1998).

[10] A. L. Hodgkin and A. F. Huxley, J. Physiol. **117**, 500-544 (1952).

[11] M. R. Guevara, L. Glass, and A. Shrier, Science **214**, 1350-1353 (1981); M. R. Guevara and L. Glass, J. Math. Biol. **14**, 1-23 (1982).

[12] D. R. Chialvo, R.F. Gilmour Jr., and J. Jalife, Nature **353**, 653-657 (1990); D. R. Chialvo, D. C. Michaels, and J. Jalife, Circ. Res. **66**, 525-545 (1990).

[13] A. Shrier, H. Dubarsky, M. Rosengarten, M. R. Guevara, S. Nattel, and L. Glass, Circulation **76**, 1196-1205 (1987).

[14] N. S Nise, *Control Systems Engineering* (The Benjamin/Cummings Publishing Company, Inc., Redwood City, California, 1992), p. 630.

[15] E. Ott, C. Grebogi, and J. A. Yorke, Phys. Rev. Lett. **64**, 1196-1199 (1990).

[16] K. Pyragas, Phys. Lett. A **170**, 421-428 (1992).

[17] D. J. Christini and J. J. Collins, Phys. Rev. Lett. **75**, 2782-2785 (1995).

[18] D. J. Christini and J. J. Collins, Phys. Rev. E **53**, R49-R52 (1996).

[19] A. Garfinkel, M. L. Spano, W. L. Ditto, and J. N. Weiss, Science **257**, 1230-1235 (1992).

[20] S. J. Schiff, J. Jerger, D. H. Duong, T. Chang, M. L. Spano, and W. L. Ditto, Nature (London) **370**, 615-620 (1994).

[21] L. Glass and W. Zeng, Int. J. Bifurcation Chaos **4**, 1061-1067 (1994).

[22] M. E. Brandt and G. Chen, Biol. Cybern. **74**, 1-8 (1996); M. E. Brandt and G. Chen, Int. J. Bifurcation Chaos **6**, 715-723 (1996); M. E. Brandt, H. T. Shih, and G. Chen, Phys. Rev. E **56**, R1334-R1337 (1997); M. E. Brandt and G. Chen IEEE Trans. Circuits Systems **44**, 1031-1034 (1997).

[23] D. S. Rosenbaum, L. E. Jackson, J. M. Smith, H. Garan, J. N. Ruskin, and R. J. Cohen, N. Eng. J. Med. **330**, 235- 241 (1994).

[24] L. J. J. Muskens, J. Physiol. Lond. **36**, 104-112 (1907); A. C. Cushney, Heart **1**. 1-22 (1909).

[25] T. Lewis, Q. J. Med **4**, 141-144 (1910);

[26] J. B. Nolasco and R. W. Dahlen, J. App. Physiol. **25**, 191-196 (1968); M. R. Guevara, G. Ward, A. Shrier, and L. Glass, in *Computers in Cardiology*, IEEE Comp. Soc. (1984) pp. 167-170.

[27] G. V. Savino, L. Romanelli, D. L. Gonzalez, O. Piro, and M. E. Valentinuzzi, Biophys. J. **56**, 273-280 (1989); A. Garfinkel *et al.*, Circulation (Suppl. I) **90**, I541 (1994); J. Clin. Invest. **99**, 305 (1997).

[28] J. M Smith and R. J. Cohen, Proc. Nat. Acad. Sci. USA **81**, 233-237 (1984); A. L. Ritzenberg, D. R. Adam, and R. J. Cohen, Nature **307**, 159-161 (1984).

[29] J. M. Smith, E. A. Clancy, C. R. Valeri, J. N. Ruskin, and R. J. Cohen, Circulation **77**, 110-121 (1988).

[30] T. Lewis and G. C. Mathison, Heart **2**, 47-53 (1910);

[31] P. S. Barker, F. D. Johnston, and F. N. Wilson, Am. Heart J. **25**, 799-811 (1943); P. V. L. Curry and D. M. Krikler, (Abstract) Br. Heart J. **38**, 882 (1976); H. D. Friedberg and L. Schamroth, J. Electrocardiol. **6**, 159-163 (1973); R. L. Rinkenberger, E. N. Prystowsky, J. J. Heger, et al., Circulation **62**, 996-1010 (1980); R. Spurrell, D. Krikler, and E. Sowton, Br. Heart J. **35**, 113-121 (1973); R. J. Sung, and J. L. Styperek, Circulation **60**, 1464-1476 (1979); J. Vohra, D. Hunt, J. Stuckey, et al., Br. Heart J. **36**, 570-576 (1974); H. Wellens, S. L. Tan, F. Bar, et al., Br. Heart J. **39**, 1058-1066 (1977).

[32] C. Mendez and G. K. Moe, Circ. Res. **19**, 378-393 (1966); H. D. Friedberg and L. Schamroth, J. Electrocardiol. **6**, 159-163 (1973); R. Spurrell, D. Krikler, and E. Sowton, Br. Heart J. **35**, 113-121 (1973); R. J. Sung and J. L. Styperek, Circulation **60**, 1464-1476 (1979).

[33] J. Sun, F. Amellal, L. Glass, and J. Billette, J. Theor. Biol. **173**, 79-91 (1995).

[34] J. Billette and R. Metayer, Circ. Res. **65**, 164-175 (1989); J. Billette, R. Metayer, and M. St-Vincent, Circ Res **62**, 790-799 (1988).

[35] A. L. Goldberger and E. Goldberger, *Clinical Electrocardiography: a simplified approach* (Moseby, St. Louis, 1994) 5th ed.

[36] M. E. Josephson, *Clinical Cardiac Electrophysiology: Techniques and Interpretation* (Lea Febiger, Philadelphia, 1993), 2nd ed.; R. N. Fogoros, *Electrophysiologic Testing* (Blackwell Science, Cambridge, Mass., 1995), 2nd ed.

[37] M. B. Simpson, J. F. Spear, and E. N. Moore, Am. J. Physiol. **240**, H947-H953 (1981).

[38] J. Jalife and C. Antzelevitch, Science **206**, 695- 697 (1979); J. Jalife and C. Antzelevitch, Am. Heart J. **100**, 128- 130 (1980).

[39] D. W. Zhu, J. D. Maloney, T. W. Simmons, et al., J. Am. Coll. Cardiol. **26**, 843-849 (1995); J. A. Chiladakis, V. P. Vassilikos, T. N. Maounis, et al., PACE **20**, 953-959 (1997); M. D. Lesh, G. F. Van Hare, L. M. Epstein, et al., Circulation **89**, 1074-1089(1994); C. M. Tracy, J. F. Swartz, R. D. Fletcher, et al., J. Am. Coll. Cardiol. **21**, 910-917 (1993); E. P. Walsh, J. P. Saul, J. E. Hulse, et al., Circulation **86**, 1138-1146 (1992); H. Poty, N. Saoudi, M. Haissaguerre, et al., Am. Heart J. **131**, 481-489 (1996).

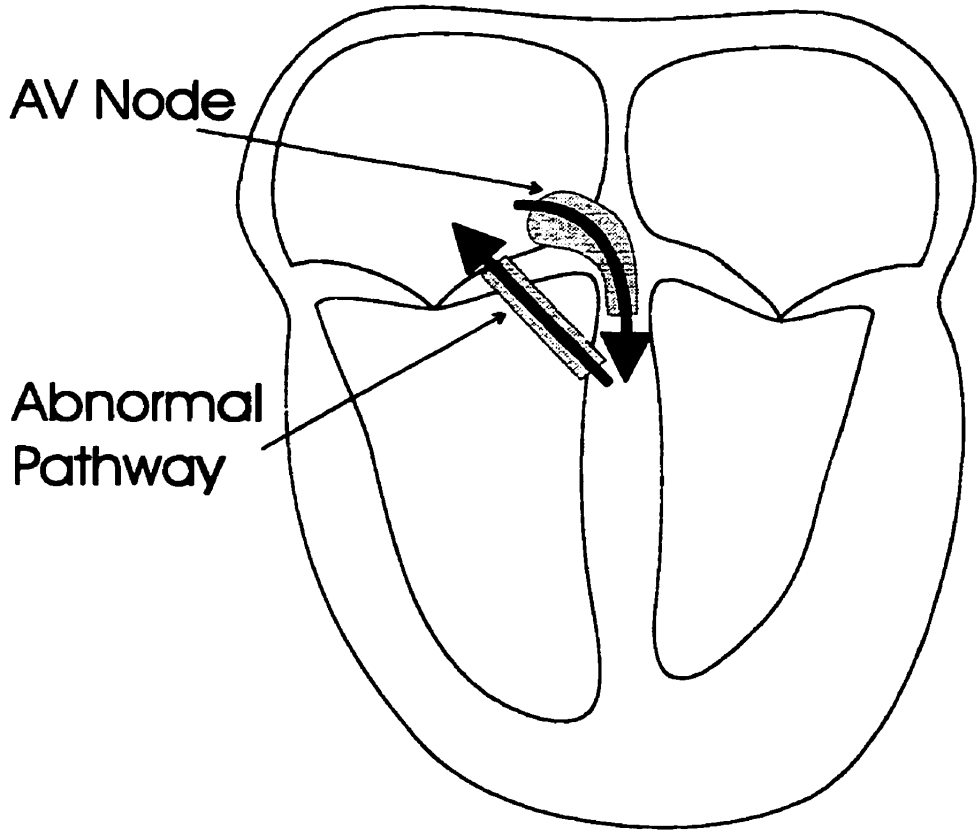

Figure 1.1: Schematic of orthodromic AV reentrant tachycardia. The dark arrows refer to the circulating reentrant cardiac impulse.

CHAPTER 2
ATRIOVENTRICULAR NODAL CONDUCTION TIME ALTERNANS

2.1 Foreward

Alternation of the atrioventricular nodal conduction time (NCT) is often observed during supraventricular tachycardia[1] [1, 2, 3, 4, 5, 6]. It is especially prominent near the termination of the tachycardia and therefore may reflect instability [2, 7, 8, 9, 10, 11, 12]. The alternation is enhanced in response to pharmacologic or hypoxic increases of AV nodal refractoriness [2, 4, 6, 13]. A typical example occurs in the orthodromic AV reentrant tachycardia associated with Wolff-Parkinson-White syndrome. The reentrant circuit of this tachycardia is composed of an antegrade pathway through the AV conduction system and a retrograde accessory AV bypass pathway [14]. Because the retrograde delay is nearly constant during this tachycardia, the cycle length alternation is clearly due to beat-to-beat changes in NCT. This sequential alternation of NCT has often been attributed to alternating conduction between dual AV nodal pathways [3, 5]. However, it has also been suggested that the alternation may arise solely from the functional properties of the AV node [4, 8, 11, 12]. In a recent study [12], we observed the NCT alternation in an in vitro rabbit heart model of AV reentrant tachycardia and proposed that the alternation resulted from the intrinsic dynamics of the AV node. The main goal of the present study was to further investigate the characteristics of the alternation and to elucidate its mechanism.

2.2 Methods

2.2.1 Preparation and Apparatus

The experiments were performed in six superfused isolated rabbit heart preparations. Animal care was conducted according to the guidelines of the American Physiological

[1] Supraventricular tachycardia refers to a rapid heart rate whose anatomical site of origin is above the ventricles.

Society and the University of Montreal. The preparation, perfusion system, stimulation techniques, and recording system were as previously described [15]. Briefly, the preparation (Figure 2.1A), including the right atrium, AV node area, and upper part of the ventricular septum, was mounted in a tissue bath. The bath was perfused at 200 mL/min with a 6-L volume of oxygenated (95% O_2, 5solution and maintained at 37° C and pH 7.38. Its composition (in mM) was 128.2 NaCl, 4.7 KCl, 2.0 $CaCl_2$, 1.0 $MgCl_2$, 20.0 $NaHCO_3$, 0.7 NaH_2PO_4 and 11.1 dextrose. A bipolar platinum-iridium stimulation electrode was placed on the crista terminalis near the sinus node. As indicated in Figure 2.1A, unipolar electrograms were recorded from the upper atrium (UA), low crista terminalis (CT), low interatrial septum (IAS) and His bundle (HIS). An additional electrogram (E) was recorded from the surface of the node. This electrode was positioned using a micromanipulator and visual control through a dissecting microscope. A similar nodal electrogram has recently been used to monitor intranodal activation [16]. All recording electrodes consisted of sharply cut, teflon insulated, 0.01" silver wires. The electrograms, stimulation pulses, a time code and a tachogram were digitized at a sampling rate of 5 kHz per channel and recorded on a video tape. The bandwidth was 0.1 Hz to 3 kHz. Stimulation intervals were generated with an accuracy of 1 ms and a precision of 0.47 μsec using a locally developed computer algorithm [17]. Stimulation pulses had voltages which were twice threshold and a duration of 2 ms. Data analysis was performed off- line.

2.2.2 Rabbit Heart Model of Orthodromic AV Reentrant Tachycardia

Since the retrograde accessory pathway has a nearly constant conduction time [14], the time interval between the His bundle activation and atrial activation is fixed. This implies that the retrograde pathway can be electronically mimicked by stimulating the atrium after a fixed delay from detecting the activation of the His bundle [8, 9, 11, 12]. This fixed HS interval stimulation protocol formed the basis of our in vitro model of orthodromic AV reentrant tachycardia and is schematically depicted in Figure 2.1B. The excitation propagates from the upper atrium to activate the low crista and low septum nodal inputs. The activation of the inputs triggers a

nodal response documented by a His bundle deflection. Each His-bundle activation is detected and the next stimulation is given with a predetermined HS. The retrograde delay of the accessory pathway is thus modeled by fixing the HS value.

2.2.3 Stimulation Protocols

After a 30-min stabilization period, the preparation was paced for 15 minutes at a rate which resulted in an atrial cycle length 30 ms shorter than that of the spontaneous sinus rhythm (SCL = 376 ± 43 ms, n=6). An incremental pacing protocol was performed to determine the HS which results in a nodal block. As illustrated in Figure 2.1C, the tachycardia was initiated by stimulating the atrium with a fixed HS (HSinit = 70 ± 22 ms, n=6) which was 30 ms longer than that which resulted in a nodal block during incremental pacing. This pacing rate was maintained for 5 min in order to establish a steady state NCT and cycle length. The HS was then progressively decreased by 2 ms steps, with each step being maintained for at least 1 min.

2.2.4 Interval Measurements

Activation times, defined by the negative peaks of the first time derivatives of the electrograms, were determined with 0.25 ms precision. This analysis was performed off line using Asyst acquisition software from Keithley and Data Pack analysis software from Run Technologies. Time intervals between the stimulation pulses, atrial electrograms, and His bundle activation were determined with 0.35 ms precision. Data is presented as mean ± standard deviation.

2.2.5 Definitions

The AV node includes the anatomical structures corresponding to the transitional, midnodal and lower nodal cells. The atrial reference site (A) was taken from the low interatrial septum. NCT refers to the time interval between the atrial activation and the following His bundle activation. The AV nodal functional properties of recovery,

facilitation and fatigue are as previously described [15, 18]. Briefly, the recovery property refers to the increase of the NCT with a decrease in nodal recovery time as assessed by the His-atrial (HA) interval. Facilitation refers to a decrease in the NCT for a given recovery time when the previous cycle is shortened. This effect is most pronounced for short recovery times. Fatigue is defined as a slow, rate-dependent increase of the NCT.

2.3 Results

2.3.1 Progressive Onset of Alternation

The alternation of both the cycle length and the NCT developed progressively with decreasing HS (Figure 2.2). In the illustrated example, the tachycardia resulting from a 60 ms HS gave a constant NCT and cycle length. As the HS was decreased to 56 ms, NCT increased due to a reduction of the nodal recovery time associated with this pacing rate. Since the decrease of HS was offset by the increase of the NCT, the cycle length remained virtually unchanged. As the HS was further decreased, a sequential alternation of progressively larger magnitude developed. Such a progressive onset of sequential alternation between two levels was observed in 4 out of 6 preparations. Since the retrograde delay was fixed and the atrial conduction time was constant, the NCT alternation accounted entirely for the cycle length alternation. Although the NCT alternation was usually quite small ($\Delta NCT_{max} = 4.6 \pm 0.5$ ms, n=4) and required high experimental precision to be detected, it was consistently observed and maintained for long periods of time.

2.3.2 Spontaneous Termination and Reinitiation of the Tachycardia

The HS decrease eventually resulted in a nodal block which temporarily terminated the tachycardia. Figure 2.3A and B show typical beat to beat NCT changes and corresponding electrograms, respectively. The termination was preceded by an increase in NCT alternation (Figure 2.3A and B). The last successful conduction through the AV node always corresponded to the lower branch of the alternation. Atrial stimula-

tion temporarily ceased due to the absence of a His bundle complex (Figure 2.3B). A spontaneous atrial beat (arrow) was generated after a time interval greater than the spontaneous sinus rhythm. The spontaneous atrial beat propagated to the His bundle with a short NCT and reinitiated the tachycardia. The next NCT was markedly prolonged, probably because of the absence of facilitation. The return of facilitatory effects at the next beat caused substantial NCT shortening. Subsequently, the NCT gradually increased and resumed its alternation with an increasing magnitude. The tachycardia persisted until another nodal block occurred. Such transient nodal blocks preceded by NCT alternation were observed in all but one preparation. In the latter, 1:1 nodal conduction persisted even at an HS of 0 ms.

2.3.3 Origin of NCT Alternation

In an attempt to localize the origin of the NCT alternation, we positioned an electrode (E) near the central area of the node (Figure 2.1). The E electrogram deflection was slower than atrial or His bundle deflections and occurred well after the last atrial activation. Using the E signal, the NCT could be divided into proximal (AE) and distal (EH) components. The AE reflected the contribution of the inputs to NCT [16]. Figure 2.4 shows the local dynamics shortly after a restarting of the tachycardia with a 40 ms HS. The gradual onset of NCT alternation is observed in the EH but not in the AE. Although the exact anatomical locus of the alternation can not be identified with precision, these results indicate that the site is distal to the E electrode and thus unlikely involves the inputs. Similar results were found in all but one of the preparations exhibiting alternation. The other case demonstrated a significant alternation in the morphology of the nodal electrogram (E), even for HS too long to induce NCT alternation. As a result, the proximal and distal intervals were observed to alternate oppositely even when the NCT was constant. This made it difficult to localize the region of the NCT alternation in this case.

2.3.4 Continuous Recovery Curves

Recovery curves were obtained at three basic cycle lengths in all preparations. In every case, the recovery curves were smooth and continuous, without breaks or jumps, as depicted for one preparation in Figure 2.5. Changes in the recovery curve with different basic cycle lengths are consistent with previous findings and reflect the AV nodal functional properties of facilitation and fatigue [15, 18].

2.3.5 Mathematical Modeling

A mathematical model quantifying the properties of AV nodal recovery and facilitation showed that, for the fixed HS stimulation protocols similar to those used in the present study, the NCT is a unique function of previous NCT, $NCT_{n+1} = f(NCT_n)$, when the level of fatigue is constant [12]. This means that we can plot a curve of possible beat-to-beat conduction times, NCT_{n+1} versus NCT_n (Figure 2.6A). By iterating this function starting at some initial value (NCT_1), we obtain the NCT sequence plotted in Figure 2.6B. Graphically, this iteration is performed by a process called cobwebbing and is illustrated in Figure 2.6A. Notice that there exists a NCT value where the curve intersects the identity line, $NCT_{n+1} = NCT_n$. This point, NCT^*, is called a fixed point because at this point $NCT^* = f(NCT^*)$. It turns out that when the slope of the curve is sufficiently shallow at the fixed point, the NCT sequence converges to it as shown in Figure 2.6A. In this case, NCT^* is called a stable fixed point. Therefore, a perturbation of the steady state would result in a damped alternation (Figure 2.6B) which relaxes to the stable fixed point value (NCT^*), as previously observed by Simpson et al [11].

The level of fatigue varied so slowly in our experiments that it did not produce appreciable changes in the NCT from one beat to the next. Therefore, the shape of the NCT_{n+1} versus NCT_n curve remains unchanged. However, the slow increase of fatigue will slowly moved the curve up and right in the manner depicted in Figure 2.7A. Notice that NCT^* slowly increases with increasing fatigue. Therefore, the observed NCT will gradually increase as shown in Figure 2.7B. If the fatigue increases enough, the slope of the curve at NCT^* will reach a critical degree of steepness (i.e. slope = -1)

where NCT^* becomes unstable (Figure 2.8A). When this happens, the observed NCT will no longer be NCT^* but will sequentially alternate between two values, NCT_1^* and NCT_2^*, one of which is larger than the fixed point value and the other is smaller. The resulting beat-to-beat alternation may be stable (Figure 2.8B) or may gradually increase with increasing fatigue (not shown).

2.4 Discussion

2.4.1 Mechanism of NCT Alternation

Cycle length alternation during AV reentrant tachycardia has often been attributed to alternating conduction between fast and slow AV nodal pathways [3, 5]. If such a mechanism were responsible for the sequential alternation of NCT, then one would expect the alternation to begin abruptly with a discontinuous jump caused by a shift of the conduction from fast to slow pathway [19]. This did not happen. We observed a gradual onset of NCT alternation with increasing magnitude (Figures 2.2, 2.3 and 2.5). This observation cannot be easily explained by the dual pathway theory.

Another finding was the continuity of the AV nodal recovery curves at all 3 basic cycle lengths studied (Figure 2.5). While a jump or break in the AV nodal recovery curve is the hallmark of dual pathway physiology in humans [19, 20], continuous recovery curves without breaks or jumps were found in all preparations. This observation rules out dual nodal pathway physiology as clinically defined. However, because reentry can occur in both human and rabbit heart without a discontinuity in the recovery curve [21], one may suggest that the absence of discontinuity does not in itself rule out the existence of dual pathways nor their involvement in the alternation. Nevertheless, our observation that the alternation was confined to the distal conduction time (Figure 2.4) makes it unlikely that dual nodal inputs are involved in this phenomenon. As suggested by the success of the ablation therapy for nodal reentrant tachycardia [20] and by other characteristics of nodal reentry [22], the inputs constitute the main component of the dual pathways. Therefore, it is unlikely that dual pathway physiology is responsible for the alternation in our preparations.

In a previous study [12], we proposed that the NCT alternation resulted from the intrinsic dynamics of the AV node. We showed that a mathematical model of the AV nodal functional properties could generate NCT alternation by a process called a period doubling bifurcation. As shown in Figures 2.6- 2.8, the period doubling mechanism is consistent with our present findings. This model predicts a gradual onset of NCT alternation with increasing magnitude as the HS is decreased (Figures 2.2- 2.4). These theoretical considerations suggest that the alternation is a natural consequence of the AV nodal functional properties.

2.4.2 Magnitude of the Alternation

Since the magnitude of the cycle length alternation was usually quite small, it is probably below the current resolution of most clinical studies. Nevertheless, the existence of a small magnitude cycle length alternation preceding the termination of the tachycardia may point to a general mechanism of reentry termination [7, 10, 11]. A recent theoretical study of reentry showed that an alternation of the action potential duration of a circulating reentrant pulse strongly reflects reentry instability [10]. For some model parameters, the cycle length alternation during this unstable reentry was shown to be very small. Therefore, the present study supports the hypothesis that even a very small cycle length alternation may be an important indicator of instability. Based on these considerations, we predict that cycle length alternation will often be observed prior to the termination of clinical tachycardias provided that the measurements are carried out with sufficient precision.

The magnitude of the alternation is not always small. The magnitude of NCT alternation is dramatically increased in response to pharmacologic or hypoxic increases of AV nodal refractoriness [2, 4, 6, 13]. Such conditions may be quite common in a clinical environment. Therefore, a relatively large magnitude alternation of cycle length might often be observed prior to the termination of tachycardia in such patients.

2.4.3 Implications

The alternation of the NCT in this study results from the rate- dependent nodal properties. Similar observations are expected for any tachycardia driving the AV node near its upper 1:1 conduction limit. We propose that similar mechanisms could produce cycle length alternation in a variety of reentrant arrhythmias. For example, Ortiz et. al. [23] found that a cycle length alternation preceded the termination of atrial flutter. They showed that the alternation was due to beat-to-beat changes of the conduction time through regions of the reentrant circuit where the conduction was slow. The tachycardia was terminated by a block occurring in the slow region. The final beat corresponded to the lower branch of the alternation. These observations are very similar to the events preceding the spontaneous termination of AV reentrant tachycardia in our experimental model.

Very small electrical alternans have also been associated with the development of ventricular arrhythmias [24]. This may be related to our observation that alternation often precedes conduction block in a slow region. For example, a region of depressed myocardium may result in conduction time alternation and the development of a local block, thereby initiating functional reentry and possibly fibrillation.

In conclusion, our results demonstrate that NCT and concomitant cycle length alternation can arise during orthodromic AV reentrant tachycardia when the retrograde delay is sufficiently short. This alternation has a gradual onset and increases in magnitude with the shortening of the retrograde delay. Further shortening eventually results in an AV nodal block which temporarily terminates the tachycardia. The last successful propagation through the AV node corresponds to the lower branch of the alternation. The reinitiation of the tachycardia is triggered by a spontaneous beat successfully propagated through the AV node. These characteristics of the alternation are predictable from the known functional properties of the AV node without postulating dual pathway physiology.

2.5 Appendix

The previous mathematical model of AV node conduction [12] was based on the rate-dependent functional properties of the AV node. In this model, it was assumed that the shape of the decreasing facilitation function, $NCT_{n+1} = f(NCT_n)$, was concave down. The proposed bifurcation mechanism was that the fatigue property generated a slow vertical shift of f, and since f was concave down, the vertical shift caused the slope at the drifting fixed point to decrease (Fig. 2.9A). A period-doubling bifurcation occurred when the slope became less than -1, thereby destabilizing the period-1 rhythm and generating an alternans rhythm. This bifurcation mechanism relies on two assumptions: i) fatigue causes a vertical shift of f, and ii) f is concave down.

The physiological mechanism for facilitation has been suggested to result from the properties of the action potentials of cells in the distal node. Here, we show that a simple model incorporating this physiological mechanism has implications for the shape of f as well as the proposed bifurcation mechanism.

Our simple model is a special case of a class of models proposed by Chialvo *et al.* [25] for the dynamics of propagation along Purkinje fibers. Figure 2.9B illustrates the variables in the model. Our basic assumption is that both the AV nodal conduction time (AH interval) and the action potential duration (APD) of the distal nodal cells (H cells) are functions of the time interval between the end of the H action potential and the next atrial activation called the diastolic interval (DI):

$$\begin{aligned} NCT_{n+1} &= P(DI_n), \\ APD_{n+1} &= Q(DI_n). \end{aligned} \tag{2.1}$$

The function P is called the recovery curve and Q is called the restitution curve.

Since our recordings were obtained using unipolar extracellular electrodes, the action potentials were not measured and the diastolic interval was not controlled. Rather, our fixed-delay stimulation protocol held the HA interval fixed at some interval λ. But since $DI_n = \lambda - Q(DI_{n-1})$ and $DI_{n-1} = P^{-1}(NCT_n)$, the diastolic

interval can be expressed in terms of λ:

$$DI_n = \lambda - Q\big(P^{-1}(NCT_n)\big), \tag{2.2}$$

and thus the nodal conduction time can be expressed as a function of the previous conduction time for fixed λ.

Given the following analytic forms for P and Q [26]:

$$\begin{aligned} P(DI_n) &= a + b\exp(-DI_n/\tau_{rec}), \\ Q(DI_n) &= c - d\exp(-DI_n/\tau_{res}), \end{aligned} \tag{2.3}$$

by substituting (2.3) and (2.2) into (2.1) the AV nodal conduction time is given by:

$$NCT_{n+1} = a + h(NCT_n)\exp(-\lambda/\tau_{rec}) \equiv f(NCT_n, \lambda), \tag{2.4}$$

where h is the following decreasing function:

$$h(NCT_n) = \kappa\exp\big(-\xi(NCT_n - a)^\gamma\big), \tag{2.5}$$

where $\kappa = b\exp(c/\tau_{rec})$ and $\xi = db^{-\gamma}/\tau_{rec}$ with $\gamma = \tau_{rec}/\tau_{res}$.

Equation 2.4 predicts that a decrease in the fixed-delay time λ causes f to become a steeper function. Therefore, the fixed point can become destabilized and alternans can be generated by decreasing λ just as we observed in the experiments (Fig. 2.2).

This simple model predicts the shape of f: if $\gamma \leq 1$ then f is concave up everywhere, whereas if $\gamma > 1$ then f is a bell-shaped function. Therefore, the assumption that f is strictly concave down is not supported by our simple model of facilitation. This means that the period-doubling mechanism suggested in the previous AV node model is not likely because a vertical shift of f due to fatigue will decrease, rather than increase, the magnitude of the slope at the fixed point. If our simple model is correct, then fatigue must be more than a simple vertical shift of f. Rather, fatigue probably shifts f up and to the right as depicted in Figure 2.7.

BIBLIOGRAPHY

[1] P. S. Barker, F. D. Johnston, and F. N. Wilson, Am. Heart J. **25**, 799-811 (1943).

[2] P. V. L. Curry and D. M. Krikler, (Abstract) Br. Heart J. **38**, 882 (1976).

[3] H. D. Friedberg and L. Schamroth, J. Electrocardiol. **6**, 159- 163 (1973).

[4] R. L. Rinkenberger, E. N. Prystowsky, J. J. Heger, et al., Circulation **62**, 996-1010 (1980).

[5] R. Spurrell, D. Krikler, and E. Sowton, Br. Heart J. **35**, 113- 121 (1973); R. J. Sung, and J. L. Styperek, Circulation **60**, 1464-1476 (1979).

[6] J. Vohra, D. Hunt, J. Stuckey, et al., Br. Heart J. **36**, 570-576 (1974); H. Wellens, S. L. Tan, F. Bar, et al., Br. Heart J. **39**, 1058-1066 (1977).

[7] L. H. Frame and M. B. Simpson, Circulation **78**, 1277-1287 (1988).

[8] D. L. Ross, W. Dassen, E. J. Vanagt, et al., Circulation **65**, 862-868 (1982).

[9] D. L. Ross, J. Farre, F. W. H. M. Bar, et al., Circulation **63**, 1129- 1139 (1981).

[10] Y. Rudy, J. Cardiovasc. Electrophysiol. **6**, 294-312 (1995).

[11] M. B. Simson, J. F. Spear, and E. N. Moore, Am. J. Physiol. **240**, H947-H953 (1981).

[12] J. Sun, F. Amellal, L. Glass, et al., J. Theor. Biol. **173**, 79-91 (1995).

[13] T. Lewis and G. C. Mathison, Heart **2**, 47-53 (1910).

[14] J. J. Gallagher, R. H. Svenson, W. C. Sealy, et al., Circulation **51**, 767-785 (1975); H. Wellens Br. Heart J. **37**, 231-241 (1975); H. Wellens and D. Durrer Circulation **52**, 58-72 (1975).

[15] J. Billette and R. Metayer, Circ. Res. **65**, 164-175 (1989); J. Billette, R. Metayer, and M. St-Vincent, Circ Res **62**, 790-799 (1988).

[16] F. Amellal and J. Billette, Circulation (in press).

[17] M. Tremblay and J. Billette, IEEE Transactions Biomed. Engin. **1**, 345-346 (1995).

[18] J. Billette Am. J. Physiol. **241**, H26-H33 (1981); J. Billette, J. P. Gossard, L. Lepanto, et al., Am. J. Physiol. **251**, H919-H925 (1986); J. Billette and S. Nattel, J. Cardiovasc. Electrophysiol. **5**, 90-102 (1994); J. Billette, F. Amellal, J. Zhao, et al., J. Cardiovasc. Electrophysiol. **5**, 63-75 (1994).

[19] P. Denes, D. Wu, R. C. Dhingra, et al., Circulation **48**, 549-555 (1973); W. Zeng, T. Mazgalev, A. A. Munk, et al., in *From Cell to Bedside: Cardiac Electrophysiolgy*, edited by D. Zipes and J. Jalife (W. B. Saunders, Philadelphia, 1995) p. 314.

[20] M. E. Josephson, *Clinical Cardiac Electrophysiology: Techniques and Interpretations* (Lea and Febiger, Philadelphia, 1993) p.181-274.

[21] D. Wu, P. Denes, R. C. Dhingra, et al., Circ. Res. **34**, 682 (1974); B. N. Goldreyer and A. N. Damato, Circulation **63**, 678 (1971); P. Brugada, E. J. Nanagt, and W. R. Dassen, Eur. Heart J. **1**, 399 (1980); R. G. Sheahan, G. J. Klein, R. Yee, et al., Circulation **93**, 969-972 (1996).

[22] M. A. McGuire and M. J. Janse, Curr. Opin. Cardiol. **10**, 3-8 (1995).

[23] J. Ortiz, M. Igarashi, X. Gonzalez, et al., Circulation **88**, 1866-1877 (1993).

[24] D. S. Rosenbaum, L. E. Jackson, J. M. Smith, et al., N. Engl. J. Med. **330**, 235-241 (1994); J. M. Smith, E. A. Clancy, C. R. Valeri, et al., Circulation **77**, 110-121 (1988); D. R. Adam, J. M. Smith, S. Akselrod, et al., J. Electrocardiol. **17**, 209-218 (1984).

[25] D. R. Chialvo, D. C. Michaels, and J. Jalife, Circ. Res. **66**, 525-545 (1990).

[26] M. R. Guevara, G. Ward, A. Shrier, L. Glass, in *Computers in Cardiology*, IEEE Comp. Soc. (1984) pp. 167-170.

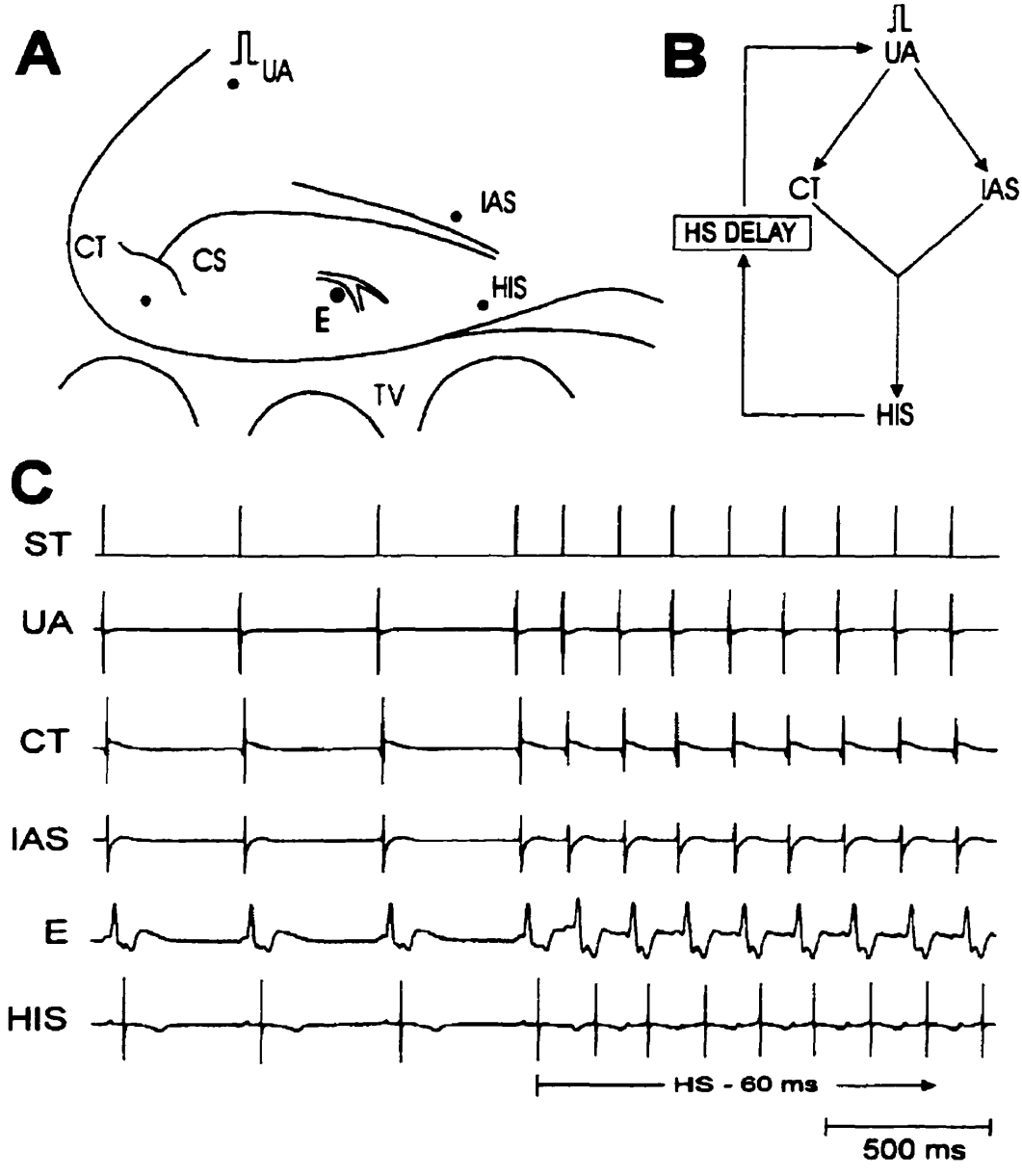

Figure 2.1: A, preparation with anatomic landmarks, pacing site (rectangular pulse) and recording sites (closed circles). B, schematic representation of our model of atrioventricular reentrant tachycardia with the two nodal inputs, the node itself and the retrograde return pathway to the atrium simulated by an electronic circuit. The His-stimulus (HS) interval controls the retrograde delay of the reentrant circuit. C, electrograms recorded during the initiation of the tachycardia with an HS of 60 ms. UA, upper atrium. CT, low crista terminalis. IAS, low interatrial septum. CS, coronary sinus. HIS, His-bundle. TV, tricuspid valve. E, nodal electrode.

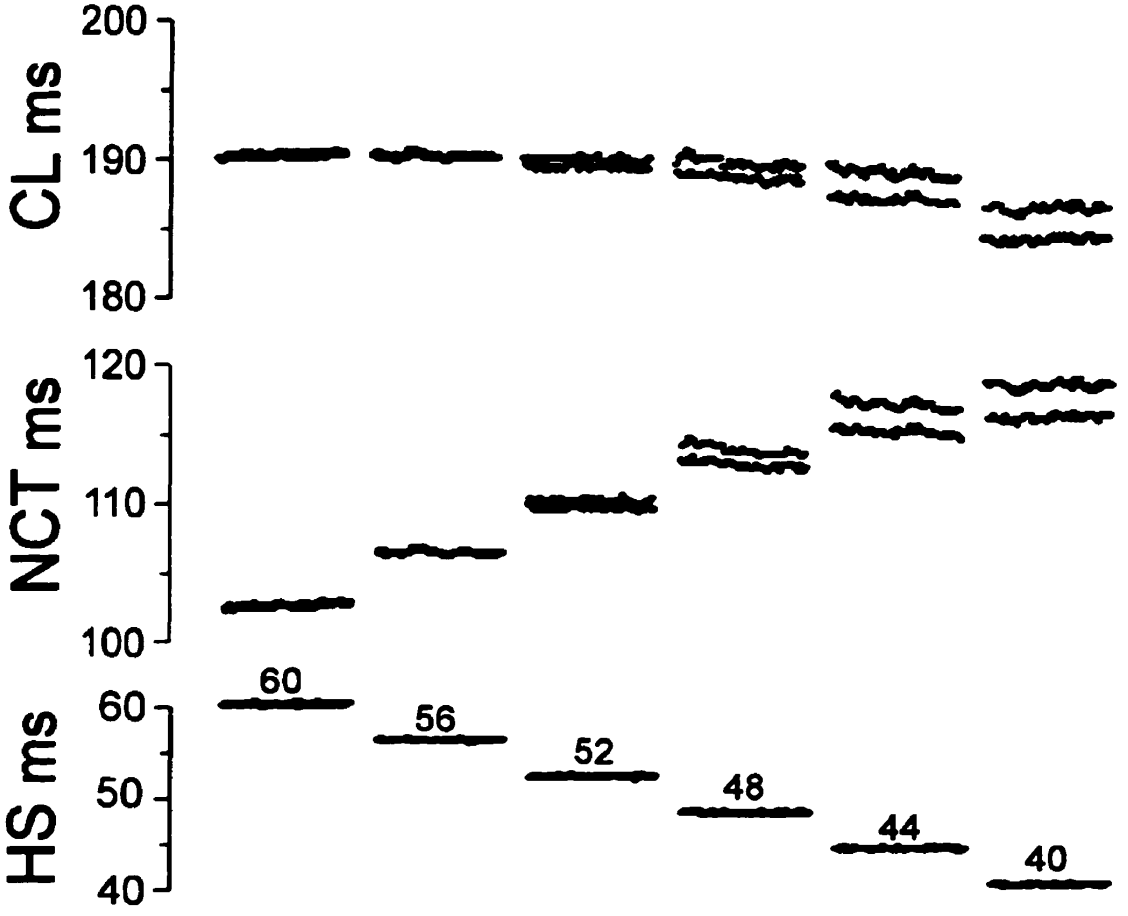

Figure 2.2: Progressive onset of cycle length (top) and NCT (middle) alternation obtained from one preparation in response to decreasing HS values (bottom). Each sequence countains 100 beats taken at steady state approximately 1-min after the HS shortening. All values are in ms.

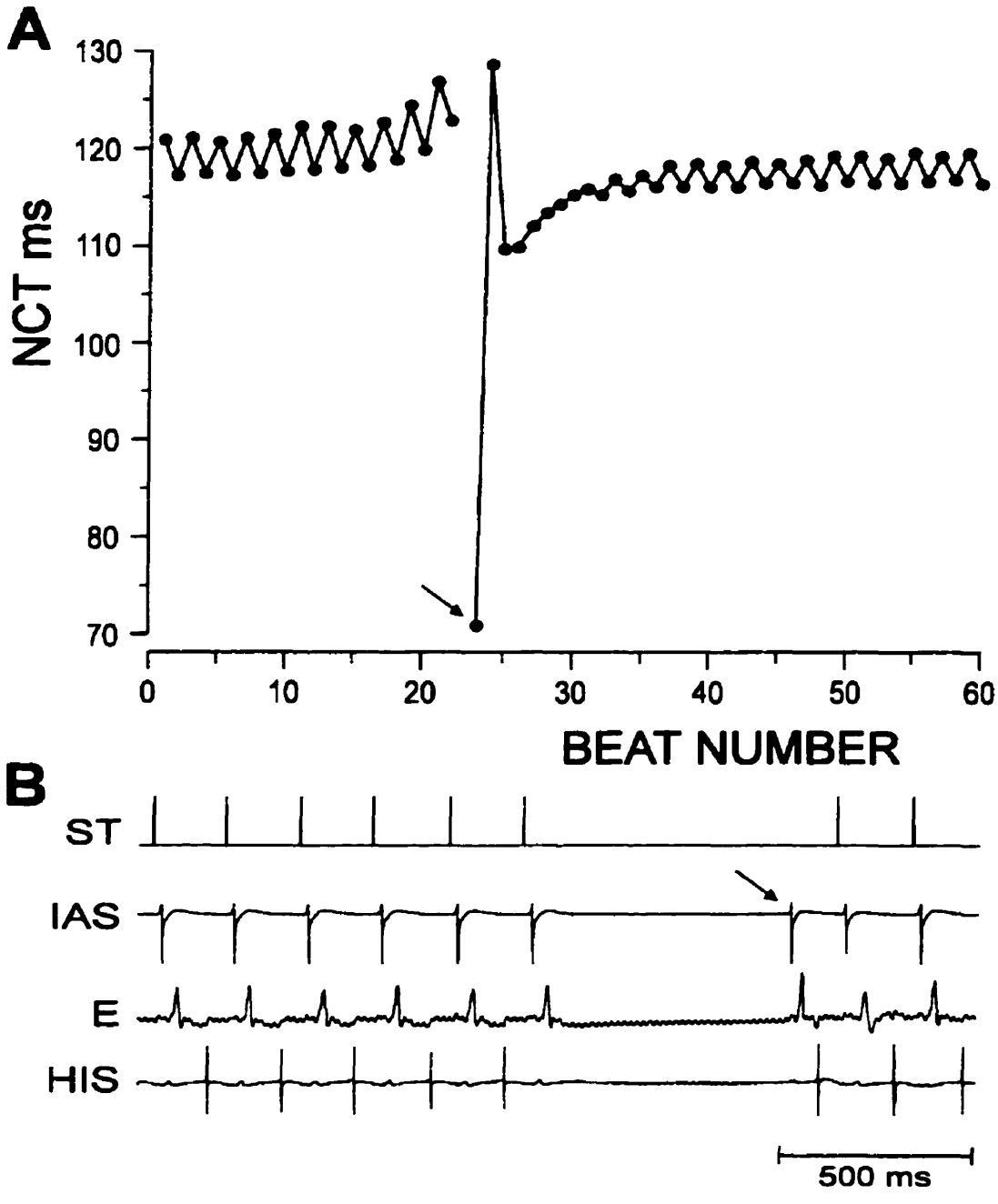

Figure 2.3: A, beat to beat changes of NCT observed during spontaneous termination and restarting of the tachycardia associated with a constant HS of 40 ms. The last conducted beat corresponds to the lower branch of NCT alternation. A spontaneous atrial beat (arrow) reinitiates the tachycardia. Corresponding electrograms are depicted in B.

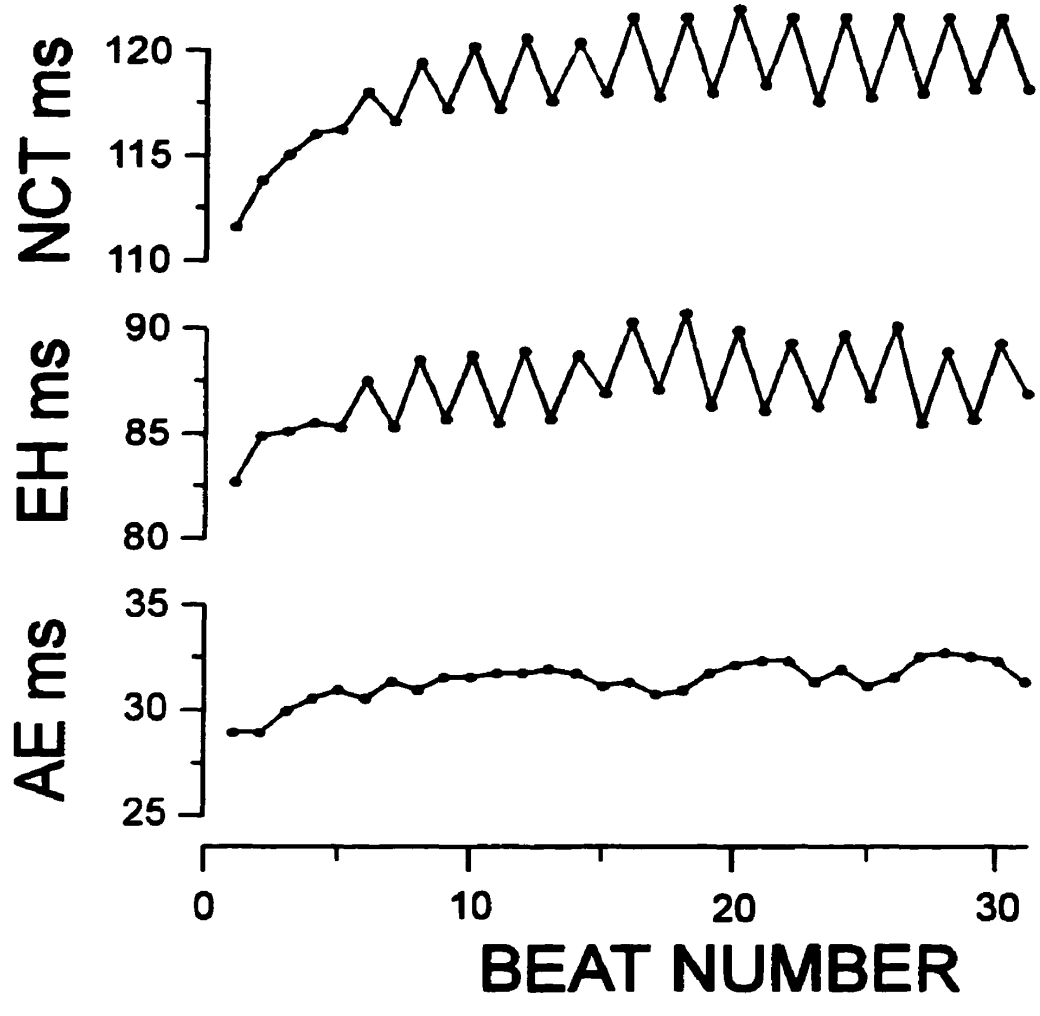

Figure 2.4: Origin of NCT alternation during restarting tachycardia initiated with a 40 ms HS. While both NCT and distal conduction time (EH) similarly alternate, the proximal conduction time (AE) does not.

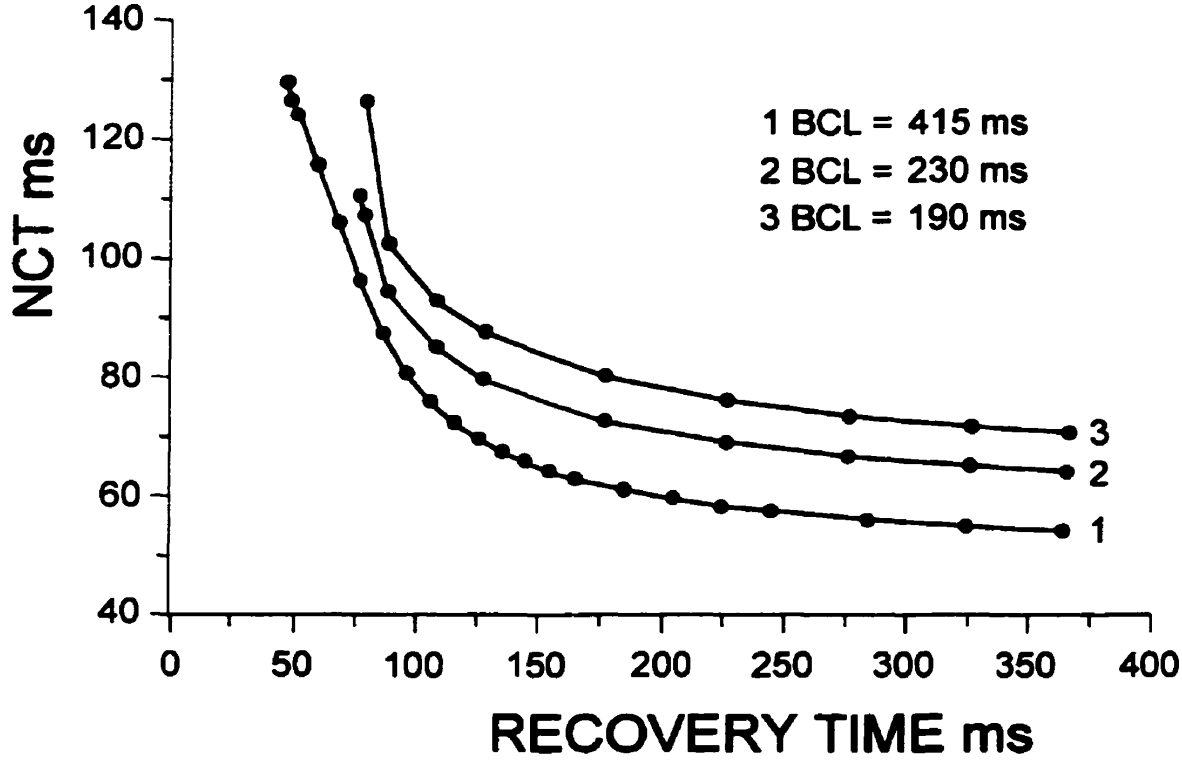

Figure 2.5: Recovery curves (NCT plotted as a function of HA) obtained at the 3 listed basic cycle lengths (BCL) in a typical preparation. The 3 curves were obtained at steady state basic NCT. Note the continuous nature of the curves at all 3 basic rates.

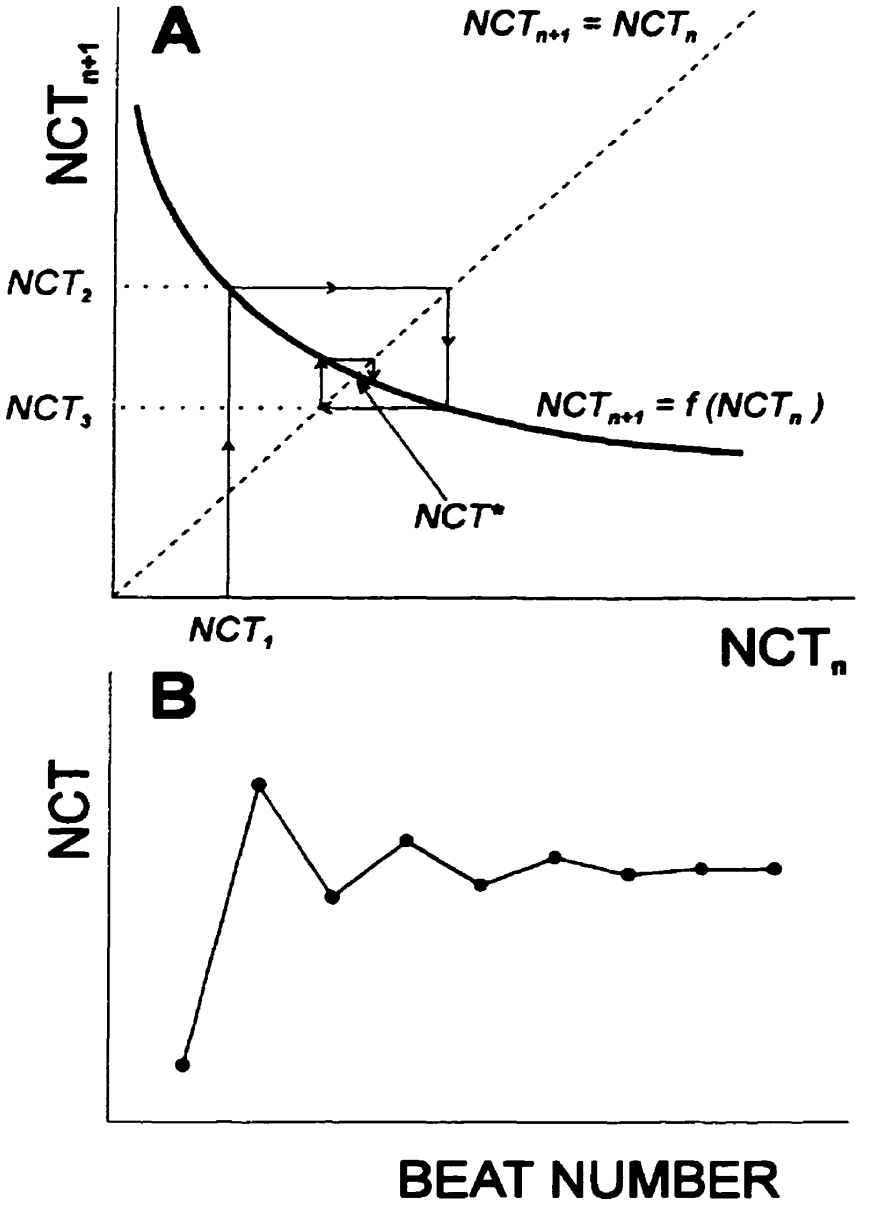

Figure 2.6: A, schematic representation of a function, f, relating successive NCT for a fixed HS. Given some initial NCT value, NCT_1, we can iterate this function to determine the sequence of NCT depicted in B. In this case, the NCT relaxes to a steady state value, NCT^*, called the fixed point.

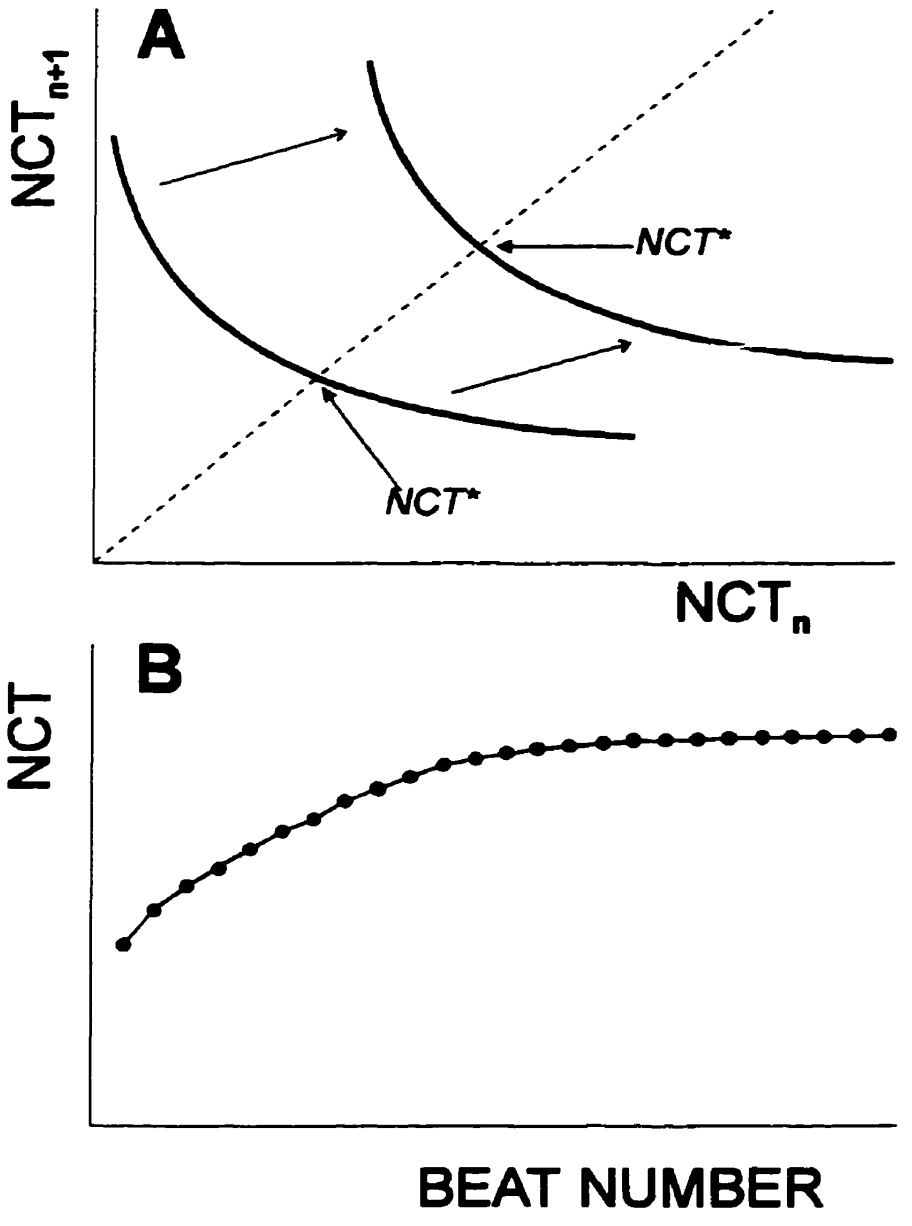

Figure 2.7: Simulation of the effects of AV nodal fatigue. A, as fatigue increases, the function f is slowly shifted up and right. The fixed point, NCT^*, slowly increases and gives the NCT sequence shown in B. Notice that the slope of the function at the fixed point is becoming more negative with increasing fatigue.

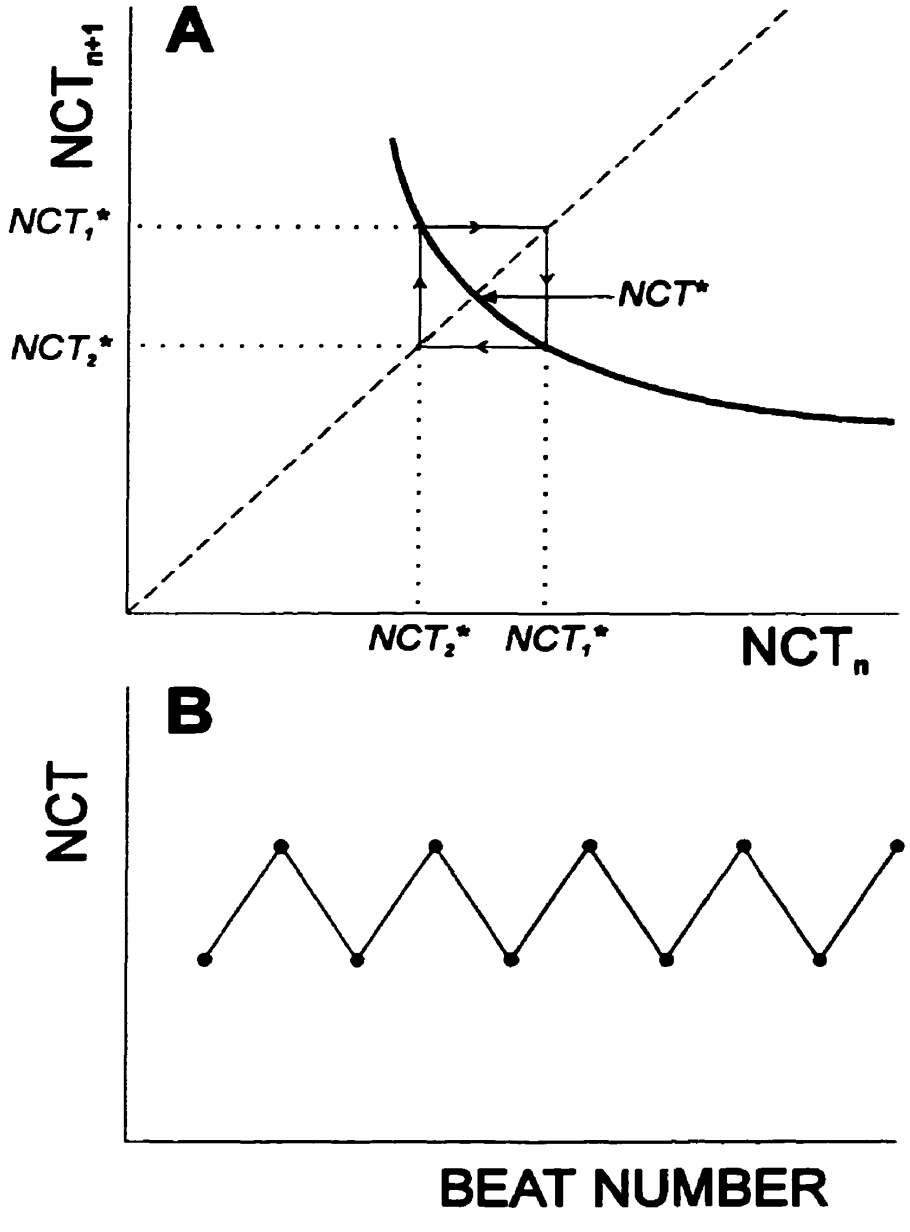

Figure 2.8: A, NCT alternation occurring when the slope of the function, f, at the fixed point, NCT^*, becomes less than -1. The graph predicts that the magnitude of the alternation, $\Delta NCT = NCT_1 - NCT_2$ will gradually increase as the slope becomes steeper. B, typical sequence of resulting NCT alternation.

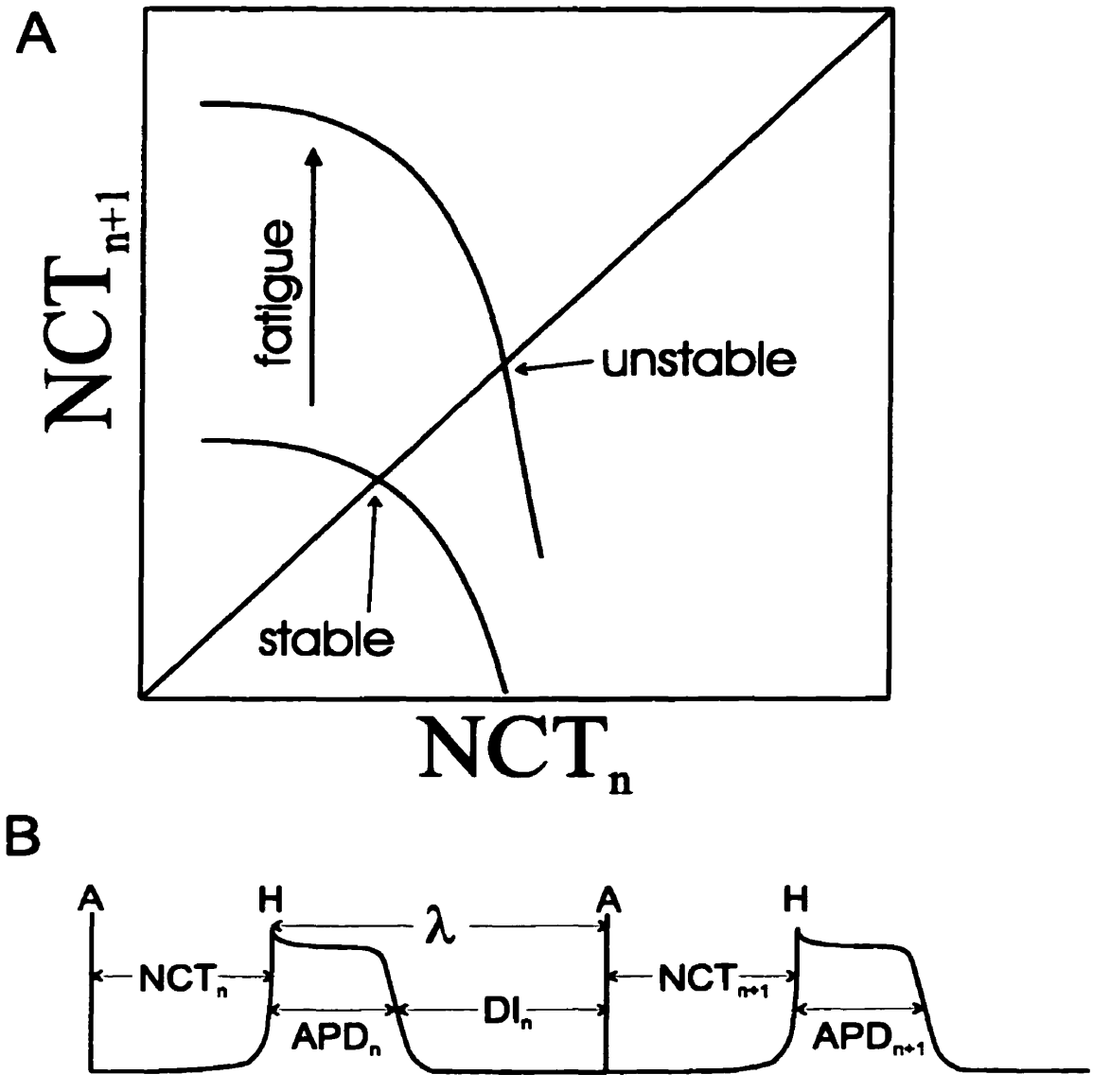

Figure 2.9: A) Bifurcation mechanism proposed by Sun *et al.*. B) Definition of variables in a simple model of facilitation.

CHAPTER 3
DYNAMIC CONTROL OF CARDIAC ALTERNANS

3.1 Foreward

Control techniques from the field of nonlinear dynamics [1] have been used to control both chaotic [2] and nonchaotic [3] dynamical systems. Since these control methods do not require knowledge of the system's governing equations, they are particularly applicable in biology where detailed mathematical models are usually unavailable. Control of biological dynamics is important for medical science since abnormal physiological rhythms can be life-threatening [4]. Attempts have already been made to control both experimental [5] and model [6, 7] biological systems. However, none of these studies used control algorithms which adapted to evolving system parameters. Since physiological environments typically drift over time, practical biological control schemes must adapt to these changes. Here, we utilize an algorithm which controls an evolving cardiac arrhythmia called an alternans rhythm in the rabbit heart.

3.2 Cardiac Alternans Rhythms

Cardiac alternans rhythms are characterized by an alternation of the timing or morphology of the heart's electrical activity from one beat to the next. While the clinical importance of cardiac alternans has only recently been recognized [8], their discovery dates back to the earliest recordings of cardiac electrical signals [9]. We generated cardiac alternans by electrically stimulating a piece of dissected rabbit heart[1]. Each stimulus delivered to the upper atrium caused a wave of electrical activity to propagate through the atrium, the atrioventricular node and out the His bundle (Fig. 3.1A). We measured the electrical activity near an atrial input of the AV node and at the His bundle output (Fig. 3.1B). X, was the time for the impulse to pass through the

[1]The experimental methods used in this study are identical to those described in the previous chapter with the exception that the alternans magnitude was increased by either inducing transient hypoxia (n=2), or using a combination of hypoxia and the calcium channel blocker verapamil (30 ng/mℓ) (n=3). These maneuvers decreased the electrical excitability of the preparation and mimicked the situation where large amplitude AV nodal alternans have been observed clinically [8].

AV node. The output impulse was re-injected into the atrium after a time delay λ. When λ was made sufficiently small, the conduction time through the AV node began to alternate [10] (Fig. 3.1B).

3.3 AV Node Dynamics

The dynamics of AV nodal conduction can be characterized by a one-dimensional map

$$X_{n+1} = f(X_n, \lambda), \tag{3.1}$$

where X_n is the AV nodal conduction time following the nth atrial stimulus, λ is the time delay from His bundle activation to the next atrial stimulus, and f is a nonlinear, decreasing function of both arguments which relates the successive conduction times [10]. The map is represented as a graph in Fig. 3.2A. This map determines the sequence of AV nodal conduction times, X_1, X_2, X_3,..., X_n given some initial conduction time, X_0, for fixed λ. The intersection of the curve with the line of identity ($X_{n+1} = X_n$) defines the period-1 fixed point $X^* = f(X^*, \lambda)$. If $\left|\frac{\partial f}{\partial X}\right| < 1$ at X^*, then X^* is stable and the sequence of conduction times will converge to X^* (Fig. 3.2A). If $\frac{\partial f}{\partial X}$ at X^* becomes less than -1, then X^* loses stability and a period-2 cycle gains stability. In our preparation, this period-doubling bifurcation causes the alternans rhythm [10]. For example, Fig. 3.2B shows a sequence of conduction times diverging from the fixed point (dashed arrows) and the development of alternans (solid arrows) for one of our preparations. Slow nonstationary effects are associated with gradual deformations of f over several iterations, which can both shift X^* and change the slope of f at X^*.

3.4 Alternans Control Algorithm

Since alternans arise when a fixed point loses stability in the manner described above, the unstable fixed point must lie between the alternating X's. Control of alternans can be achieved by directing the system towards the unstable fixed point by varying λ for

certain beats[2]. This procedure is schematically depicted in Fig. 3.2C. By shortening λ by an appropriate amount $\delta\lambda_n$ after a large X_n, the map f shifts to the dashed curve. The subsequent X_{n+1} is thereby directed closer to the unstable fixed point X^* as shown by the dashed arrow.

The simplest way to choose the magnitude of $\delta\lambda_n$ is to make it proportional to the distance between the system's present state point, X_n, and the unstable fixed point. Therefore, the stimulus delay time for beat $n+1$ was shortened by an amount $\delta\lambda_n$, where

$$\delta\lambda_n = \alpha(X_n - \widehat{X}^*).$$

The proportionality constant α established the sensitivity of the control algorithm. $\widehat{X}^*$ was the current estimate of X^* approximated as the midpoint of the alternating X's

$$\widehat{X}^* = \frac{1}{2}(X_n + X_{n-1}).$$

This fixed point estimate was recomputed after each beat allowing us to adaptively locate the real fixed point. It is not necessary to know the analytic form of f to apply this algorithm.

3.5 Results

We used this control method to suppress alternans rhythms in 5 rabbit heart preparations. The left panels of Fig. 3.3 show the sequence of AV nodal conduction times X_n before, during, and after the control period along with the corresponding values for λ_n in 3 different preparations. The right panels are points of f obtained during the transient periods at the onset (+) and following the termination (•) of the control. Fig. 3.3A shows control of nonstationary alternans which have an increasing magnitude and a slow average drift of the AV nodal conduction time. Because the unstable fixed point was adaptively located, its evolution was tracked. The right panel shows the shift of f over the course of the control. Fig. 3.3B shows that when control was

[2]Our control algorithm is a modified version of the one used in reference [7]. Our modifications ensured that the algorithm changed the stability, but not the location, of the uncontrolled system's unstable period-1 fixed point.

initiated near the onset of alternans, relatively small perturbations (less than 2 ms) were required to suppress its development. In this case, the unstable fixed point did not evolve appreciably over the course of the control.

The control technique requires that we choose an appropriate proportionality constant α. In our experiments, α was chosen by trial and error. If α was too small the alternans magnitude was reduced, but not eliminated. For example, the preparation depicted in Fig. 3.3C shows that the first control attempt, with $\alpha_1 = 3.3$, was not sufficient to eliminate the alternans. The next attempt, with $\alpha_2 = 5.0$, was successful. These observations led us to examine the stability conditions of the controlled system.

3.6 Stability of the Controlled Fixed Point

Turning on the control algorithm had the effect of transforming the one-dimensional map 3.1 into the following two-dimensional system:

$$\begin{aligned} X_{n+1} &= f\left(X_n, \lambda - \frac{\alpha}{2}(X_n - Y_n)\right) \\ Y_{n+1} &= X_n \end{aligned} \tag{3.2}$$

The period-1 fixed point of this system (X^*, Y^*) has the property: $X^* = Y^*$, which is also the value of the uncontrolled system's fixed point. The Jacobian of this system is

$$\begin{bmatrix} A - \frac{\alpha}{2}B & \frac{\alpha}{2}B \\ 1 & 0 \end{bmatrix} \tag{3.3}$$

where $A = \frac{\partial f}{\partial X}$ and $B = \frac{\partial f}{\partial \lambda}$. In our case, both A and B are negative at the fixed point.

The fixed point is stable provided that the Jacobian has eigenvalues which fall

within the unit circle. This condition is met for α in the following range:

$$\frac{(|A|-1)}{|B|} < \alpha < \frac{2}{|B|}, \tag{3.4}$$

where all terms are evaluated at the fixed point. Although it is not necessary to know the analytic form of f to apply the control algorithm, the properties of the map determine the range of α which gives effective control.

Because many beats had conduction times which were less than $\widehat{X}^*$, $\delta\lambda_n$ was often negative, implying that the stimulus should have been delayed for those beats. However, in clinical situations where alternans occur naturally, beats induced via electrical stimulation can only shorten λ. Therefore, premature stimuli were delivered only after beats with conduction times larger than $\widehat{X}^*$. Otherwise, $\delta\lambda_n$ was set to zero and the stimulus was delivered at the unperturbed delay, λ. This modification doubles the lower limit of effective α and the upper limit increases as described in Chapter 4.

To estimate the lower limits of effective α in our experiments, we assumed that f had the following form: $f(X_n, \lambda) = a + \exp(-\lambda/\tau)h(X_n)$, where a and τ are parameters which can be determined experimentally, and h is an unknown decreasing function [10]. Therefore, at the fixed point $B = -\frac{1}{\tau}(X^* - a)$. Previous studies have shown that typical values for a and τ are 80 ms and 70 ms respectively. [10]. Using these parameters, and X^* and A determined from the maps in Fig. 3.3, we estimated that the lower limits of effective α are 2, 0.7, and 5 for the preparations shown in Figures 3.3A, B, and C respectively. These limits agree with our observations.

3.7 Complex Alternans

In some preparations the alternans rhythm was more complex. For example, Fig. 3.4A shows irregular oscillations superimposed over each alternans branch. This kind of behavior is seen when the curve f shifts back and forth with a period of about 20 beats (not shown). The physiological mechanism of such a nonstationarity is unknown. Nevertheless, the control algorithm successfully eliminated these irregular alternans

(Fig. 3.4B, C), thus showing that the technique is robust to complex rhythms.

3.8 Discussion

Previous biological control experiments implemented a pre-control learning phase to estimate X^* which was held constant over the course of the control [5]. Any error in the fixed point estimate leads to a controlled fixed point which differs from that of the uncontrolled system. Furthermore, an evolving fixed point of the original system can not be tracked using such a scheme.

Since we recomputed our fixed point estimate $\widehat{X}^*$ after each beat, our control algorithm accurately targeted the original system's unstable period-1 fixed point. Slow evolution of the fixed point was tracked. However, since f slowly evolves, the limits on the range of effective α correspondingly change. Therefore, while α may initially be in the effective range, the system's evolution may lead to destabilization. In most cases, the range of effective α was sufficiently large so that the gradual evolution of the system did not destabilize the fixed point.

Suppression of cardiac alternans has important clinical implications given that alternans in the ECG morphology often precedes life-threatening arrhythmias and is a risk factor for sudden death [8]. If a control algorithm similar to the one used in the present study was incorporated in a prosthetic cardiac pacemaker, such alternans rhythms might be suppressed and a route to a fatal arrhythmia curtailed.

BIBLIOGRAPHY

[1] E. Ott, C. Grebogi, and J. A. Yorke. Phys. Rev. Lett. **64,** 1196-1199 (1990).

[2] W. L. Ditto, S. N. Rauseo, and M. L. Spano. Phys. Rev. Lett. **64,** 3211 (1990); E. R. Hunt. Phys. Rev. Lett. **67,** 53 (1991); B. Peng, V. Petrov, and K. Showalter. J. Phys. Chem. **95,** 4957 (1991).;V. Petrov, B. Peng, and K. Showalter. J. Chem. Phys. **96,** 7505-7513 (1992); R. Roy, T. W. Murphy, T. D. Maier, Z. Gills, and E. R. Hunt. Phys. Rev. Lett. **68,** 1259 (1992).

[3] T. L. Carroll, I. Triandaf, I. B. Schwartz, and L. Pecora. Phys. Rev. A **46,** 6189 (1992); Z. Gills, C. Iwata, R. Roy, I. B. Schwartz, and I. Triandaf. Phys. Rev. Lett. **69,** 3169 (1992); I. B. Schwartz, and I. Triandaf. Phys. Rev. A **48,** 718 (1993); V. Petrov, M. J. Crowley, and K. Showalter. Phys. Rev. Lett. **72,** 2955 (1994); N. F. Rulkov, L. S. Tsimring, and H. D. I. Abarbanel. Phys. Rev. E **50,** 314 (1994).

[4] M. E. Josephson, *Clinical Cardiac Electrophysiology:Techniques and Interpretation* (Lea Febiger, Philadelphia, 1993), 2nd ed.; D. Zipes, J. Jalife (eds), *From Cell to Bedside: Cardiac Electrophysiolgy* (WB Saunders, Philadelphia, 1995).

[5] A. Garfinkel, M. L. Spano, W. L. Ditto, and J. N. Weiss. Science **257,** 1230-1235 (1992); S. J. Schiff, K. Jerger, D. H. Duong, T. Chang, M. L. Spano, and W. L. Ditto. Nature **370,** 615-620 (1994).

[6] L. Glass and W. Zeng. Int. J. Bifurcation and Chaos **4,** 1061-1067 (1994); D. J. Christini and J. J. Collins. Phys. Rev. Lett. **75,** 2782-2785 (1995); T. L. Carroll Phys. Rev. E **52,** 5817 (1995); M. E. Brandt and G. Chen. Biol. Cybern. **74,** 1-8 (1996); M. E. Brandt and G. Chen. Int. J. Bifurcation and Chaos **6,** 715-723 (1996).

[7] D. J. Christini and J. J. Collins. Phys. Rev. E **53,** R49-R52 (1996).

[8] J. M. Smith, E. A. Clancy, C. R. Valeri, J. N. Ruskin, and R. J. Cohen. Circulation **77,** 110-121 (1988); D. S. Rosenbaum, L. E. Jackson, J. M. Smith, H. Garan, J. N. Ruskin, and R. J. Cohen. N. Eng. J. Med. **330,** 235-241 (1994).

[9] T. Lewis. Q. J. Med. **4**, 141 (1910-11); T. Lewis, G. C. Mathison. Heart **2**, 47-53 (1910).

[10] J. Sun, F. Amellal, L. Glass, and J. Billette. J. Theor. Biol. **173,** 79 (1995); F. Amellal, K. Hall, L. Glass, and J. Billette. J. Cardiovasc. Electrophysiol. **7(10),** 943-951 (1996).

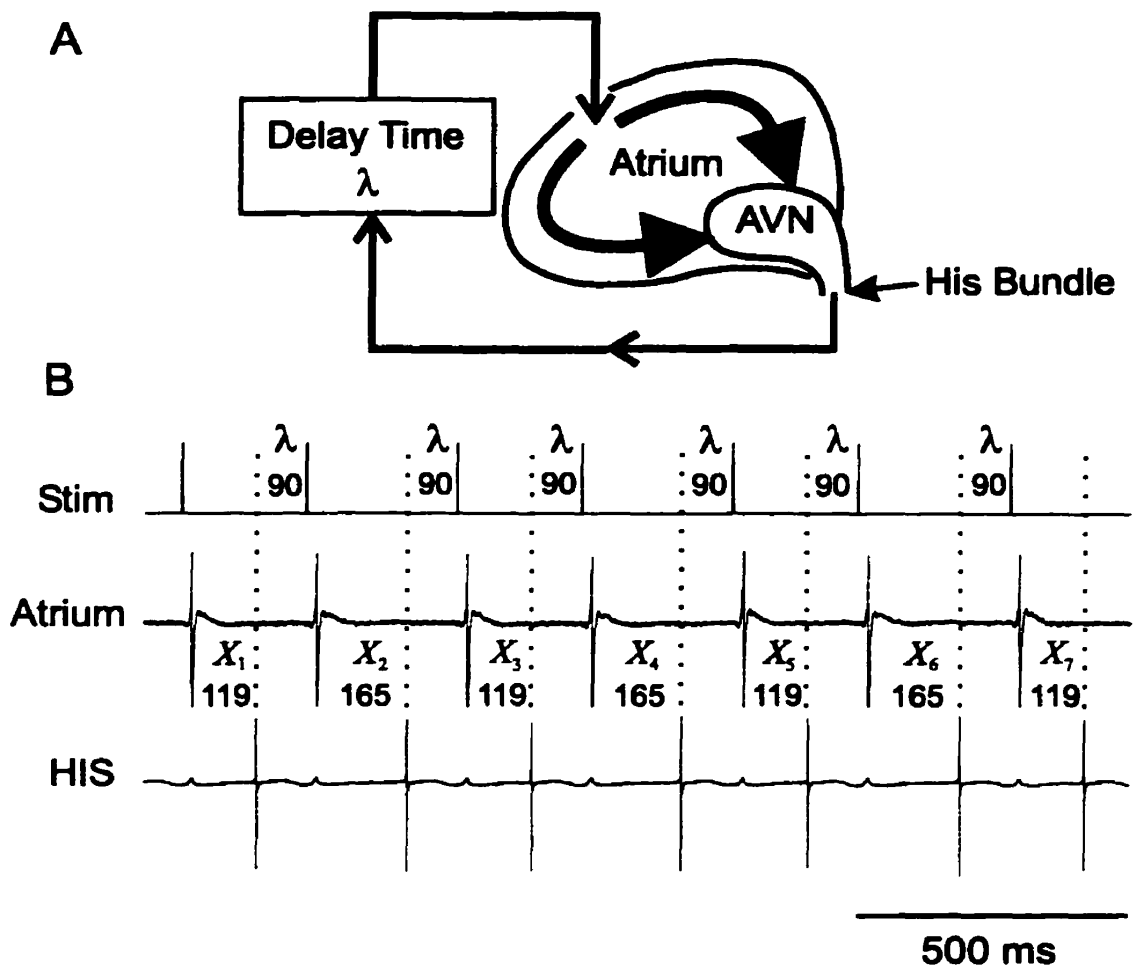

Figure 3.1: A) Schematic diagram of the rabbit heart preparation and pacing strategy. Following detection of His bundle (HIS) activation, we applied the next atrial stimulus after a time delay, λ, which was our control parameter. B) Stimulation pulses and electrograms recorded from the atrium and His bundle during alternans. The conduction time, X, through the atrioventricular node (AVN) was defined as the time interval between atrial and His bundle deflections. Here we show an alternation of X between 119 ms and 165 ms for $\lambda = 90$ ms.

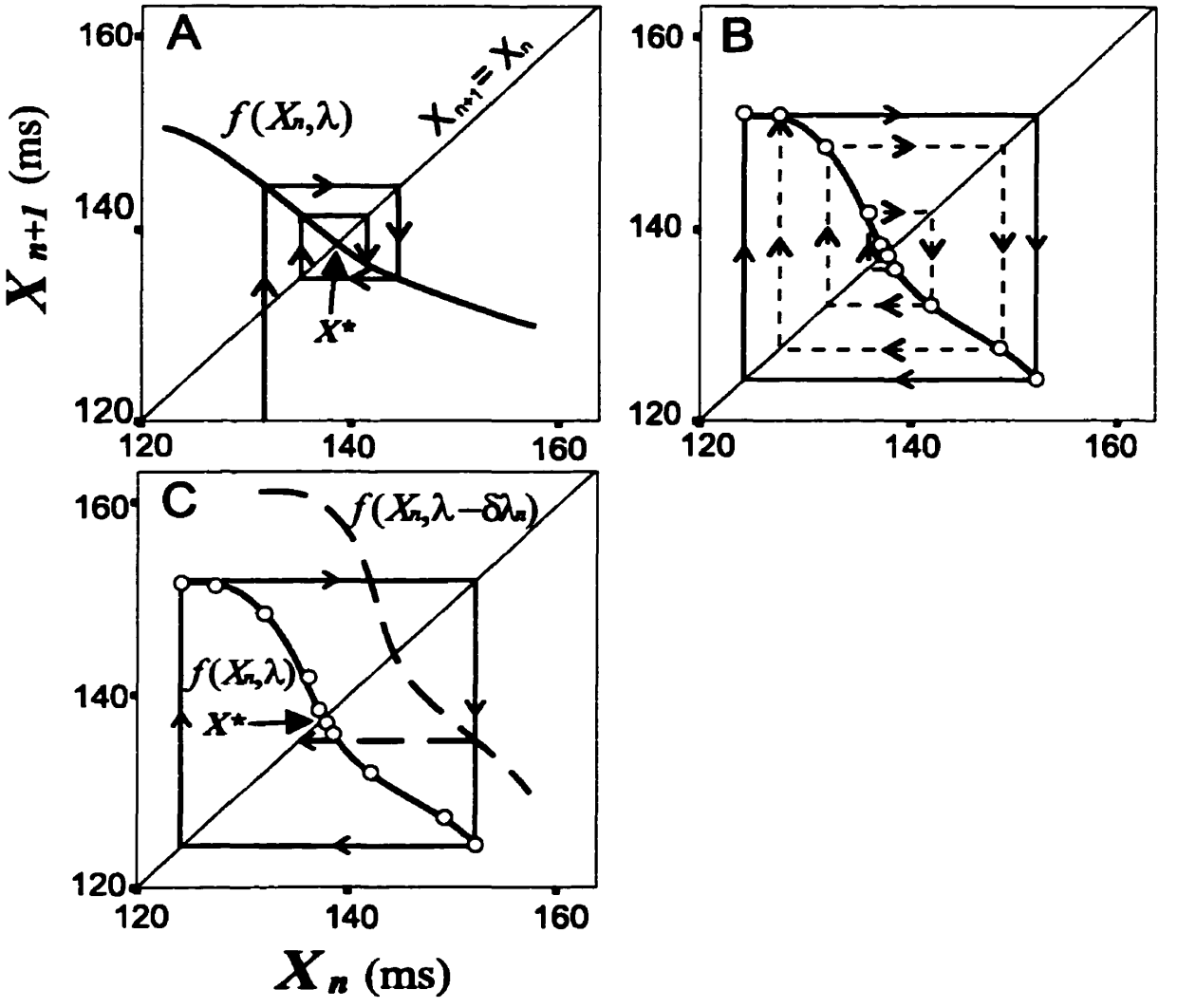

Figure 3.2: The difference equation, $X_{n+1} = f(X_n, \lambda)$, relating successive AV nodal conduction times and a schematic of the control mechanism. A) Convergence of successive conduction times to a stable fixed point, X^*, when the slope of $f(X_n, \lambda)$ at X^* is greater than -1. B) Development of alternans in one of our preparations when the slope of $f(X_n, \lambda)$ at X^* was less than -1. C) Effect of a premature stimulation, $\lambda - \delta\lambda_n$, on f. A premature stimulation applied after a beat with a long AV nodal conduction time directs the subsequent conduction time closer to X^* (dashed arrow).

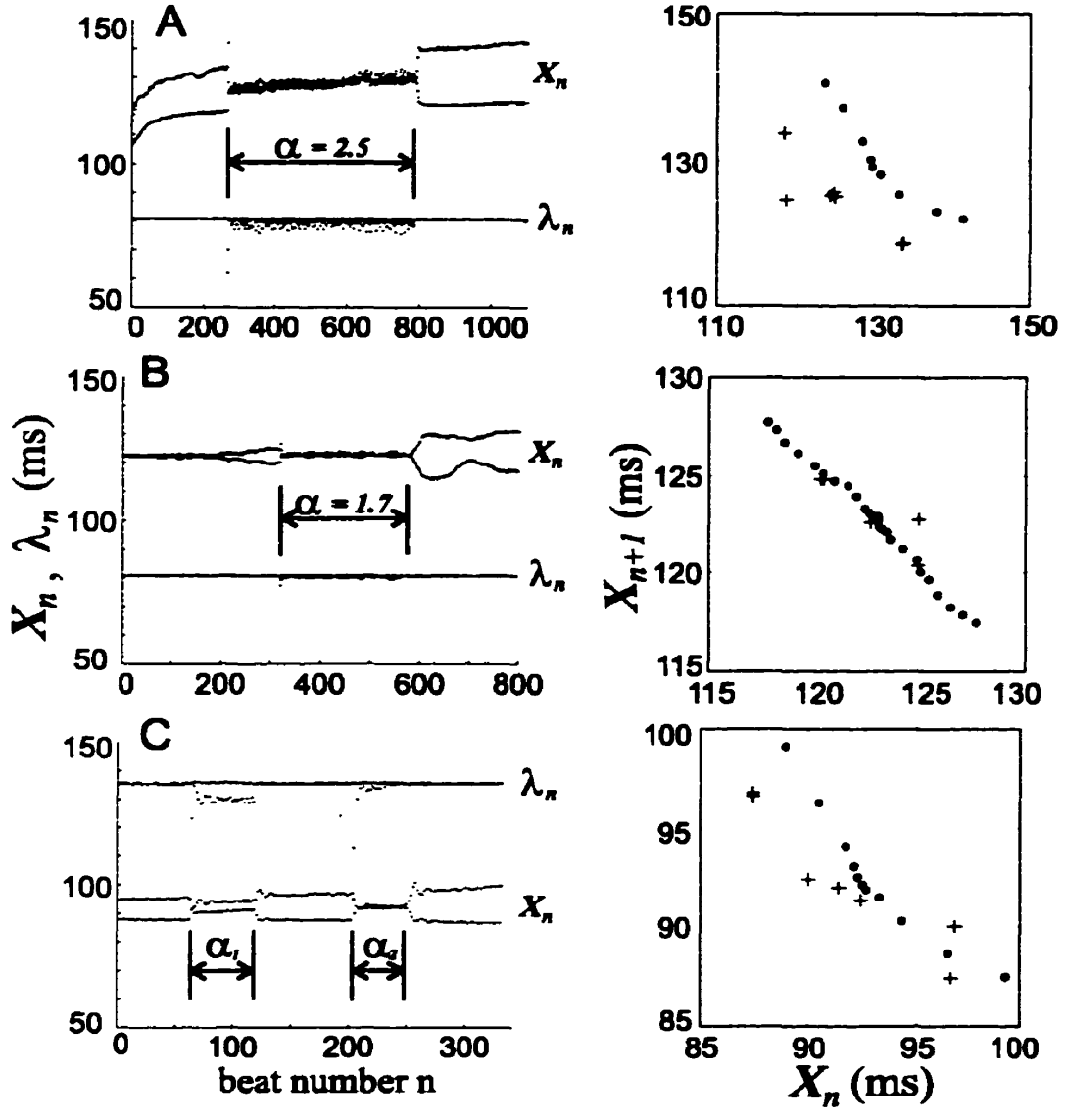

Figure 3.3: Control of alternans in three preparations. A) AV nodal conduction times X_n and delay times λ_n in the first preparation. Control was implemented from beat 266 to 787 (2 minutes) with $\alpha = 2.5$. The right panel plots X_{n+1} versus X_n at the onset (+) and following the termination (•) of the control sequence. The fixed point X^* after the control was 130 ms and the slope of the map at this point was -1.7. B) X_n and λ_n in the second preparation. Control was implemented from beat 319 to 550 for $\alpha = 1.7$. X^* after the control was 123 ms and the slope at the fixed point was -1.2. C) X_n and λ_n in the third preparation. The first control attempt was implemented from beat 79 to 134 with $\alpha_1 = 3.3$. The second control attempt was implemented from beat 219 to 255 with $\alpha_2 = 5.0$. After the second control, X^* was 92 ms and the slope at the fixed point was -1.5.

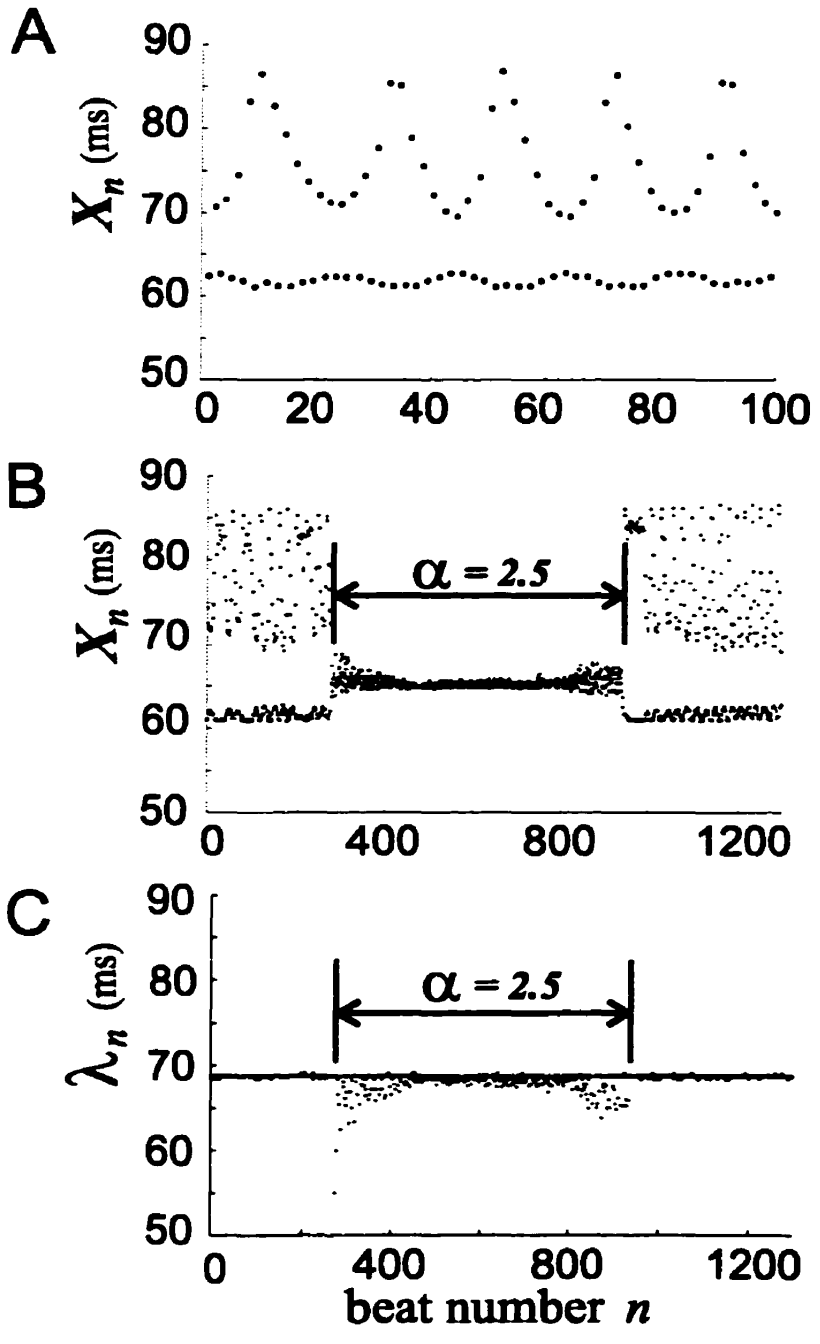

Figure 3.4: Control of complex alternans. A) 100 beats of X_n showing an irregular oscillation superimposed over each alternans branch. B) X_n with control implemented from beat 277 to beat 936 with $\alpha = 2.5$. C) Corresponding λ_n.

CHAPTER 4
RESTRICTED CONTROL OF ONE-DIMENSIONAL MAPS

4.1 Foreward

Recent success controlling complex dynamics of nonlinear physical and chemical systems [1] has opened the door for the control of biological rhythms. Some researchers have speculated about the medical implications of controlling heartbeat dynamics or brain rhythms [2, 3], but biological systems typically have characteristics that require special consideration. For example, all biological control studies to date [2, 3] have required that the control interventions be unidirectional - only allowing shortening of a parameter. This restriction can have detrimental effects on the ability to control these systems [4]. To extend the analogy of dynamic control being like balancing a meter stick on one's palm [5], restricted control is like trying to balance the meter stick by only allowing hand movements in one direction.

Surprisingly, the unidirectional restriction can improve the controllability of some systems. Here, we will describe how restricted control can introduce new stability zones, and we show that some of these zones were observed in our recent cardiac control experiments [3]. Furthermore, the structure of the stability zones suggests a way to modify the original control algorithm to automatically adapt the feedback gain parameter.

4.2 Delayed Feedback Control of Systems Described by One-Dimensional Maps

The cardiac dynamics in our experiments were described by a one- dimensional map:

$$X_{n+1} = f(X_n, \lambda), \tag{4.1}$$

where X_n is the variable under control and λ is the control parameter. The goal is to stabilize an unstable period-1 fixed point $X^* = f(X^*, \lambda)$ by perturbing λ by an amount:

$$\delta\lambda_n = \frac{\alpha}{2}(X_{n-1} - X_n), \tag{4.2}$$

where α is a feedback gain parameter. This is an example of delayed feedback control originally proposed by Pyragas [6]. The controlled system's fixed point is identical to the uncontrolled system. Thus, if the fixed point drifts over the course of the control (as is typical for biological systems) the controlled system will track the fixed point provided that the system stays in the stable range of the feedback gain α.

4.3 Linear Stability Analysis of Unrestricted Delayed Feedback Control

Linearizing about a fixed point at the origin gives:

$$\begin{aligned} X_{n+1} &= AX_n + \beta(Y_n - X_n), \\ Y_{n+1} &= X_n, \end{aligned} \tag{4.3}$$

where $A \equiv \frac{\partial f}{\partial X}$, and $\beta \equiv \frac{\alpha}{2}\left(\frac{\partial f}{\partial \lambda}\right)$ where both derivatives are evaluated at the fixed point. In the case of our cardiac experiments, $A < -1$ and $\beta < 0$.

The eigenvalues of (4.3) are $\left(A - \beta \pm \sqrt{(A-\beta)^2 + 4\beta}\right)/2$. The fixed point is stable provided that both eigenvalues fall inside the unit circle. This condition is met when:

$$-1 < \beta < \frac{1}{2}(A+1), \tag{4.4}$$

provided that $A < 1$ [3]. Note that the stability zone shrinks to zero for $A \leq -3$ [7] thereby limiting the applicability of the unrestricted control algorithm to maps with a sufficiently shallow slope at X^*.

4.4 Restricted Control

Restricting the above control algorithm by only allowing shortening of λ gives the following linearized system:

$$\begin{aligned} X_{n+1} &= AX_n + \Theta_n\beta(Y_n - X_n), \\ Y_{n+1} &= X_n, \end{aligned} \tag{4.5}$$

where

$$\Theta_n = \begin{cases} 1 & \text{if } (X_n - Y_n) > 0, \\ 0 & \text{otherwise.} \end{cases} \tag{4.6}$$

Thus, when $\Theta_n = 1$ the control is turned on, and when $\Theta_n = 0$ the control is turned off.

4.4.1 Geometric Interpretation of Restricted Control

Geometrically, the restriction 4.6 means that perturbations will only be applied if points on the return map lie above the line of identity $X_{n+1} = X_n$ (the dotted diagonal line in Figure 4.1). For example, Figure 4.1A shows how the restricted control algorithm stabilizes the unstable fixed point X^* in a linear system with $A = -4$ and $\beta = -3.1$. The solid line corresponds to the uncontrolled system and the dashed lines correspond to the perturbed system. X^* is at the intersection of the solid and dotted lines. In this case, the first control intervention causes the next iterate to fall below the line of identity implying that the next iterate will be uncontrolled. Furthermore, since the first controlled iterate was less than the fixed point, the next iterate will be above the identity line. Thus, control is applied every other iterate so that the sequence of Θ_n is 0101.... In this case, the fixed point is stabilized because control directs the system closer to the fixed point. For larger values of β the fixed point is not stabilized, but the oscillatory growth of X_n is slowed (not shown).

In our cardiac experiments, if the gain parameter α is increased, then β becomes

more negative. Figure 4.1B shows the situation when β is decreased to -3.23. As in the previous example, the first controlled iterate is below the line of identity (implying that the next iterate is uncontrolled). However, in this case the perturbation is bigger and the controlled iterate is slightly larger than the fixed point. This means that the next iterate is also below the line of identity and the control is applied in a 001001... sequence. This sequence is stable for $\beta = -3.23$ because the first controlled iterate directed the system closer to the fixed point. But if β is decreased to -3.4, we see from Figure 4.1C that the same control sequence is unstable because the system is directed away from the fixed point.

If α is further increased, then a new control sequence is achieved. Figure 4.1D shows a stable 011011... sequence for $\beta = -5.76$. In this case, the first perturbation is so large that the controlled iterate is also above the line of identity, implying that the next iterate is also controlled. The second controlled iterate is below the line of identity and below the fixed point, thereby giving the 011011... sequence. In this case, the fixed point is stabilized because the second controlled iterate is directed closer to the fixed point. However, larger values of β give an unstable 011011... sequence (not shown) because the second controlled iterate is directed farther from the fixed point.

Just like the transition from the stable 0101... sequence to the stable 001001... sequence depicted in Figures 4.1A and B, there is a transition from the stable 011011... sequence to the stable 00110011... sequence as β is further decreased (Figure 4.1E shows the case for $\beta = -5.798$) and the 00110011... sequence becomes unstable as β is decreased still further (Figure 4.1F depicts $\beta = -5.82$).

For the linear system (4.6), the progression of unstable and stable periodic control sequences continues indefinitely as β is decreased. In other words, the switching parameter Θ_n imposes the following progression of control sequences: unstable 01^k, stable 01^k, stable 001^k, unstable 001^k, unstable 01^{k+1}, ..., where 1^k denotes k control perturbations in a row before the sequence repeats and k progresses from one to infinity as β is decreased from zero.

4.4.2 Computation of the Stability Zones[1]

Since we know the progression of the control sequences imposed by the switching term Θ_n, X_{k+1} can be expressed as:

$$X_{k+1} = e_k X_0, \tag{4.7}$$

where e_k is given by the following iterative expression:

$$e_k = (A - \beta)e_{k-1} + \beta e_{k-2} \tag{4.8}$$

with $e_0 = A$ and $e_1 = A^2 + \beta(1 - A)$ or $e_1 = A^2$ for the 01^k or 001^k sequences respectively. In this study, we consider the case $A < -1$ since that is when the fixed point is unstable.

The boundaries of the stability zones are computed by using the criterion that stable sequences move the system closer to the fixed point after one control sequence. Since X_{k+1} is the last iterate of the first 01^k control sequence and X_{k+2} is the last iterate of the first 001^k sequence, the stability conditions are $e_k < 1$ and $e_{k+1} < 1$ for the 01^k and 001^k sequences respectively. Therefore, the boundaries are given by k degree polynomials in β. For example, the $k = 1$ control sequences are stable for $1 + A + 1/A \leq \beta \leq 1 + A$ for $A < -1$. Figure 4.2 depicts the stable zones for $k = 1$ and $k = 2$. The condition $e_k = 0$ marks the boundary between the stable 01^k and 001^k sequences (grey lines in Fig. 4.2) where the fixed point is reached after a single control sequence 01^k.

The striking feature of this analysis is that the domain of control is extended by the restriction. Figure 4.2 shows that the linearized system has stable sequences for an arbitrarily negative slope A. This contrasts with the unrestricted system, whose control domain is bounded by the dashed lines in Figure 4.2, that can only stabilize fixed points with slopes greater than -3.

While there are an infinite number of stable zones corresponding to an arbitrary

[1]The stability zones were independently discovered by Socolar and Gauthier [8] using different techniques.

number k control perturbations in a row, the stability zones are bounded by the curve $\beta = A - 2 - 2\sqrt{1-A}$. This boundary is computed by recognizing that as k approaches infinity, the control is always on such that $X_{n+1} > X_n$ for every iterate. Thus, the algorithm behaves just like the unrestricted control (4.3) with real eigenvalues greater than one – a condition met only when β is below the boundary.

4.4.3 Experimental Observation of different control sequences

Although our experimental cardiac system was not linear, application of the restricted control algorithm resulted in several of the control sequences predicted in the above linear system. These control sequences were especially clear at the initiation of the control where the control perturbations were relatively large and therefore easy to see.

For example, Figure 4.3A shows the variable X_n and the control parameter λ_n during an unstable 01 sequence for a feedback gain $\alpha = 3.3$. This example corresponds to the initiation of the first control sequence of Figure 3.3C (the baseline value λ_0 is shifted by -55 ms to assist in plotting the data). The first controlled beat is indicated by the arrow and corresponds to a negative perturbation of λ_0 (all control perturbations are negative as imposed by the switching term Θ_n). Since the system is nonlinear, oscilatory growth of X_n is quenched and the original large amplitude alternation of X_n is reduced in magnitude – but not eliminated.

However, as shown in Figure 4.3B (corresponding to the second control sequence shown in Fig.3.3C) when α is increased to 5.0 the system shifts to a stable 001 sequence that eliminates the alternation of X_n. The first controlled beat is indicated by the arrow. After the fourth perturbation to λ_n (beat 323), the system shifts to a stable 0101 sequence. This shift is due to the close proximity of these stable zones (Fig. 4.2) and any noise or drift in the system can cause such transitions.

Figure 4.3C shows a stable 0011 control sequence that eliminated the alternation of X_n in another preparation with $\alpha = 2.5$. Again, the system switches to its adjacent stable 011 control sequence shortly after the control was initiated.

4.5 Automatic adaptation of the feedback gain

The control algorithm requires that the feedback gain parameter α be specified. In our cardiac experiments, we chose α by trial and error. However, the structure of the stability zones suggests a way to automatically adapt α so that X^* can be stabilized more robustly.

Since multiple perturbations away from the fixed point are not desirable, the optimal stability zone is the $k = 1$ zone. Furthermore, since the stable $k = 1$ zone has the largest area, it will be the most robust to noise and drifting system parameters. Therefore, to target this zone we adapt α according to:

$$\alpha_n = \begin{cases} \alpha_{n-1} + \delta\alpha & \text{if } \Theta_{n-4} \text{ to } \Theta_{n-1} \text{ was 0101 or 1010,} \\ \alpha_{n-1} - \delta\alpha & \text{otherwise,} \end{cases} \tag{4.9}$$

where $\delta\alpha$ is a small increment. When $\left(\frac{\partial f}{\partial \lambda}\right)|_{X^*}$ is negative (as in our cardiac experiments) α and $\delta\alpha$ are positive. Otherwise they are negative. This simple algorithm is motivated by examining the stability zones in Figure 4.2. If α is too small then this corresponds to β being above the $k = 1$ boundary and the control sequence will be an unstable 01 sequence. If α is too large, then β is below the optimal 01 boundary depicted by the uppermost grey curve in Figure 4.2. Thus, the adaptation will adjust the system so that it oscillates between the stable 01 and stable 001 sequences provided that the increment $\delta\alpha$ is small enough so that the stepsize of β is sufficiently less than the thickness of the $k = 1$ stability zone.

To illustrate the adaptive algorithm, we used the restricted controller:

$$\lambda_n = \lambda_0 + \Theta_n \frac{\alpha_n}{2}(X_{n-1} - X_n), \tag{4.10}$$

with α_0 randomly chosen between 0 and -10 and $\delta\alpha = -0.1$. We applied (4.10) to the quadratic map:

$$X_{n+1} = \lambda_n X_n(1 - X_n) + \zeta_n, \tag{4.11}$$

where ζ_n is a normally distributed random variable with a mean of zero and a variance of 0.001. Our goal was to stabilize the fixed point $X^* = (\lambda_0 - 1)/\lambda_0$.

Figure 4.4 shows the results for adaptive control of the quadratic map. For iterates 1-500, $\lambda_0 = 3.3$ corresponding to an uncontrolled stable period-2 orbit. Control was initiated at iterate $n = 125$ and the random initial value of α_n was -2.03. The adaptive algorithm stabilized X^* and the subsequent fluctuations of α_n kept the system in the $k = 1$ stability zone. The control was shut off at $n = 375$ and the period-2 cycle returned.

At $n = 501$, λ_0 was switched to 3.52 which corresponds to a period-4 rhythm. The control was initiated at $n = 626$ with a random initial value of $\alpha_n = -8.38$. The adaptive control stabilized X^* and the control was turned off at iterate 876. At $n = 1002$, λ_0 was switched to 3.65 which is in the chaotic regime. Control was initiated at $n = 1127$ with the initial $\alpha_n = -8.32$ and X^* was stabilized after approximately 130 iterates. When the control was shut off at $n = 1378$ the chaos resumed.

Since the adaptive algorithm was designed to track a drifting fixed point, we applied the control to a quadradic map with λ_0 starting at 3.3 and increasing by an increment of 0.007 every iterate. The small increments to λ_0 introduced a slow drift in the system. Control was initiated at iterate 250 and Figure 4.5 shows that the drifting fixed point was tracked and stabilized well into the chaotic regime.

4.6 Conclusion

The biological restriction of unidirectional control perturbations surprisingly enhances the controllability of systems described by one-dimensional maps. Since biological systems typically drift over time, dynamic control algorithms must adapt to these changes. The restricted delayed feedback control technique allows for moderate tracking of the fixed point as long as the system remains in a stability zone. However, a simple modification of the restricted control algorithm allows for automatic adaptation of the previously fixed feedback gain parameter to ensure that the drifting system is directed to, and remains in, the largest stability zone.

BIBLIOGRAPHY

[1] W. L. Ditto, S. N. Rauseo, and M. L. Spano. Phys. Rev. Lett. **64,** 3211 (1990); E. R. Hunt. Phys. Rev. Lett. **67,** 53 (1991); B. Peng, V. Petrov, and K. Showalter. J. Phys. Chem. **95,** 4957 (1991).;V. Petrov, B. Peng, and K. Showalter. J. Chem. Phys. **96,** 7505-7513 (1992); R. Roy, T. W. Murphy, T. D. Maier, Z. Gills, and E. R. Hunt. Phys. Rev. Lett. **68,** 1259 (1992). T. L. Carroll, I. Triandaf, I. B. Schwartz, and L. Pecora. Phys. Rev. A **46,** 6189 (1992); Z. Gills, C. Iwata, R. Roy, I. B. Schwartz, and I. Triandaf. Phys. Rev. Lett. **69,** 3169 (1992); I. B. Schwartz, and I. Triandaf. Phys. Rev. A **48,** 718 (1993); V. Petrov, M. J. Crowley, and K. Showalter. Phys. Rev. Lett. **72,** 2955 (1994); N. F. Rulkov, L. S. Tsimring, and H. D. I. Abarbanel. Phys. Rev. E **50,** 314 (1994).

[2] A. Garfinkel, M. L. Spano, W. L. Ditto, and J. N. Weiss. Science **257,** 1230-1235 (1992); S. J. Schiff, K. Jerger, D. H. Duong, T. Chang, M. L. Spano, and W. L. Ditto. Nature **370,** 615-620 (1994).

[3] K. Hall, D. J. Christini, M. Tremblay, J. J. Collins, L. Glass, and J. Billette, Phys. Rev. Lett. **78**, 4518-4521 (1997).

[4] D. J. Christini and J. J. Collins. CHAOS **7**, 544-549 (1997).

[5] T. Shinbrot, C. Grebogi, E. Ott, and J. Yorke, Nature **363**, 411-417 (1993).

[6] K. Pyragas, Phys. Lett. A **170**, 421-428 (1992).

[7] T. Ushio, IEEE Trans. Circ. Sys. **43**, 815-816 (1996).

[8] J. E. S. Socolar and D. J. Gauthier, Phys. Rev. Lett. **79**, 4938 (1997).

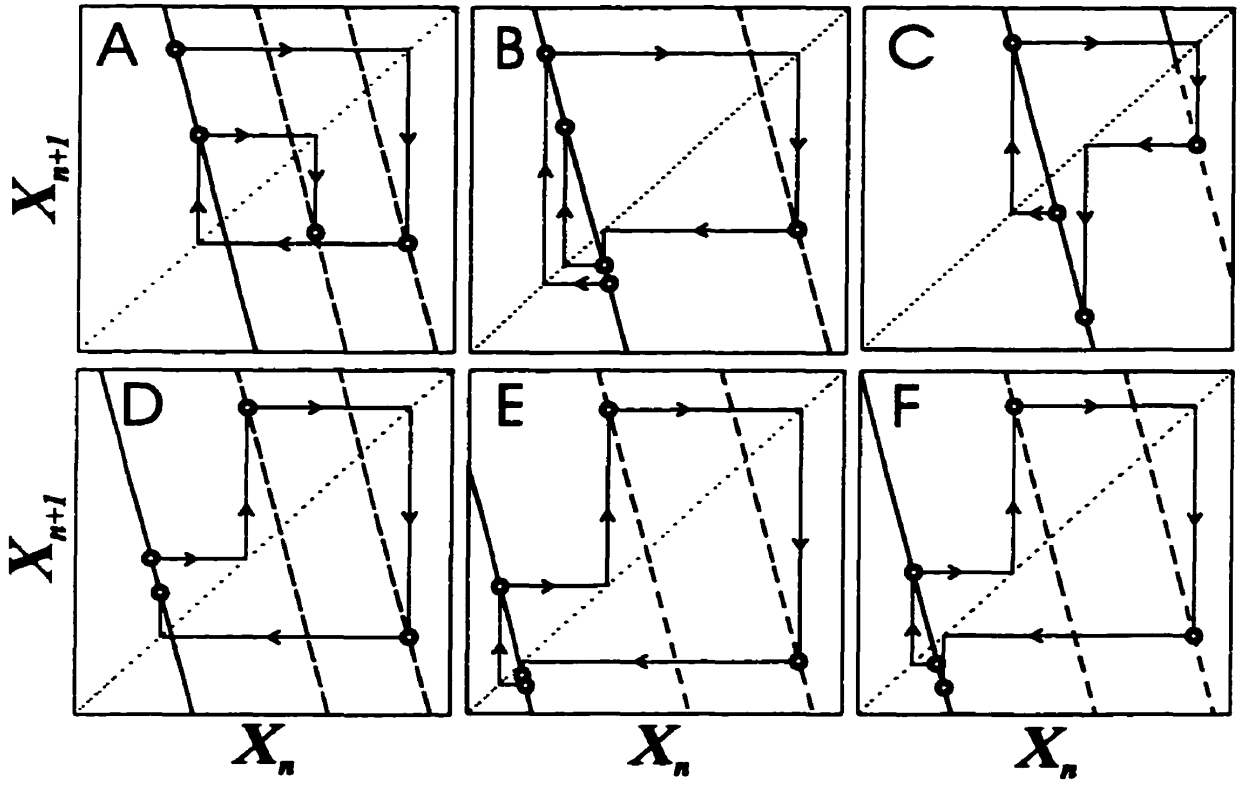

Figure 4.1: Return maps showing the progression of control sequences as β is decreased. The dotted diagonal line is the identity line and the solid line is the uncontrolled system with slope $A = -4$. The dashed lines shows the system when perturbed by control interventions. A) $\beta = -3.1$ results in a stable 01 control sequence. B) $\beta = -3.23$ results in a stable 001 sequence. C) $\beta = -3.4$ gives an unstable 001 sequence. D). $\beta = -5.76$ gives a stable 011 sequence. E) $\beta = -5.798$ gives a stable 0011 sequence. F) $\beta = -5.82$ gives an unstable 0011 sequence.

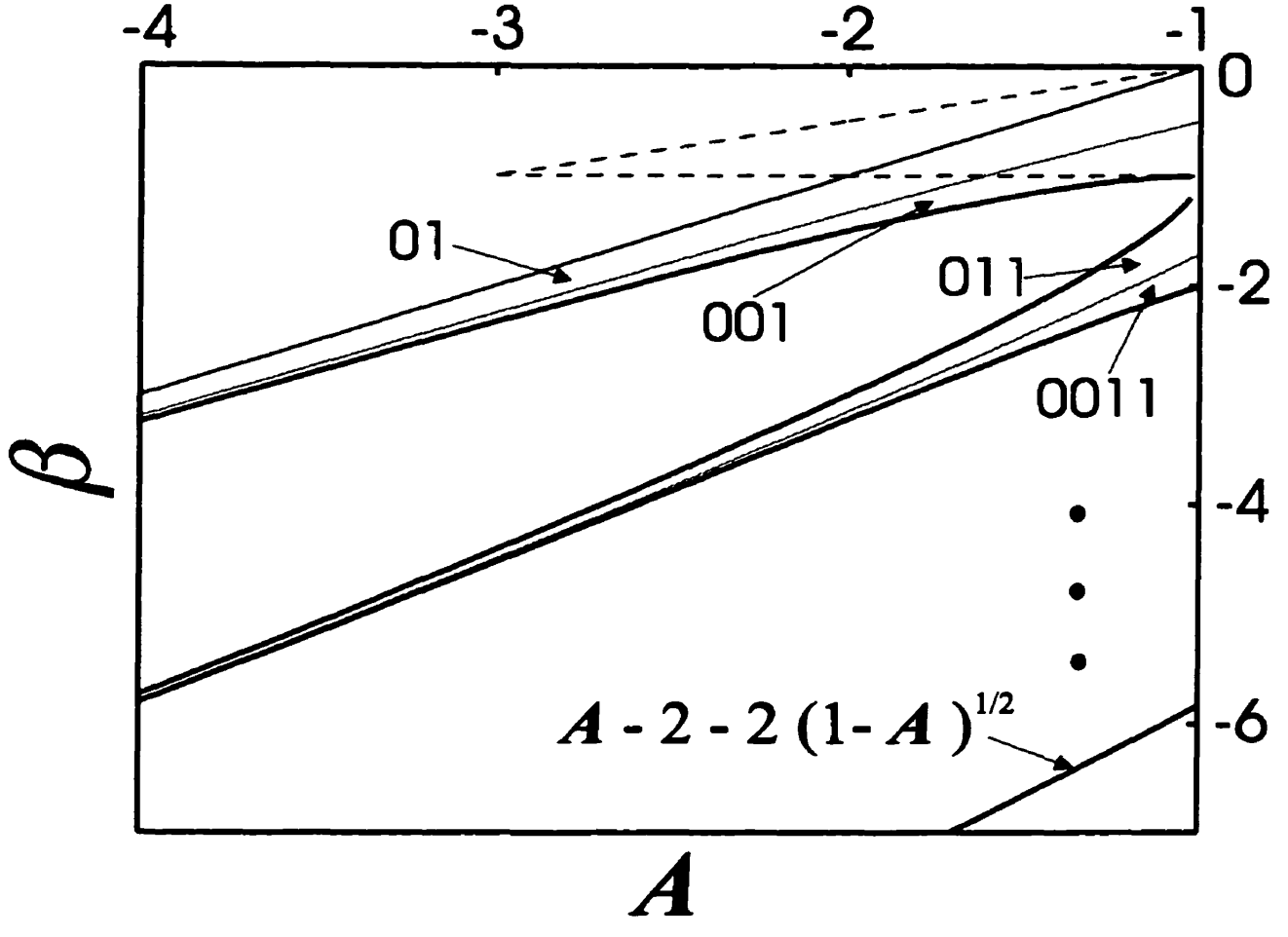

Figure 4.2: Stability zones of restricted control. The $k = 1$ and $k = 2$ stability zones are indicated. The grey lines inside the zones mark the transition from 01^k to 001^k. The dots indicate that there are an infinite number of stability zones for larger number k perturbations in a row. The infinite sequence of stability zones is bounded by the curve $\beta = A - 2 - 2\sqrt{1 - A}$.

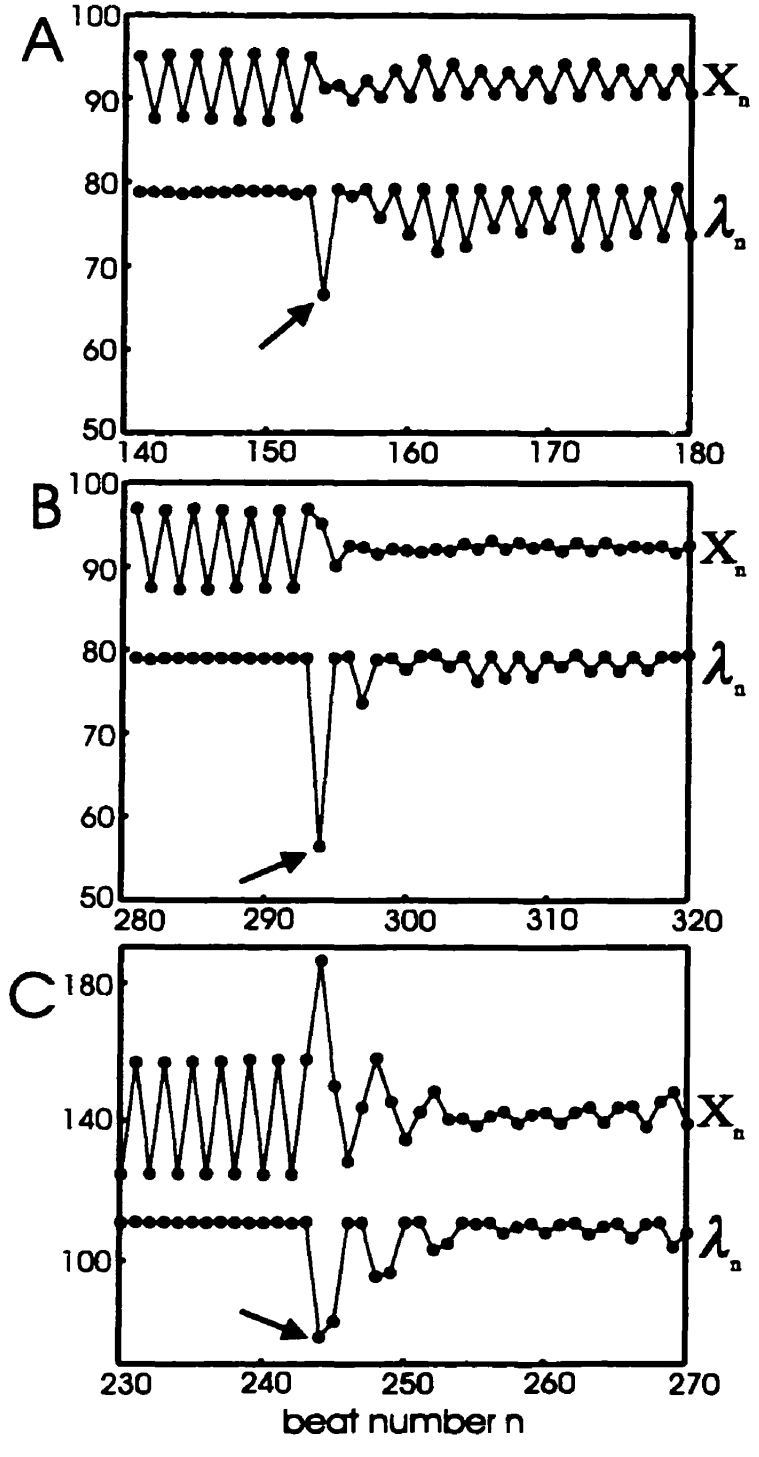

Figure 4.3: Experimentally observed control sequences. The first control perturbation is indicated by the arrow. A) An unstable 01 sequence for $\alpha = 3.3$. B) The same preparation with $\alpha = 5.0$. In this case the control begins in a stable 001 sequence and shifts to a stable 01 sequence. C) A stable 0011 sequence shifting to a stable 011 sequence in a different preparation with $\alpha = 2.5$.

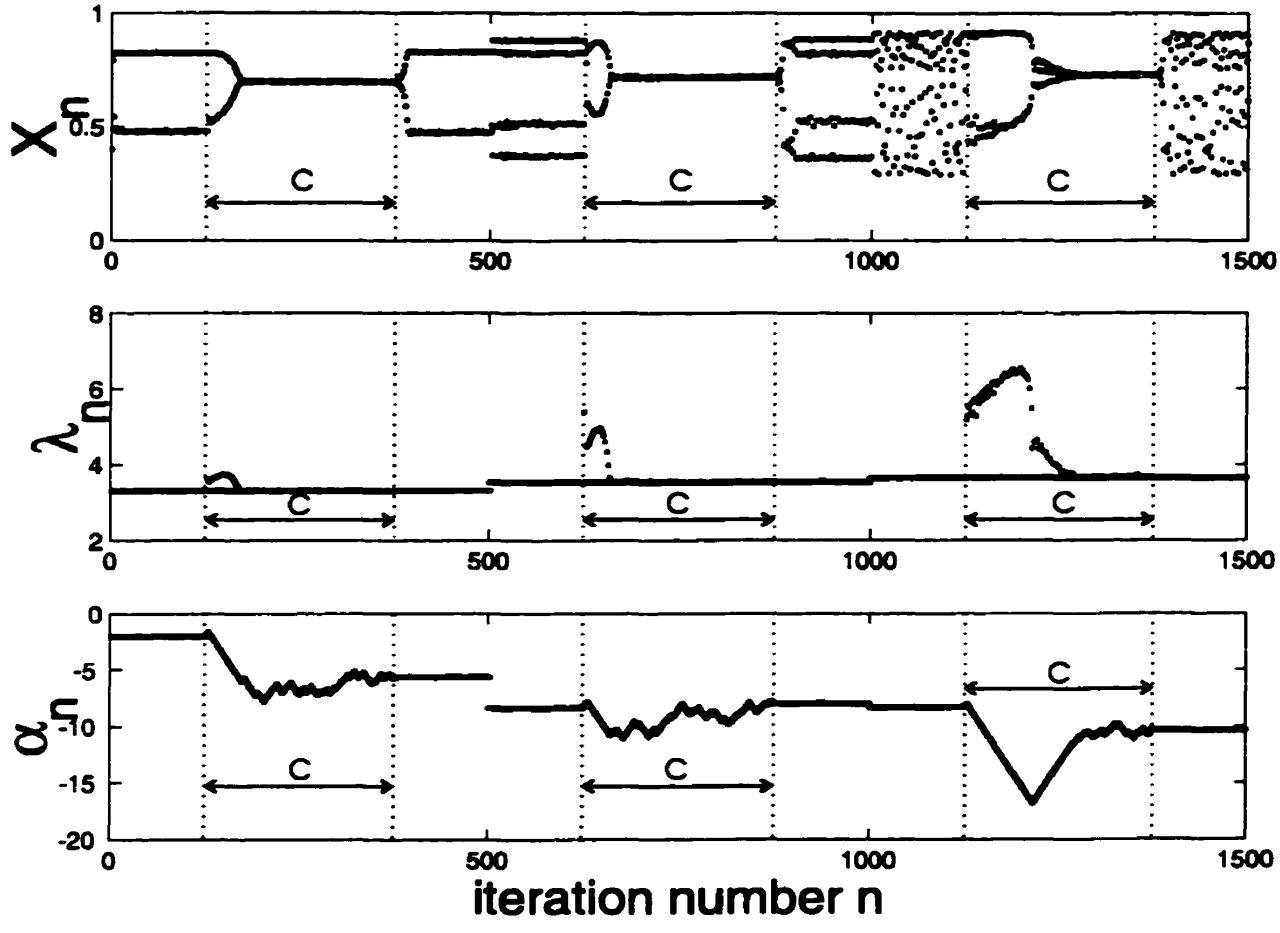

Figure 4.4: Adaptive control of the quadratic map. Control was implemented in the intervals labelled with a "C". Iterates 1-500, 501-1001, and 1002-1500 show control of period-2, period-4, and chaotic dynamics respectively.

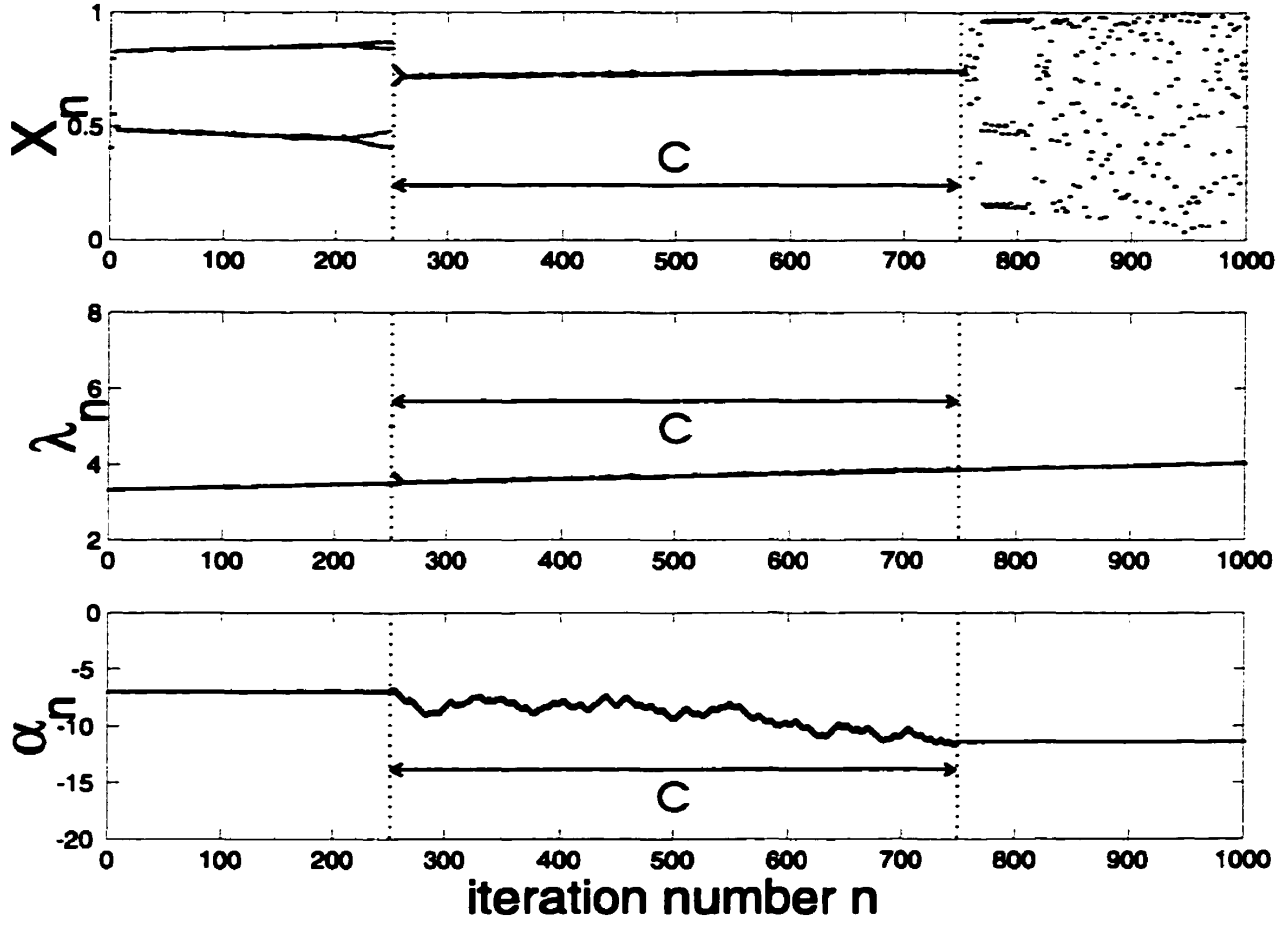

Figure 4.5: Adaptive control of a drifting quadratic map. The baseline value of λ_0 was incremented by 0.007 each iterate causing a slow drift in the system. The adaptive algorithm tracked the drifting fixed point as the system moved into the chaotic regime.

CHAPTER 5

HOW TO TELL A TARGET FROM A SPIRAL: THE TWO PROBE PROBLEM

5.1 Foreward

Targets and spirals are topologically distinct wave patterns that have been observed in a variety of physical, chemical, and biological systems [1, 2]. A target pattern is produced by concentric waves traveling away from a rhythmic source, whereas a spiral wave is generated by a rotating source. Despite their different mechanisms, both wave patterns lead to indistinguishable rhythms when measured at a single point in space. This ambiguity sparked the early debate over the mechanism of the periodic radio waves measured from pulsars[1] [3], and has implications for the mechanisms of several biological rhythms, some of which are life-threatening [2, 4].

Our interest in distinguishing spirals from targets is motivated by a problem in cardiac electrophysiology: targets and spirals underly serious arrhythmias in the heart [4] and cardiologists need to diagnose the mechanism to launch the appropriate therapy. However, cardiac targets and spirals are not readily distinguishable since it is presently impossible to measure a high-resolution activation map in an intact human heart. Rather, a small number of probes can be placed on the heart's inner surface in order to measure local electrical activity and deliver stimuli [5].

Here, we pose the following problem: what is the minimum number of probes required to distinguish a target from a spiral? We show that the answer is two, provided that the waves propagate in an "excitable" medium, like the heart.

[1] Periodic radio waves may be caused by a stationary "pulsating" source or a rotating source called a "lighthouse" model.

5.2 Wave Propagation in Excitable Media

An excitable system [1, 6] is characterized by the following properties: i) there is a stable rest state; ii) a suprathreshold perturbation away from the rest state causes an excitation (i.e. a "large" excursion in phase space); and iii) after an excitation, there is a refractory time period when another perturbation will not give a new excitation [6]. When excitable elements are coupled together in space, the resulting excitable medium can support excitation waves.

A local stimulus delivered to an excitable wave pattern can cause a global spatio-temporal change. For example, a time-shift of the wave pattern is caused by a sufficiently large stimulus delivered at the right time and location [7, 8]. The time-shift of the rhythm is called phase resetting, or simply resetting (Fig. 5.1).

We will show that stimuli delivered at a single probe cannot distinguish between a target pattern and a spiral wave. However, targets and spirals can be distinguished by interchanging the stimulus location between two probes and measuring the resetting response for both arrangements. This procedure identifies the wave pattern by exploiting the different spatio-temporal symmetry properties of targets and spirals.

5.3 Target and Spiral Phase Fields

Let $\tau(\mathbf{r})$ be the time when the wavefront passes through the position $\mathbf{r}$. A probe located at $\mathbf{r}$ records $\tau(\mathbf{r})$ as the time at which the activation variable crosses some threshold. The spatio-temporal activation pattern can be described by identifying the phase of the rhythm ϕ at all locations and times t:

$$\phi(\mathbf{r}, t) = \frac{t - \tau(\mathbf{r})}{T_0} \pmod 1, \tag{5.1}$$

where ϕ advances from 0 to 1 with the period of the rhythm. The local phase difference measured at locations $\mathbf{r_1}$ and $\mathbf{r_2}$ is determined by the time delay between

the activation of probes at different locations:

$$\phi(\mathbf{r}_1, t) - \phi(\mathbf{r}_2, t) = -\frac{\Delta t_{12}}{T_0}, \tag{5.2}$$

where $\Delta t_{12} = \tau(\mathbf{r}_1) - \tau(\mathbf{r}_2)$ is the time difference between the activation of probes p_1 and p_2.

The phase field of a target pattern is given by

$$\phi(r, \theta, t) = \frac{t}{T_0} - \frac{r}{cT_0} \pmod 1, \tag{5.3}$$

where c is the propagation velocity[2] and (r, θ) are the radial and angular coordinates of a polar coordinate system with the origin at the center of the pacemaker region. The spiral phase field is given by:

$$\phi(r, \theta, t) = \frac{t}{T_0} + \psi(r) + \frac{\theta}{2\pi} \pmod 1, \tag{5.4}$$

where $\theta = -\,2\pi\,\psi(r)$ describes the shape of the spiral wave-front rotating clockwise around a circular obstacle at the origin [9].

5.4 Symmetry Properties of Targets and Spirals

The target and spiral phase fields have different symmetry properties. Let the operator $\widehat{R}_\varphi$ denote a rotation of the plane about the origin by an angle φ and let $\widehat{T}_t$ denote a time translation by an amount t. The symmetry properties of the two phase fields are expressed by their invariance under the following transformations:

$$\begin{aligned} \text{target:} \quad & \widehat{R}_\varphi\, \phi(\mathbf{r}, t) = \phi(\mathbf{r}, t), \quad \forall\, \varphi \\ \text{spiral:} \quad & \widehat{T}_{t^*} \widehat{R}_\varphi\, \phi(\mathbf{r}, t) = \phi(\mathbf{r}, t), \quad t^* = \frac{\varphi T_0}{2\pi}. \end{aligned} \tag{5.5}$$

[2]Because of curvature effects, the propagation velocity c generally depends on the distance r from the pacemaker. For simplicity, we have taken c to be a constant. Nevertheless, our results apply provided that the time for a wave to propagate from the pacemaker to the stimulus probe is approximately equal to the time for the stimulus wave to propagate to the pacemaker.

Thus, the target pattern is invariant under a rotation about an arbitrary angle, whereas the spiral pattern is invariant under a rotation combined with a particular time translation. We will show how two probes can be used to reveal the different symmetry properties by measuring the resetting response of the wave patterns.

5.5 Phase Resetting Targets and Spirals

To illustrate our technique, we investigated the effects of stimuli on a target pattern and a spiral wave rotating around a circular obstacle in the modified FitzHugh-Nagumo model:

$$\begin{aligned} \frac{\partial v}{\partial t} &= \frac{1}{\epsilon}(v - \frac{1}{3}v^3 - w) + D\nabla^2 v + I_{loc} + I_{stim}(t), \\ \frac{\partial w}{\partial t} &= \epsilon(v + \beta - \gamma w)g(v) \end{aligned} \tag{5.6}$$

where v is the excitation variable, w is the recovery variable, $\beta = 0.7$, $\gamma = 0.5$, and $\epsilon = 0.3$. The diffusion coefficient $D = 1$ cm^2 s^{-1}. I_{loc} is a constant current applied to a localized region at the center of the sheet in order to either make it oscillate, mimicking a pacemaker, or depress excitability thereby creating an obstacle around which a spiral wave can propagate. $I_{stim}(t)$ is a pulsatile stimulation current used for resetting. The sigmoidal function $g(v) = (w_H - w_L)/(1 + e^{-kv}) + w_L$ controls the rate of the pacemaker, where $k = 4.0$, $w_H = 0.6$, and $w_L = 0.13$ in the pacemaker region and 0.4 everywhere else. For the spiral wave $k = 4.0$, $w_H = 0.6$, and $w_L = 0.4$. The equations were solved using a simple Euler integration scheme on an 80×80 grid with zero-flux boundary conditions, a spatial discretization of 0.4 mm and a time step of 0.05 ms[3]. Figure 5.1 shows resetting of a target and a spiral with periods T_0 of 59.7 ms and 47.7 ms respectively. We

[3]Halving either the time step or spacial discretization step decreases the period of the rhythm by less than 0.2% and points on the resetting curves are changed by less than 1%. Thus, we can be confident of convergence of our numerical algorithm.

measured the activity at two probes labeled p_1 and p_2 and delivered the stimuli to probe p_1.

The local phase ϕ_i of the stimulus is measured at both probes. The effect of the stimulus is determined by measuring the successive activation times since the activation prior to the stimulus $T_1^{(i)}$, $T_2^{(i)}$,..., $T_j^{(i)}$ where the index i indicates the probe and the index j indicates the number of activations since the stimulus was delivered (Fig. 5.2A) [7]. The local activation times $T_j^{(i)}$ depend on both the phase and the location of the stimulus.

Figure 5.2B shows the normalized resetting curves for the spiral and target patterns using stimuli delivered and measured at probe p_1. The local phase measurements at probe p_2 is given by equation (5.2). Furthermore, the resetting curves measured at p_2 are given by:

$$T_j^{(1)}(\phi_1) = T_j^{(2)}(\phi_2 - \frac{\Delta t_{12}}{T_0}), \tag{5.7}$$

for j large enough so that the transient effects of the stimulus have dissipated. Thus, the resetting curves measured at different probes are related by a horizontal shift equal to the phase lag between the probes (not shown). This is a general result expressing the fact that the resetting response of the rhythm is independent of the measurement location.

The resetting curves obtained at the stimulus probe are strikingly similar for both targets and spirals (Fig. 5.2B). The similarity is easily explained. Early stimuli fall in the refractory and therefore have no effect on the rhythm. Such stimuli give the flat part on the left of the resetting curve. On the other hand, a late stimulus results in a new wave that is annihilated before interacting with the pacemaker or the tip of the spiral. Thus, late stimuli fall in an "interference zone" and also have no effect on the rhythm. Only stimuli at intermediate phases reset the rhythm and result in the diagonal part of the resetting curve.

Therefore, the resetting curve measured at the stimulation probe is divided into three zones: the refractory zone at small phases, the resetting zone at interme-

diate phases, and the interference zone at late phases. The stimulus phase ϕ^* marks the juncture between the resetting and interference zones.

The position of ϕ^* is determined by the distance between the stimulation probe and the source of the rhythm. Since a resetting stimulus must generate a wave that interacts with the source, the stimulus must be delivered early enough so that the wave has time to travel interact with the pacemaker or the tip of the spiral. A wave generated by a late stimulus will be annihilated by the original target or spiral wave before interacting with the source. Therefore, the greater the distance from the source, the smaller the junction phase ϕ^*.

Figure 5.2C shows the resetting curves measured at the stimulation probe p_2. Comparing with the resetting curves from stimuli delivered at p_1 (Fig. 5.2B), we find that $\phi_2^* < \phi_1^*$ for both the target and the spiral, implying that p_2 is farther from the source than p_1.

5.6 Distinguishing a Target from a Spiral

5.6.1 Homogeneous Media

Because of the rotational symmetry of the target pattern, the time delay between activation of the probes depends on their relative distance from the source: $\Delta t_{12} = (r_1 - r_2)/c$. Therefore, for a target pattern the time delay between the activation of two probes predicts the shift of the junction phase ϕ^* resulting from interchanging the stimulation site between the probes:

$$\phi_1^* - \phi_2^* = -\frac{2\Delta t_{12}}{T_0}, \tag{5.8}$$

where ϕ_i^* is the juncture phase measured at the stimulus site i. The factor of 2 arises from equation (5.2) since the phase measurements are made at their respective stimulation sites. Since the spiral pattern lacks rotational symmetry, probe activation delays alone cannot predict the change in the interference zones

caused by interchanging the location of the stimulus. Therefore, targets and spirals can be distinguished on this basis.

To illustrate this symmetry property, we applied prediction (5.8) in our simulations of the FitzHugh-Nagumo model. From Figure 5.2B, we find that $\phi_1^* = 0.57$ and 0.84 for the target and spiral patterns respectively. Similarly, Figure 5.2C shows that $\phi_2^* = 0.45$ for the target and $\phi_2^* = 0.68$ for the spiral. The activation time delays were Δt_{12} = -3.5 ms for the target and Δt_{12} = 8.0 ms for the spiral. Thus, as expected, (5.8) is satisfied for the target pattern but not for the spiral for this arrangement of probes.

Whereas a target pattern satisfies (5.8) for any two probes positions, a spiral pattern will satisfy (5.8) only in the special case where the probes are placed along a curve whose shape depends on the shape of the spiral. Measurement uncertainties may also lead to 5.8 being satisfied for a spiral. For example, in the real heart it is likely that the largest uncertainties are associated with measuring the junction phases ϕ_1^* and ϕ_2^*. Since the junction phases appear as a difference on the left side of equation (5.8), their absolute uncertainties add together and equation (5.8) may be satisfied within experimental uncertainty even for a spiral. Thus, failure to satisfy (5.8) rules out a target pattern, but resetting from more than two probes should be used to confirm a target.

5.6.2 Heterogeneous Media

Although our analysis is based on the rotational symmetry properties of target patterns in homogeneous media, equation (5.8) is also satisfied for target patterns with broken rotational symmetry arising from anisotropic wave propagation. Provided that the time for a wave to propagate from the pacemaker to the stimulus probe is approximately equal to the time for the stimulus wave to propagate to the pacemaker, the broken rotational symmetry is compensated by the anisotropic propagation of waves generated by stimuli. Thus, equation (5.8) can be used to identify topological target patterns.

For example, Figure 5.3A shows a highly distorted target pattern with a period of $T_0 = 61.6$ ms that was produced by inhomogeneous anisotropic diffusion. This pattern was created by integrating equation (5.7) on a domain with four randomly chosen squares of average size 30×30 grid points where each square was assigned random diffusion coefficients, averaging 1 $cm^2\ s^{-1}$ in one direction and 1.5 $cm^2\ s^{-1}$ in the perpendicular direction. Elsewhere, the diffusion coefficients were assigned the average values[4]. We measured the activity at p_1 and p_2 and found that $\Delta t_{12} = 0.8$ ms. The curves in Figure 5.3B show the resetting response for stimuli delivered at p_1 (left panel) and p_2 (right panel). We find that $\phi_1^* = 0.55$ and $\phi_2^* = 0.58$, thereby confirming that equation (5.8) is satisfied for the distorted target pattern.

Since inhomogeneity and anisotropy do not affect our ability to identify a distorted target pattern, our techniques will work in excitable media with complex wave propagation. Furthermore, our technique also applies to target patterns in three dimensions since they are also described by the rotationally symmetric phase field (5.3).

5.7 Conclusion

Targets and spirals are believed to correspond to different mechanisms of cardiac arrhythmia with different therapies [4, 5, 10]. Therefore, distinguishing between them is of crucial clinical importance. Our two probe diagnostic technique uses resetting stimuli to identify the geometry of the propagating waves. Since resetting stimuli are routinely used for other diagnostic purposes [5, 11], we suggest that cardiologists will be able to use our method to distinguish targets from spirals in clinical settings.

[4]The source code for choosing the diffusion coefficients is presented in Appendix B.

BIBLIOGRAPHY

[1] S. K. Scott, *Oscillations, Waves, and Chaos in Chemical Kinetics* (Oxford Univ. Press, Oxford, 1994); *Waves and Patterns in Chemical and Biological Media*, edited by H. L. Swinney and V. I. Krinsky (MIT/North-Holland, Cambridge, MA,1992); R. Suzuki, Adv. Biophys.**9**, 115 (1976); M. W. Mueller, W. D. Arnett, Astrophys. J. **210**, 670 (1976).

[2] G. Bub, L. Glass, N. G. Publicover, A. Shrier, PNAS **95**:10283 (1998); L. Glass, M. C. Mackey, *From Clocks to Chaos: The Rhythms of Life* (Princeton University Press, Princeton, 1988); N. A. Gorelova, J. Bures, J. Neurobiol. **14**:353 (1983); A. T. Winfree, *The Geometry of Biological Time* (Springer-Verlag, New York, 1980); K. Hara, P. Tydeman, M. Kirschner, PNAS **77**: 462 (1980); V. I. Koroleva, J. Bures, Brain Res. **173**:209 (1979); M. Shibata, J. Bures, J. Neurobiol. **5**:107 (1974).

[3] A. Hewish, Sci. Am. **219**(10), 25 (1968).

[4] L. Glass, Physics Today **45**, No. 8, 40 (1996); J. M. Davidenko, A. M. Pertsov, R. Salomonsz, W. Baxter, and J. Jalife, Nature **355**, 349 (1992); A. T. Winfree, *When Time Breaks Down* (Princeton Univ. Press, Princeton, 1987); M. A. Allessie, F. I. M. Bonke, and F. J. G. Schopman, Circ. Res. **33**, 54 (1973);.

[5] M. E. Josephson, *Clinical Cardiac Electrophysiology: Techniques and Interpretation*, 2nd ed. (Lea & Febiger, Philadelphia, 1993).

[6] J. Keener, J. Sneyd. *Mathematical Physiology* (Springer-Verlag, New York, 1998); J. J. Tyson, J. P. Keener, Physica D **32**:327 (1988).

[7] L. Glass and M. E. Josephson, Phys. Rev. Lett. **75**, 2059-2062 (1995); T. Nomura and L. Glass, Phys. Rev. E **53**, 6353-6360 (1996);

[8] V. I. Krinsky, V. N. Biktashev, and A. M. Pertsov, Ann. N. Y. Acad. Sci. **591**, 232 (1990); W. Quan and Y. Rudy, Circ. Res. **66**, 367 (1990); PACE **14**, 1700 (1991); Y. Rudy, J. Cardiovasc. Electrophysiol. **6**, 294 (1993); J. M. Davidenko, R. Salomonsz, A. M. Pertsov, W. T. Baxter, and J. Jalife,

Circ. Res. **77**, 1166 (1995); L. Boersma, J. Brugada, C. Kirchhof, and M. Allessie, Circulation **89**, 852 (1994).

[9] A counter-clockwise rotation is described by changing the sign of the $\theta/2\pi$ term in the spiral phase field. See J. D. Murray, *Mathematical Biology*, 2nd ed. page 348 (Spinger-Verlag, Berlin, 1993).

[10] We have developed a geometrical technique for localizing abnormal pacemakers. K. Hall and L. Glass, in press J. Cardiovasc. Electrophysiol. (1999).

[11] H. C. Strauss, A. L. Saroff, J. T. Bigger, E. G. V. Giardina, Circulation **47**: 86 (1973); B.H. Sarter, D. Schwartzman, D.J. Callans, C.D. Gottlieb, F.E. Marchlinski, J. Cardiovasc. Electrophysiol. **7**:1082 (1996); H. Kottkamp, G. Hindricks, H. Shenasa, X. Chen, T. Wichter, M. Borggrefe, G. Breithardt, *ibid* **7**:916 (1996); M. Tritto, P. Calabrese, *ibid* **7**:632 (1996); K. Asami, F. Suzuki, H. Ashikawa, K. Hiejima, J. Electrocardiol. **29**:149 (1996); D. J. Callens, M. Zardini, C. D. Gottlieb, M. E. Josephson, J. Am. Coll. Cardiol. **27** 1106 (1996).

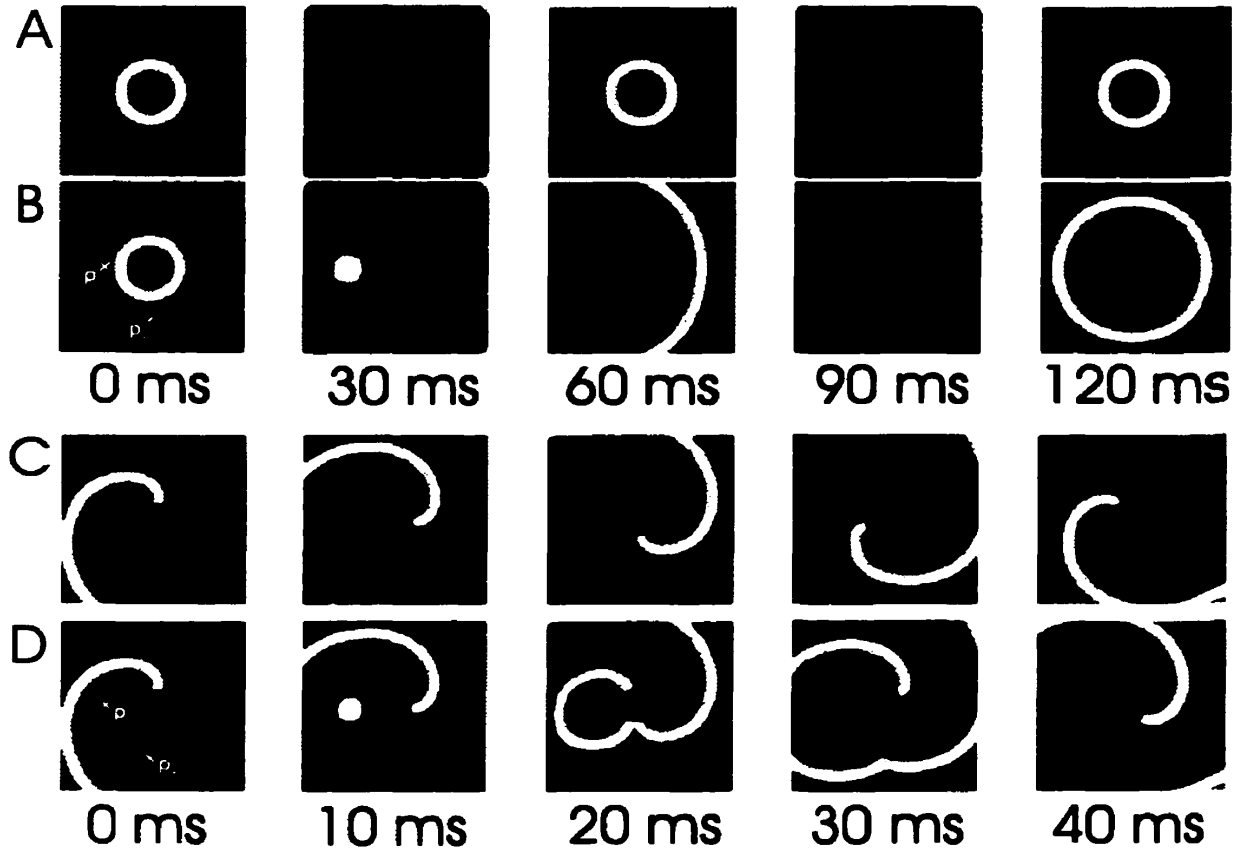

Figure 5.1: Resetting of a target pattern and a spiral wave. A) A target pattern with period $T_0 = 59.7$ ms generated by a pacemaker at the center of the square. B) The stimulus delivered at p_1 at phase $\phi_1 = 0.4$ results in a wave that causes the pacemaker to fire prematurely and thereby resets the rhythm. C) A spiral wave propagating around a circular obstacle with a period $T_0 = 47.7$ ms. D) The stimulus delivered at p_1 at $\phi = 0.4$ generates a wave that collides with the obstacle and breaks into two waves circulating in opposite directions. The wave traveling in the same direction as the original wave continues on to reset the rhythm. The original wave collides with the oppositely traveling wave and both are annihilated.

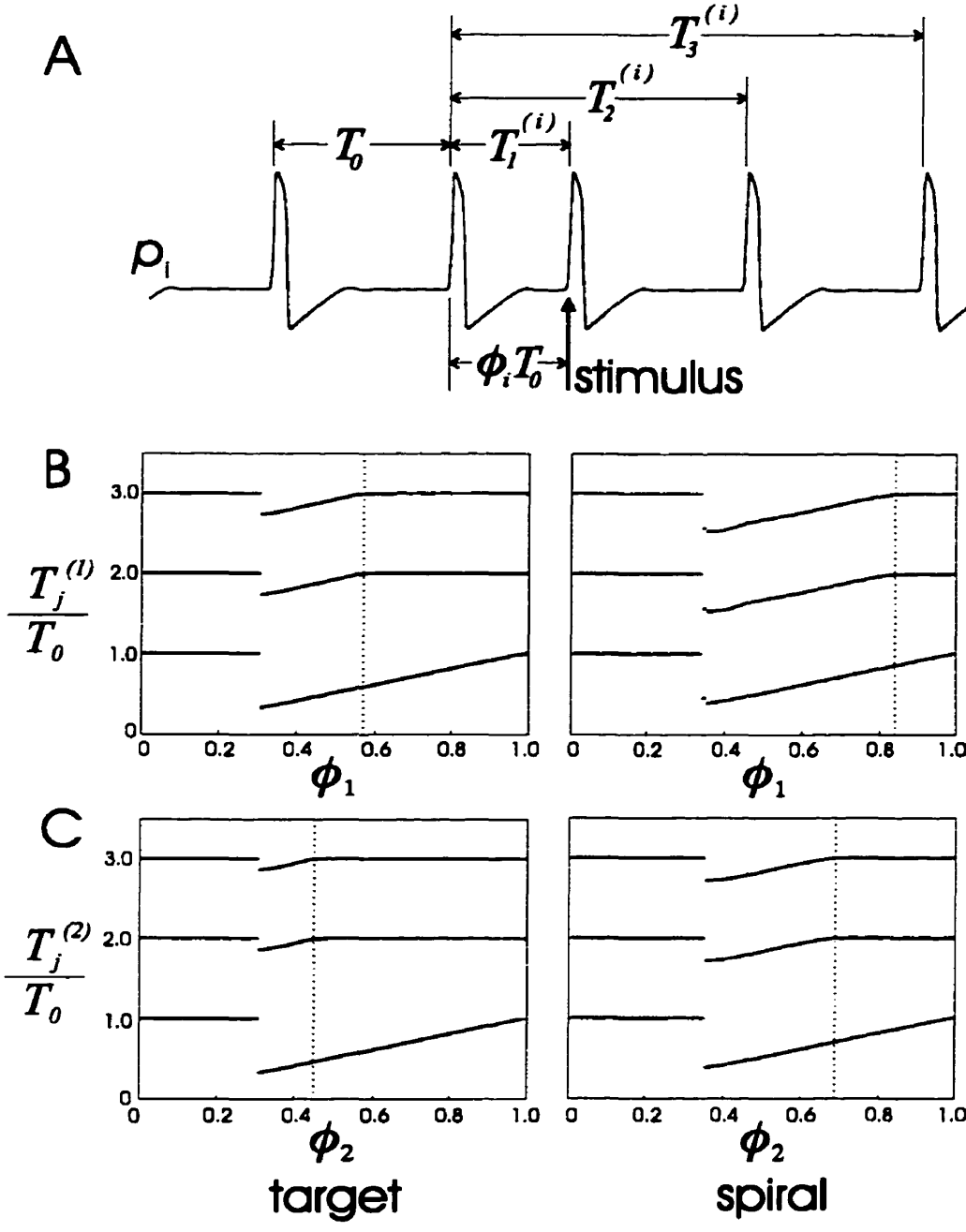

Figure 5.2: Resetting curves for stimuli delivered at p_1. A) Definition of measurements at probe p_i. B) The resetting curves as measured at the stimulus probe p_1 for a target (left) and a spiral (right). The phase ϕ_1^* at the junction between the interference and resetting zones is marked by the dotted vertical line. C) Resetting curves for stimuli delivered at p_2. ϕ_2^* (dotted vertical line) is shifted to the left compared to ϕ_1^* in B) because p_2 is farther from the source of the rhythm. The magnitude of the shift is predicted by equation (5.8) in the case of the target but not for the spiral.

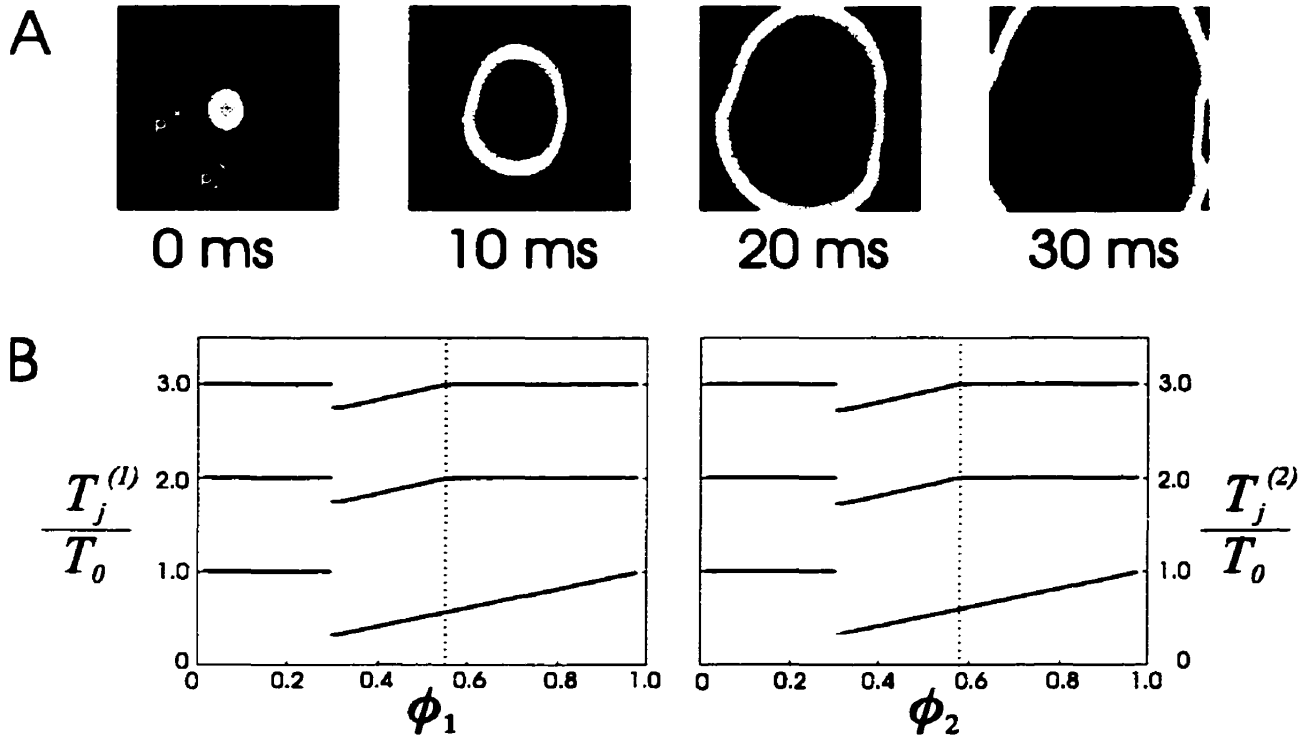

Figure 5.3: A) A distorted target pattern with $T_0 = 61.6$ ms caused by heterogeneous anisotropic diffusion. B) The resetting curve measured at the stimulation site p_1 (left panel) shows that the junction phase $\phi_1^* = 0.55$, wheras the resetting curve measured from stimulation site p_2 (right panel) shows that the junction phase is $\phi_2^* = 0.58$. Equation (5.8) is also satisfied for the distorted target.

CHAPTER 6

LOCATING ECTOPIC FOCI

6.1 Foreward

Ectopic depolarizations can arise from many areas of the heart [1]. Frequent ventricular ectopic beats can be incapacitating in some patients [2], persistent atrial ectopic tachycardia can lead to heart failure [3, 4, 5], and recent reports suggest that atrial fibrillation can be generated by a rapidly firing atrial focus [6, 7, 8]. While ectopic rhythms are often refractory to pharmacological treatment [9, 10, 11], radiofrequency catheter ablation of the ectopic focus is an effective therapy [2, 5, 7, 8, 10, 11, 12, 13, 14].

Locating an ectopic pacemaker is presently achieved by mapping the electrical activation of the endocardial surface in an attempt to find the site of earliest activation [2, 5, 10, 12, 13, 14]. The mapping process is time-consuming and involves much trial and error. As a result, it is sometimes necessary to apply radiofrequency current at several sites before targeting the ectopic focus [2, 5, 7, 10, 12, 13, 14].

We suggest that an ectopic focus can be located by simple geometric strategies using three or more intracardiac electrodes. Specifically, we propose that the site of origin of an ectopic depolarization can be estimated from the activation sequence of electrodes placed away from the ectopic focus. Furthermore, in the case of an on-going ectopic rhythm, the resetting response of the ectopic pacemaker to stimuli applied at an outlying electrode can be used to estimate the distance to the pacemaker.

We devise two localization strategies based on these ideas and test them using a computer simulation of a pacemaker in an excitable sheet. While the basic strategies are sensitive to the electrode arrangement and measurement uncertainties, by iterating our techniques we were able to locate the pacemaker in a

homogeneous isotropic excitable sheet as well as in an inhomogeneous anisotropic sheet.

6.2 Methods

6.2.1 Numerical Simulations

We implemented the following modification of the FitzHugh- Nagumo equations in two spatial dimensions:

$$\begin{aligned} \frac{\partial v}{\partial t} &= \frac{1}{\mu}(v - \frac{1}{3}v^3 - w) + D\nabla^2 v + I_{pace} + I_{stim}(t), \\ \frac{\partial w}{\partial t} &= \mu(v + \beta - \gamma w) f(v) \end{aligned} \tag{6.1}$$

where v is the transmembrane voltage, w is the total slow current, β and γ are constants whose values were chosen to be 0.7 and 0.5 respectively. I_{pace} is a constant current applied to the pacemaker region in order to make it oscillate. $I_{stim}(t)$ is a pulsatile stimulation current used for resetting. The small parameter $\mu = 0.3$ controls the relative time scales of the action potential upstroke and plateau. The sigmoidal function $f(v)$ allows us to control the rate of the pacemaker by adjusting the amount of time spent in phase 4 of the action potential. $f(v)$ also affects the action potential duration. In our simulations

$$f(v) = \frac{(w_H - w_L)}{1 + e^{-kv}} + w_L,$$

where $k = 4.0$, $w_H = 0.6$, and $w_L = 0.13$ in the pacemaker region and 0.4 everywhere else.

The equations were solved using a simple Euler integration scheme with zero-flux boundary conditions, a spatial discretization of 0.4 mm and a time step of 0.05 ms. Simulations for the hyperbolic localization strategy used a 160 × 160 grid whereas the localization by resetting strategy used an 80 × 80 grid.

When simulating homogeneous isotropic excitable media, the diffusion coefficient was chosen to be 1 $cm^2\ s^{-1}$ everywhere. For hyperbolic localization in inhomogeneous anisotropic media, we assigned diffusion coefficients by randomly identifying fifteen squares of average size $52 \times 52 \pm 11$ grid points with each square being assigned random anisotropic diffusion coefficients, averaging $0.9 \pm 0.5\ cm^2\ s^{-1}$ in one direction and $1.9 \pm 0.6\ cm^2\ s^{-1}$ in the perpendicular direction. Elsewhere, the anisotropic diffusion coefficients were assigned the values of 1 $cm^2\ s^{-1}$ in one direction and 2 $cm^2\ s^{-1}$ in the other[1]. For localization by resetting, we randomly assigned anisotropic diffusion coefficients to eight squares of average size $23 \times 23 \pm 8$ grid points. The diffusion coefficients averaged $0.7 \pm 0.5\ cm^2\ s^{-1}$ in one direction and and $2.2 \pm 0.7\ cm^2\ s^{-1}$ in the other direction.

6.2.2 Localization Strategies

Our strategies make the simplifying assumption that the conduction velocity is approximately constant and isotropic. This implies that an impulse generated by the pacemaker propagates radially and creates a circular activation pattern. We measured the time-course of the transmembrane voltage at three electrode positions which were 6 mm apart and arranged along the vertices of a right triangle, thus simulating a catheter. The time of electrode activation was taken to be the time at which the voltage crossed zero. In all of our simulations, we estimated the conduction velocity by stimulating at one electrode and measuring the time delays to activation of the other two electrodes. The conduction velocity was computed using the average of the two time delay measurements, and was calculated once per trial using the initial electrode configuration. Since the radius of an ablation lesion is about 3 mm [21], the ectopic focus was considered to be located if an electrode was placed within 3 mm of the center of the pacemaker region.

[1]The source code for assigning the diffusion coefficients is presented in Appendix B.

Hyperbolic Localization

Our localization technique based on electrode activation sequences is strikingly similar to an artillery localization strategy called "sound-ranging". During World War I, a method was devised for locating long-range enemy guns by listening to a gunshot at three locations. Since the listening posts were different distances from the gun, the gunshot was heard at different times. Each listening post was electrically connected so that the three detonations could be recorded on one chronograph. By measuring the time delays between the recorded gunshots, soldiers could compute the location of the enemy gun [15, 16].

If the gun is analogous to an ectopic focus then the listening posts are like intracardiac electrodes. Subsequent to an ectopic depolarization, a time delay between activation of a pair of electrodes implies that one of the electrodes is closer to the ectopic focus than the other. The difference in distance from the ectopic focus is given by the product of the measured time delay and the conduction velocity. Since the curve defined by a fixed differential distance between two focal points is a hyperbola [15, 17], the ectopic focus lies somewhere on a hyperbola with its foci at the electrodes.

By measuring the time delay to activation of a third electrode, the predicted location of the ectopic focus is at the intersection point of two hyperbolae (Fig. 6.1A). In the Appendix we derive the coordinates of the intersection point and hence obtain the predicted location of the ectopic focus.

Localization by Resetting

Resetting of an ectopic pacemaker using stimuli applied to an electrode away from the pacemaker is identical to the protocol used to measure the sinoatrial conduction time. The standard sinoatrial conduction time test involves delivering premature atrial stimuli at various coupling intervals during a sinus rhythm [18, 19]. A premature stimulus causes a wave of activation to propagate towards the pacemaker. Depending on its timing, the incoming wave may collide with

an outgoing wave generated by the pacemaker. The range of coupling intervals where this happens is called the interference zone. Alternatively, an earlier stimulus generates a wave that invades and resets the pacemaker. By measuring the resetting response to stimuli at various coupling intervals, one can compute the sinoatrial conduction time [18, 19].

We propose that the same protocol can be applied during an ectopic rhythm to measure the conduction time between the stimulation electrode and the ectopic pacemaker. In fact, resetting of an ectopic pacemaker has previously been observed with results similar to that of the sinus node [9, 20]. Given an estimate of the conduction velocity, the distance from the electrode to the ectopic focus can be determined. Therefore, the ectopic focus lies on a circle centered on the stimulation electrode with a radius equal to the distance between the electrode and the pacemaker.

We show in the Appendix that by measuring the times of activation at other sites, we can also determine the distance from these electrodes to the pacemaker. Therefore, the ectopic focus can be localized to the intersection of three circles centered about three electrodes, one of which delivered resetting stimuli (Fig. 6.1B). Alternatively, the coordinates of the ectopic focus correspond to the intersection of the circle centered at the stimulation electrode and a hyperbola determined by the activation delay between the stimulation site and another electrode (Fig. 6.1C). In this case, the activation time of a third electrode is used to discriminate between the two intersection points.

6.2.3 Sensitivity of the localization strategies

The predicted location of the ectopic focus is sensitive to the position, orientation, and arrangement of the electrodes as well as measurement uncertainties. These factors are analyzed in the Appendix. The resulting imprecision means that the predicted location may not correspond to the real ectopic focus - but it is closer than the initial catheter position. Therefore, we expect to converge on the true

ectopic focus by moving the catheter to the predicted location and repeating the localization scheme. Specifically, we moved the catheter such that the electrode that was activated latest was moved to the predicted pacemaker location and the orientation of the catheter was preserved.

6.2.4 Confirmation strategy

Once a putative ectopic pacemaker location has been identified, how can we be sure that it is at the correct location before applying radiofrequency energy? In addition to the established strategies of pace mapping and activation sequence mapping [12, 22], the resetting procedure suggests a new technique to confirm the location of an ectopic pacemaker. If stimuli are delivered directly to the pacemaker, then we expect that the interference zone on the resetting curve will be eliminated. Therefore, a resetting protocol could be used to confirm the location of an ectopic pacemaker, regardless of how the putative location was found.

Since the entire resetting protocol is time-consuming, this may not be a practical confirmation strategy. However, we do not need to determine the exact distance to the pacemaker. We only need to know if we are within the ablation lesion radius r_{abl} which is roughly 3 mm [21]. This can be determined by checking to see if resetting results from a single stimulus delivered at a coupling interval $\widehat{\mathrm{CI}}$ given by:

$$\widehat{\mathrm{CI}} = \mathrm{CL}\left(1 - \frac{2r_{abl}}{v\mathrm{CL}}\right). \tag{6.2}$$

where CL is the cycle length of the ectopic rhythm and v is the conduction velocity. Resetting occurs if the time interval between the stimulus and the next unpaced beat, called return cycle (RC), satisfies the following inequality:

$$\mathrm{RC} < \mathrm{CL}\left(2 - \widehat{\mathrm{CI}}/\mathrm{CL}\right). \tag{6.3}$$

If the stimulus resets the rhythm then the ectopic pacemaker is within the ablation radius of stimulation electrode.

6.3 Results

6.3.1 Hyperbolic Localization

Homogeneous isotropic excitable sheet

A pacemaker with a radius of 1.2 mm was placed at cartesian coordinates (1.6 cm, 1.6 cm) where the origin is at the bottom left corner of a 6.4 cm $\times$ 6.4 cm square of homogeneous isotropic excitable media described by equation (6.1). This produced a periodic circular spread of excitation depicted in Figures 6.2A and B. We measured the activation times of the three electrodes on our simulated catheter and performed 10 trials of hyperbolic localization corresponding to 10 random initial catheter positions and orientations.

Since we knew the relative positions of the electrodes and we estimated the conduction velocity to be 56.9 cm/s, the measured activation delays defined two hyperbolae and the predicted pacemaker location was at their point of intersection. We computed the intersection point using equations (6.9) and (6.10) derived in the Appendix.

In 2 of the 10 trials, the pacemaker was localized after the first iterate. For example, Figure 6.2A shows the results for trial 3 where the intersecting hyperbolae were determined by the depicted initial electrode configuration with measured time delays of 3.0 ms and 5.2 ms. In the other 8 trials, the first iterate gave a predicted pacemaker location that was closer than the initial catheter position, but not within 3 mm of the pacemaker. Subsequent iterates converged on the true pacemaker location in all of the trials. For example, Figure 6.2B shows the results for trial 4 where the pacemaker was located after two iterates. The average number of iterates required to locate the pacemaker was 2.2 $\pm$ 0.8.

Inhomogeneous anisotropic excitable sheet

The irregular, elongated activation pattern of a pacemaker in an inhomogeneous, anisotropic sheet is depicted in Figures 6.2C and D. Again, we measured the activation times of the three electrodes and performed 10 trials of hyperbolic localization corresponding to 10 random initial catheter positions and orientations. The measured conduction velocity was different for each trial depending on the initial catheter location and orientation. The average conduction velocity was 65 $\pm$ 8 cm/s.

Only 1 of the 10 trials (trial 2) located the pacemaker after one iterate (Fig. 6.2C). Rather, an average of 4 $\pm$ 3 iterates were required to locate the pacemaker in 9 out of 10 trials. For example, Figure 6.2D shows the results of trial 9 where the pacemaker was located after 2 iterates. In one trial, the hyperbolic localization failed on the fourth iterate since the computed hyperbolae did not intersect. Nevertheless, the three prior iterates directed the catheter closer to the pacemaker.

6.3.2 Localization by Resetting

Homogeneous isotropic excitable sheet

Due to the computation time required to simulate the resetting protocol, we reduced the size of the excitable sheet to 3.2 cm $\times$ 3.2 cm with the pacemaker being centered at coordinates (0.8 cm, 0.8 cm). The cycle length of the rhythm was 59.7 ms. We performed 5 trials of localization by resetting starting from random initial catheter positions and orientations.

We applied stimulation pulses at various coupling intervals with a magnitude of 1.0 and a duration of 5 ms to a 1.2 mm radius around the electrode that was activated earliest. Figure 6.3A shows the effect of a stimulus given in the interference zone for the initial electrode arrangement in trial 1. Such a stimulus caused a wave of activation to propagate towards the pacemaker, but it was annihilated by an outgoing wave. Therefore, stimuli delivered in the interference

zone had no effect on the pacemaker. Figure 6.3B shows the effect of a resetting stimulus where the wave generated by the stimulus invaded the pacemaker region and resulted in a time-shift of subsequent pacemaker beats.

The extent of resetting was determined by measuring the return cycle (RC), as a function of the coupling interval of the stimulus (CI) (Fig 6.4A). These intervals are typically normalized by dividing by the cycle length (CL) of the rhythm[2][18, 19].

Figure 6.4B depicts the results of our resetting simulations for trial 1. The diagonal dashed line is called the compensatory line and points that fall on this line correspond to an absence of resetting. Thus, stimuli given at coupling intervals in the interference zone gave return cycles that fell on the compensatory line.

As labeled on Figure 6.4B, the height of the plateau of the resetting curve determines the conduction time from the electrode to the pacemaker and back (2CT) [18, 19]. Therefore, the one-way electrode-pacemaker conduction time (CT) is related to the size of the interference zone and is given by:

$$\mathrm{CT} = \frac{1}{2}\mathrm{CL}(1 - \mathrm{CI}^*/\mathrm{CL}), \tag{6.4}$$

where CI^* is the coupling interval at the junction between the interference and resetting zones. For trial 1, $\mathrm{CI}^*/\mathrm{CL}$ was about 0.52 which gave a one-way conduction time of 22.9 ms. Given that the estimated conduction velocity was 56.9 cm/s, the distance from the stimulation electrode to the pacemaker was estimated to be 1.3 cm. Since the activation delay times were 10.1 ms and 15.4 ms, the predicted pacemaker location was at coordinates (0.85 cm, 0.87 cm) corresponding to the intersection of three circles or the intersection of a circle and a

[2]The resulting resetting curves are plotted differently in Chapters 5 and 6 corresponding to the different conventions in the physics literature (Chapter 5) and cardiology literature (Chapter 6). Whereas Chapter 5 plots the normalized time intervals T_j/T_0 versus the stimulus phase ϕ (see Figure 5.2A), Chapter 6 plots the return cycle $\mathrm{RC} \equiv T_2/T_0 - \phi$ versus the normalized stimulus coupling interval $\mathrm{CI/CL} = \mathrm{CI}/T_0 \equiv \phi$ (see Figure 6.4). The relationship between the plots translates to the following rule: horizontal lines transform into diagonals and visa versa. The different "zones" of the resetting curves are important for the analysis and they are labelled consistently in both chapters.

hyperbola (Fig. 6.5A). These intersection points were computed using Appendix equations (6.17) and (6.18) respectively.

In 3 out of the 5 trials, the initial catheter position was too far away to reset the rhythm. In such cases, we reasoned that CI^* was at most equal to the local refractory period around the stimulation electrode which was 20 ms. Therefore, the local refractory period defined a minimum distance to the pacemaker. The localization strategy was iterated using this minimum distance as the radius of the circle centered about the stimulation electrode.

Figure 6.5B shows the results for trial 4. In this case, there was no resetting for the initial catheter position. But after the first iterate of the localization strategy, resetting was observed for stimuli given at normalized coupling intervals shorter than 0.75 and the pacemaker was located on the next iterate. The pacemaker was located in all 5 trials after an average of 1.2 ± 0.4 iterates.

Inhomogeneous anisotropic excitable sheet

In order to test the resetting strategy in an inhomogeneous anisotropic sheet, we simulated a 3.2 cm $\times$ 3.2 cm sheet with a pacemaker at coordinates (0.8 cm, 0.8 cm). The irregular periodic activation pattern is shown in Figures 6.5C and D and the cycle length of the rhythm was 63.9 ms. We performed 5 trials of localization by resetting starting from random initial catheter positions and orientations. The average conduction velocity for the 5 trials was 56 ± 4 cm/s.

An average of 1.4 ± 0.5 iterates were required to locate the pacemaker in 5 out of 5 trials. In 3 out of the 5 trials, the initial catheter position was too far away to reset the rhythm. In these cases, we used the local refractory period of 18.5 ms as our upper estimate of CI^*. Figure 6.5C shows the results of trial 1 where the pacemaker was located after 2 iterates. In 3 cases, movement of the catheter to an erroneous predicted location caused one of the other electrodes to fall in the correct position. For example, Figure 6.5D shows the results of trial 3.

6.3.3 Confirmation strategy

We applied the confirmation strategy to trial 2 of the hyperbolic localization scheme in an inhomogeneous anisotropic sheet where the cycle length was 81.6 ms (Fig. 6.2C). We applied resetting stimuli at the earliest activated electrode and Figure 6.6 shows the resulting resetting curve (•) which had a large interference zone and therefore was not at the true pacemaker location. However, resetting stimuli delivered at the predicted pacemaker location resulted in a resetting curve with no interference zone (○) which suggests that the electrode was at the correct position.

But is the electrode within the 3 mm ablation radius? This question was addressed by checking to see if a single stimulus given at the coupling interval $\widehat{\mathrm{CI}}$ from equation (6.2) resulted resetting according to the inequality (6.3). Since the velocity for trial 2 was estimated to be 66.8 cm/s, equation (6.2) implied that the normalized coupling interval for the single stimulus was $\widehat{\mathrm{CI}}/\mathrm{CL} = 0.89$. The resulting return cycle was 83.9 ms which satisfied the resetting condition (6.3) – but only by 6.6 ms.

6.4 Discussion

In the present study, we suggest that an ectopic focus can be located using measurements from resetting and electrode activation sequences. The hyperbolic localization strategy can be applied to isolated ectopic depolarizations, whereas the resetting strategy can only be used during an on-going ectopic rhythm with a relatively constant cycle length.

By assuming a constant propagation velocity, our localization techniques neglect curvature and recovery effects which are general properties of excitable media. Nevertheless, our simulations showed that the pacemaker region was accurately located by iterating our localization techniques in homogeneous isotropic media as well as inhomogeneous anisotropic media.

Our localization strategies and computer simulations were carried out on a flat surface. This is an obvious but not necessarily fatal flaw of the present formulation. While the heart is clearly not flat, some regions may be thin enough to be approximated by a surface. Our techniques could be used to locate the breakthrough site of an ectopic focus by measuring the shape of the endocardial surface and solving our localization equations in an endocardial coordinate system.

A new electromagnetic mapping technology was recently introduced that could accomplish this task [23, 24]. Catheters with high-resolution location sensors can be dragged over the endocardium thereby creating an anatomical map of the endocardial surface. The relative positions of the catheters with respect to the endocardial surface is determined by integrating the sensed electromagnetic fields to a set of known radiated fields. This technology could be used to automatically compute the predicted location of an ectopic focus in an endocardial coordinate system and efficiently guide the mapping process.

Since our localization techniques require an iteration process before locating the ectopic focus, they must be used in conjunction with a confirmation strategy such as pace mapping [22] or activation sequence mapping [12]. Interestingly, our hyperbolic localization analysis has implications for activation sequence mapping.

Activation sequence mapping works by comparing the activation sequence of several intracardiac recording sites during an ectopic tachycardia with the sequence during pacing at the putative ectopic focus [12]. If the activation sequence is the same then it is assumed that the pacing electrode is at the true ectopic focus. However, our results suggest that depending on the orientation and number of recording electrodes there may be more than one pacing site giving rise to the same paced activation sequence.

For example, if only two recording sites are used then there is a continuum of pacing sites giving the same paced activation sequence, although the morphology of the electrograms would generally vary depending on the stimulation site. In the case of homogeneous isotropic conduction, the continuum corresponds to a hyperbolic curve, but in the real heart we would expect a distorted hyperbola.

Similarly, if three recording electrodes are used then there may be two pacing sites giving the same activation sequence corresponding to two intersection points of hyperbolae. Whether or not one of these sites can be ruled out depends on the orientation and activation sequence of the electrodes, and our hyperbolic localization equations could be used to rule out an alternative ectopic focus. Otherwise, the pacing electrode may be at the wrong spot. This suggests that one should consider the morphology of the electrograms in addition to their timing. Nevertheless, a fourth recording electrode could be used to resolve the ambiguity.

We suggest an additional method for confirming a pacemaker location. While our confirmation strategy was successful in our simulations, it may be difficult to apply in a clinical situation because the cycle length of a clinical ectopic rhythm is typically much longer than what we found in our simulations. Therefore, according to (6.2) and (6.3), our confirmation strategy would require the precise measurement of a very small amount of resetting. This requirement may be impractical due to measurement uncertainties and any variability of cycle length.

Rather than verifying the correct pacemaker site, our confirmation strategy could be used to rule out an erroneous location. As shown in Figure 6.6, stimuli delivered near the pacemaker result in resetting that can be easily measured for a large range of coupling intervals. However, when stimuli are delivered away from the pacemaker, the resetting curve has an interference zone for a moderate range of late coupling intervals. Therefore, a putative pacemaker location can be ruled out if there is no resetting for a stimulus delivered at a moderately late coupling interval. Furthermore, such a stimulus defines a minimum distance from the pacemaker according to equation (6.4).

In conclusion, simple geometric strategies can be used to locate a pacemaker in both a homogeneous isotropic excitable sheet as well as an inhomogeneous anisotropic sheet. The sensitivity of the localization strategies requires that they be iterated in order to find the pacemaker. Since the iterates converge rapidly on

the ectopic focus, our techniques could be used to efficiently guide the mapping process. Furthermore, once a candidate ectopic pacemaker has been identified, we suggest a simple test to help determine whether or not the candidate corresponds to the real ectopic pacemaker. While the results from our simulations are encouraging, the utility of our localization strategies has yet to be determined in a clinical setting.

6.5 Appendix

6.5.1 Hyperbolic Localization

Coordinates of intersecting hyperbolae

It is convenient to use a polar coordinate system to compute the intersection points of two hyperbolae. We choose one of the electrodes to be at the origin and label it e_1 (Fig. 6.7A). The $\theta = 0$ line is defined to be along the line joining e_1 to another electrode which is labeled e_2. The distance between e_1 and e_2 is known and is labeled $2c_1$. The third electrode e_3 is at a position $(r, \theta) = (2c_2, \phi)$ (Fig. 6.7A).

Since the circular activation front propagates radially, a measured activation delay between recording sites implies that the electrodes are different distances from the source. This difference in distance is given by the conduction velocity v multiplied by the measured activation delay between the electrodes. For example, if the activation delay between e_1 and e_2 is Δt_{12} then the differential distance from the source is $2a_1 = v\Delta t_{12}$. Similarly, for a delay of Δt_{13} between the activations of e_1 and e_3, the differential distance is $2a_2 = v\Delta t_{13}$.

The hyperbola is defined by the set of points that are an equal difference in distance from two focal points [15, 17]. In our case, the focal points of the two hyperbolae are the electrode pairs (e_1,e_2) and (e_1,e_3). Therefore, the two activa-

tion delays Δt_{12} and Δt_{13} define two hyperbolae given by:

$$r = \frac{c_1^2 - a_1^2}{c_1 \cos\theta + a_1}, \tag{6.5}$$

and

$$r = \frac{c_2^2 - a_2^2}{c_2 \cos(\theta - \phi) + a_2}, \tag{6.6}$$

with focal points corresponding to the above electrode pairs respectively.

The intersection point (r^*, θ^*) of these hyperbolae gives the coordinates of the ectopic pacemaker. Therefore, from equations (6.5) and (6.6):

$$\frac{c_1^2 - a_1^2}{c_1 \cos\theta^* + a_1} = \frac{c_2^2 - a_2^2}{c_2 \cos(\theta^* - \phi) + a_2}$$

at the intersection point. After some algebra, we obtain:

$$(\alpha^2 + \beta^2)\cos^2\theta^* - 2\alpha\gamma\cos\theta^* + (\gamma^2 - \beta^2) = 0, \tag{6.7}$$

where

$$\begin{aligned} \alpha &= \frac{c_1}{c_1^2 - a_1^2} - \frac{c_2\cos\phi}{c_2^2 - a_2^2}, \\ \beta &= \frac{c_2\sin\phi}{c_2^2 - a_2^2}, \\ \gamma &= \frac{a_2}{c_2^2 - a_2^2} - \frac{a_1}{c_1^2 - a_1^2}. \end{aligned} \tag{6.8}$$

Equation (6.7) can be solved for $\cos\theta^*$ by the quadratic formula:

$$\cos\theta^* = \frac{\alpha\gamma}{\alpha^2 + \beta^2} \pm \frac{\beta}{\alpha^2 + \beta^2}\sqrt{\alpha^2 + \beta^2 - \gamma^2}, \tag{6.9}$$

and from equation (6.5), r^* is given by:

$$r^* = \frac{c_1^2 - a_1^2}{c_1\cos\theta^* + a_1}. \tag{6.10}$$

The number of intersection points is determined by the number of real, positive values of r^* determined by the two values of $\cos\theta^*$ corresponding to the $\pm$ sign. Hence, there may be zero, one or two intersection points.

Since $\cos\theta = \cos(2\pi - \theta)$, equation (6.9) does not completely determine θ^*. However, the value of Δt_{13} resolves the ambiguity since the distance to e_3 is only consistent with one of the values for θ^*.

Sensitivity analysis of hyperbolic localization

The precision of the hyperbolic localization strategy depends on the positioning of the catheter, the orientation and arrangement of the electrodes, and the measurement uncertainties. The catheter determines both the interelectrode spacing (corresponding to c_1 and c_2) and the electrode arrangement (corresponding to ϕ). The conduction velocity v and the electrode activation delays Δt_{12} and Δt_{13} are the measurements with the largest uncertainties and they combine to give the parameters a_1 and a_2.

An uncertainty in the parameter a results in an uncertainty in the opening angle ω of the hyperbola (Fig. 6.7B). The opening angle is determined by the hyperbola's eccentricity $\epsilon = c/a$ such that:

$$\tan\omega = \sqrt{\epsilon^2 - 1}, \tag{6.11}$$

where $\epsilon > 1$. The sensitivity of the opening angle to variations in the parameter a is given by:

$$\frac{d\omega}{da} = -(c^2 - a^2)^{-\frac{1}{2}}.$$

Therefore, the uncertainty in the opening angle is

$$\delta\omega = -(c^2 - a^2)^{-\frac{1}{2}}\delta a, \tag{6.12}$$

to first order in δa. This means that the uncertainty of the opening angle is minimized when the electrode spacing is large and the electrodes are oriented such that there is a small time difference between their activation.

Uncertainties in the opening angles $\delta\omega_1$ and $\delta\omega_2$ result in an uncertainty in the predicted location of the ectopic focus. This uncertainty can be determined by finding out how far the hyperbolic intersection point moves when the opening angles ω_1 and ω_2 are varied. For small variations of the opening angles, the intersection point moves by an amount D which has the following dependency:

$$D^2 \sim \left[\delta\omega_1{}^2 + \delta\omega_2{}^2 - 2\delta\omega_1\delta\omega_2 \cos\psi\right] \csc^2\psi, \tag{6.13}$$

where ψ is the intersection angle between the hyperbolae which can be approximated by the angle of intersection between the lines that are asymptotic to the hyperbolae:

$$\psi \approx \frac{1}{2}(\omega_1 - \omega_2) + \phi. \tag{6.14}$$

D^2 is minimized when $\psi = 90°$ and the uncertainties in the opening angles are small. Therefore, the optimal electrode arrangement is such that the electrodes are widely separated at right angles to each other and oriented so that they are activated simultaneously.

6.5.2 Localization by resetting

Coordinates of intersecting circles

If the resetting protocol is performed by stimulating at electrode e_1 then the distance r_1 between e_1 and the pacemaker can be estimated as discussed above. Therefore, the pacemaker must lie on the circle:

$$x^2 + y^2 = r_1^2,$$

where we have taken the origin of cartesian coordinates to be at e_1.

Given an estimate of the conduction velocity v, the activation delays Δt_{12} and Δt_{13} determine how much farther e_2 and e_3 are from the pacemaker relative to e_1:

$$\begin{aligned} r_2 &= r_1 + v\Delta t_{12}, \\ r_3 &= r_1 + v\Delta t_{13}, \end{aligned} \tag{6.15}$$

and the pacemaker lies at the intersection of the three circles:

$$\begin{aligned} x^2 + y^2 &= r_1^2, \\ (x - x_2)^2 + (y - y_2)^2 &= r_2^2, \\ (x - x_3)^2 + (y - y_3)^2 &= r_3^2, \end{aligned} \tag{6.16}$$

where e_2 and e_3 are at coordinates (x_2, y_2) and (x_3, y_3) respectively.

For simplicity, we orient the axes of the coordinate system so that $y_2 = 0$. Therefore, by solving (6.16) we obtain the coordinates of the intersection point (x^*, y^*):

$$x^* = \frac{r_1^2 - r_2^2 + x_2^2}{2x_2}, \tag{6.17}$$

$$y^* = \pm\sqrt{r_1^2 - \left(\frac{r_1^2 - r_2^2 + x_2^2}{2x_2}\right)^2} = y_3 \pm \sqrt{r_3^2 - \left(\frac{r_1^2 - r_2^2 + x_2^2}{2x_2} - x_3\right)^2},$$

where the two expressions for y^* allow us to resolve the ambiguity introduced by the $\pm$ signs.

Coordinates of intersection between a circle and a hyperbola

¿From the previous section, if stimuli are delivered at e_1 then the pacemaker must lie on a circle of radius r_1 centered at e_1. By measuring the activation delay to e_2 we can determine that the pacemaker lies on a hyperbola given by equation

(6.5). Substituting $r^* = r_1$ into equation (6.5) we get:

$$\cos\theta^* = \frac{c_1^2 - a_1^2}{c_1 r_1} - \frac{a_1}{c_1}, \tag{6.18}$$

where we have returned to the polar coordinate system depicted in Figure 6.6. The ambiguity between θ^* and its complement can be resolved by measuring the activation delay to a third electrode e_3, since its distance r_3 is only consistent with one of the values for θ^*.

Sensitivity analysis of localization by resetting

The precision of the resetting strategy is determined by the orientation of the electrodes in addition to uncertainties of the conduction time, propagation velocity, and electrode activation delays. Since the pacemaker location is identified with an intersection point between a circle and a hyperbola, the uncertainty in the predicted location is determined by finding out how far the intersection point moves when the opening angle of the hyperbola and the radius of the circle are varied.

If r_1 is the predicted distance to the pacemaker, then the uncertainty of r_1 is given by:

$$\delta r_1 = v(\delta \mathrm{CT}) + \mathrm{CT}(\delta v),$$

where v is the propagation velocity, CT is the conduction time, and δv and δCT are the respective uncertainties. The uncertainty in the opening angle of the hyperbola $\delta\omega$ is given by equation (6.12) above. If the circle's radius and the hyperbola's opening angle are varied by δr_1 and $\delta\omega$ respectively, then the intersection point moves by an amount D given by:

$$D^2 = (\delta r_1)^2 + 2(1 - \cos\delta\omega)(r_1^2 + r_1\delta r_1) \tag{6.19}$$

Therefore, the uncertainty of the predicted pacemaker location is minimized for a small $\delta\omega$. This means that the optimal electrode arrangement is such that the electrode spacing is large and the activation delays are small.

BIBLIOGRAPHY

[1] M. E. Josephson, *Clinical Cardiac Electrophysiology: Techniques and Interpretation* (Lea Febiger, Philadelphia, 1993), 2nd ed.

[2] D. W. Zhu, J. D. Maloney, T. W. Simmons, et al., J. Am. Coll. Cardiol. **26**, 843-849 (1995).

[3] J. F. Keane, WH Plauth, and A. S. Nadas, Am. Heart J. **84**, 748-753 (1972).

[4] P. C. Gillette, T. H. Goh, A. Garson Jr, et al., JAMA **253**, 391-392 (1985).

[5] J. A. Chiladakis, V. P. Vassilikos, T. N. Maounis, et al., PACE **20**, 953-959 (1997).

[6] J. Kalman, P. Sparks, J. Vohra, et al., PACE (Abstract) **21**, 902 (1998).

[7] P. Jais, M. Haissaguerre, D. C. Shah, et al., Circulation **95**, 562-564 (1997).

[8] M. Haissaguerre, F. I. Marcus, B. Fischer, et al., J. Cardiovasc. Electrophysiol. **5**, 743-751 (1994).

[9] P. C. Gillette and A. Garson, Circulation **56**, 571-575 (1977).

[10] M. D. Lesh, G..F. Van Hare, L. M. Epstein, et al., Circulation **89**, 1074-1089 (1994).

[11] M. D. Lesh, J. M. Kalman, and J. E. Olgin, J. Cardiovasc. Electrophysiol. **7**, 368-381 (1996).

[12] C. M. Tracy, J. F. Swartz, R. D. Fletcher, et al., J. Am. Coll. Cardiol. **21**, 910-917 (1993).

[13] E. P. Walsh, J. P. Saul, J. E. Hulse, et al., Circulation **86**, 1138-1146 (1992).

[14] H. Poty, N. Saoudi, M. Haissaguerre, et al., Am. Heart J. **131**, 481-489 (1996).

[15] G. Hartcup, *The War of Invention: Scientific Developments, 1914-18.* (Brassey Defence Publishers, London, 1988) 68-76.

[16] B. Rawling, *Surviving Trench Warfare: Technology and the Canadian Corps, 1914-1918.* (University of Toronto Press, Toronto, 1992) 93-94.

[17] D. Zwillinger, *Standard mathematical tables and formulae:* 30^{th} *edition.* (CRC Press, Boca Raton, 1996) p. 286.

[18] H. C. Strauss, A. L. Saroff, J. T. Bigger Jr, et al., Circulation **47**, 86-93 (1973).

[19] D. G. Benditt, S. Milsein, M. Goldstein, et al., *Cardiac Electrophysiology: From Cell to Bedside.* (W. B. Saunders Company, Philadelphia, 1990) p. 721, eds. D. P. Zipes and J. Jalife..

[20] M. M. Scheinman, D. Basu, and M. Hollenberg, Circulation **50**, 266-273 (1974).

[21] A. Mehdirad, J. Gaiser, P. Baker, et al., PACE **21**, 316-321 (1998).

[22] M. E. Josephson, H. L. Waxman, M. E. Cain, et al., Am. J. Cardiol. **50**, 11-22 (1982).

[23] L. M. Gepstein, G. Hayam, and S. A. Ben-Haaim, Circulation **95**, 1611-1622 (1997).

[24] H. Kottkamp, G. Hindricks, G. Breithardt, et al., J. Cardiovasc. Electrophysiol. **8**, 1332-1337 (1997).

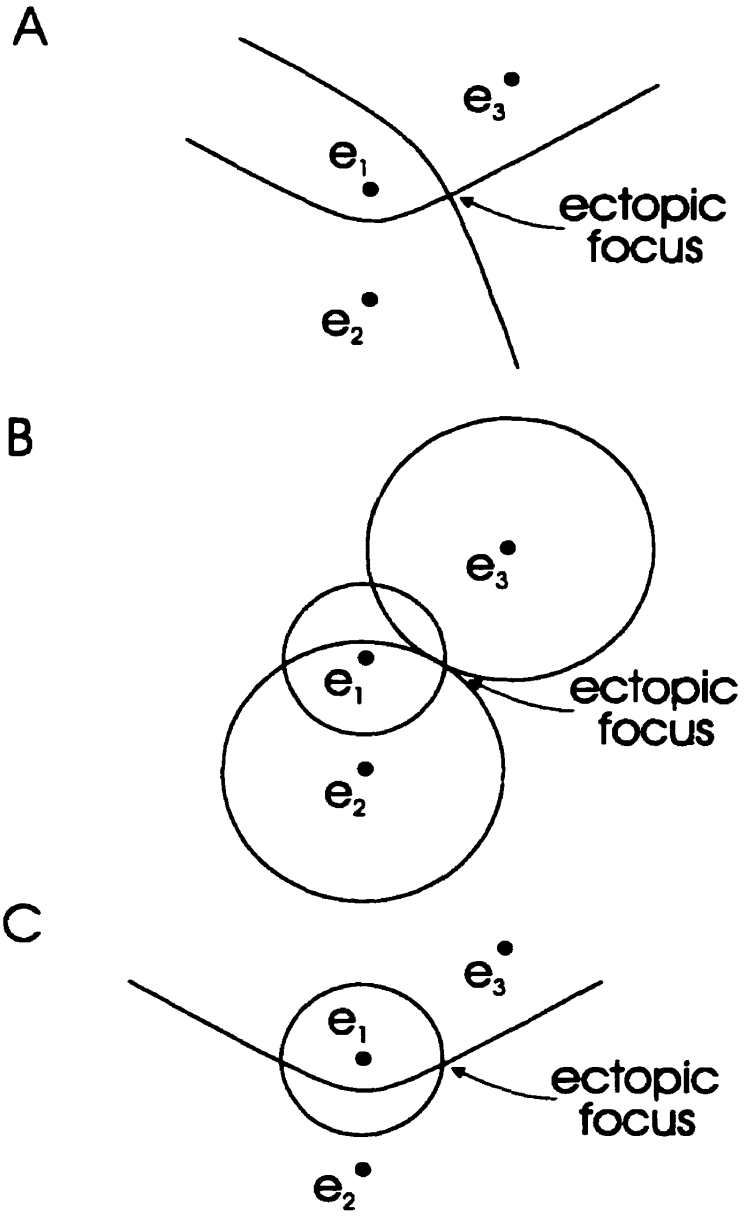

Figure 6.1: a) Hyperbolic localization. An activation delay between a pair of intracardiac electrodes (e_1, e_2, e_3) defines a hyperbola upon which the ectopic focus lies. Therefore, two electrode pairs define two hyperbolae and the pacemaker is located at their intersection. b) & c) Localization by resetting. Resetting stimuli are given at electrode e_1 and the pacemaker's response is used to estimate the electrode-pacemaker distance. This distance defines a circle centered on the stimulation electrode and the pacemaker lies on this circle. By measuring the activation delays to the other electrodes, the various electrode-pacemaker distances can be determined and the pacemaker can be located by computing either b) the intersection of three circles centered about each of the electrodes with radii equal to their respective electrode-pacemaker distances, or c) the intersection of the circle about the stimulation electrode and a hyperbola.

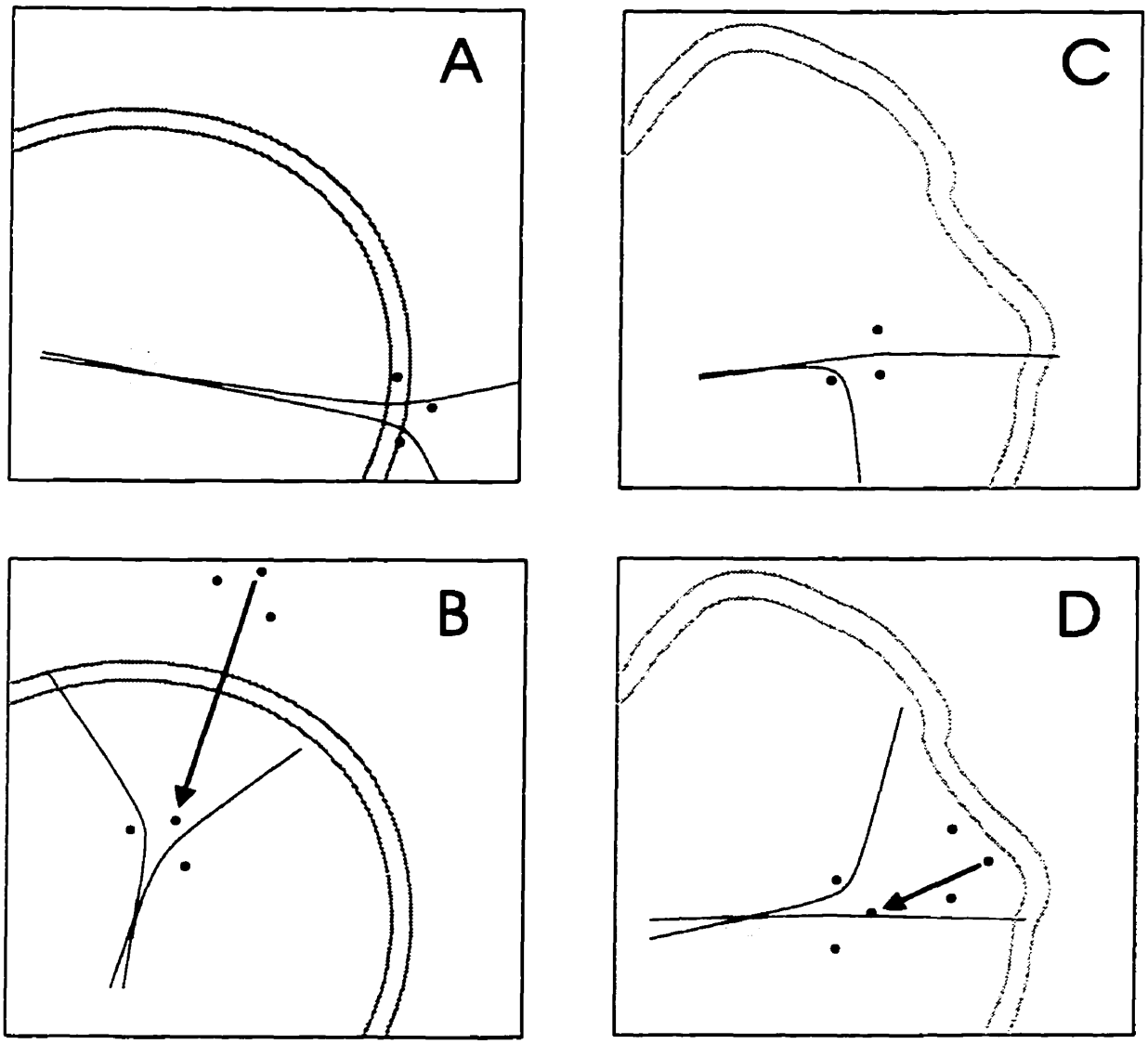

Figure 6.2: Hyperbolic localization in homogeneous isotropic (left column) and heterogeneous anisotropic (right column) media. The large concentric curves are the contour lines of zero voltage. The hyperbolae are the solid black curves whose intersection corresponds to the predicted pacemaker location. a) Trial 3 in a homogeneous sheet where the hyperbolae intersected within the 3mm target radius of the pacemaker (gray circle). b) In trial 4, the first iterate gave a predicted location outside the target. For the next iterate, the catheter was moved so that the latest activated electrode was positioned at the predicted pacemaker location (arrow). The next iterate gave hyperbolae that intersected within the target. c) Trial 2 in an inhomogeneous sheet where the target was hit on the first iterate. d) Trial 9 showing convergence after two

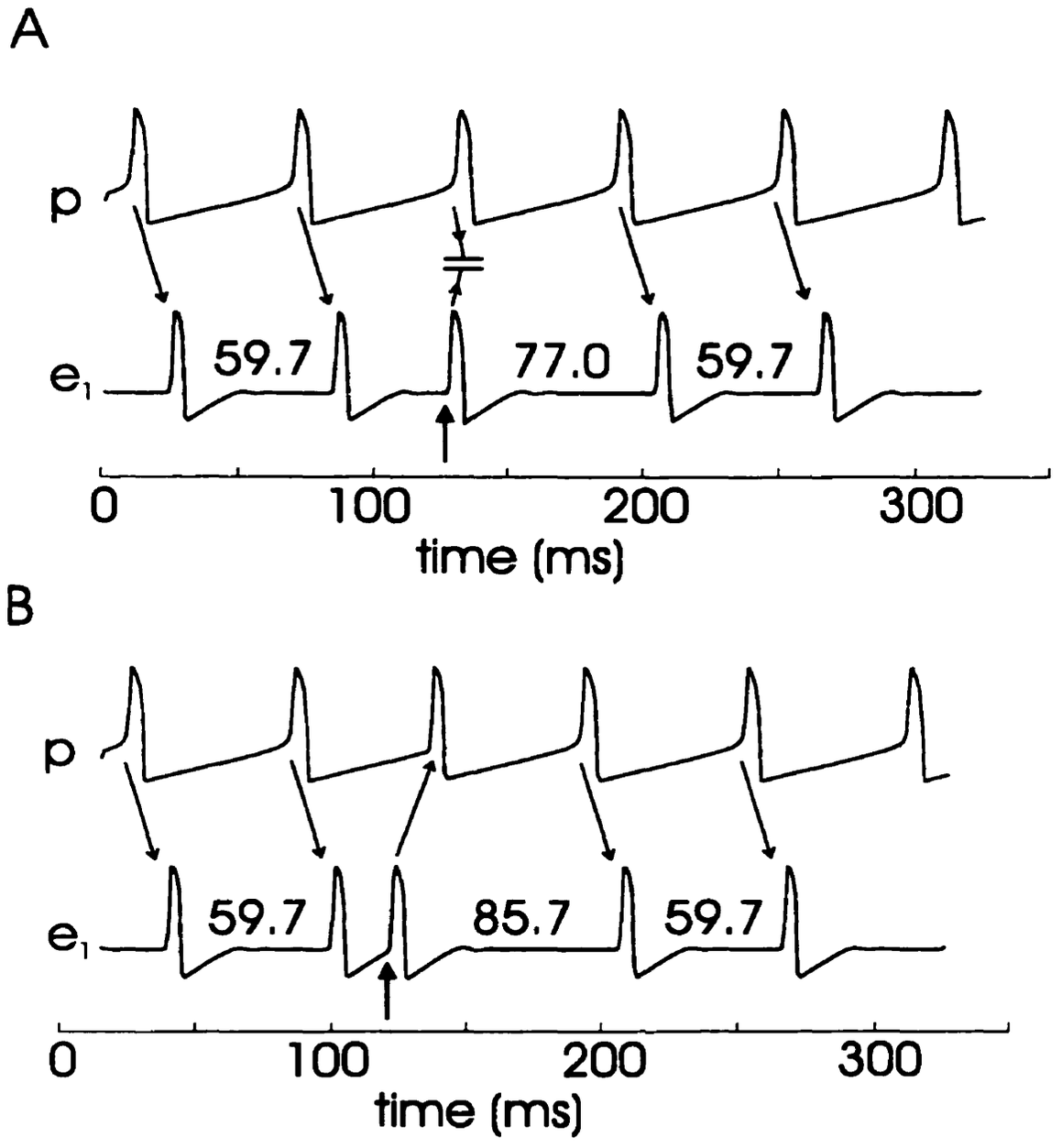

Figure 6.3: a) A stimulus (arrow) given in the interference zone for trial 1 of resetting in a homogeneous isotropic sheet. When the normalized coupling interval of the stimulus was longer than 0.52 the wave generated by the stimulus collided with an outgoing wave generated by the pacemaker and had no effect on the subsequent rhythm. Here, the normalized coupling interval was 0.7. b) A resetting stimulus given at a normalized coupling interval of 0.36 propagated into the pacemaker region and reset the rhythm.

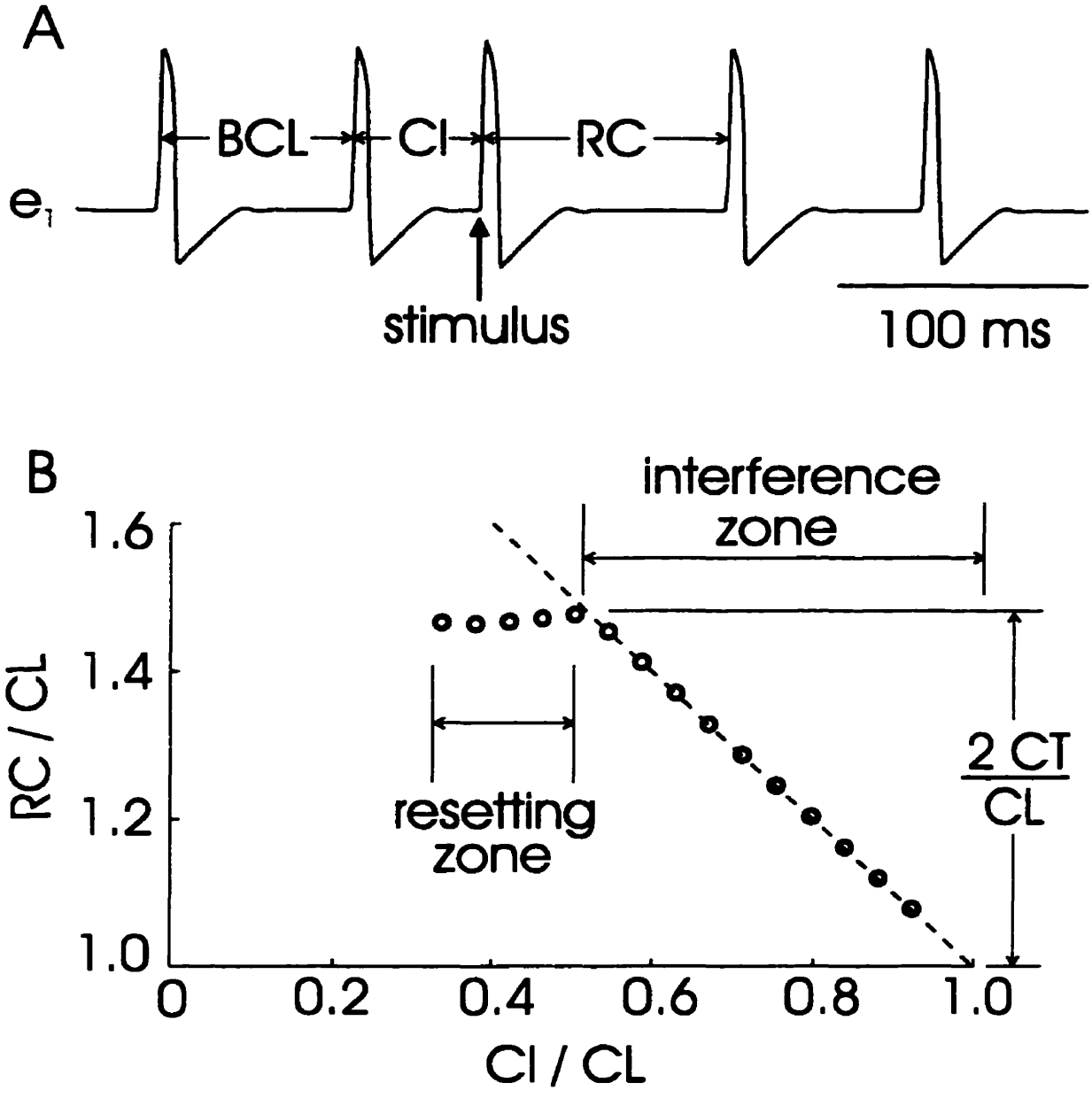

Figure 6.4: a) Measurement of resetting for trial 1 in a homogeneous isotropic sheet. Stimuli given at various coupling intervals (CI) resulted in different degrees of resetting, quantified by measuring the return cycle (RC) as a function of CI. Normalizing for the cycle length (CL) allows for the comparison of different rhythms. b) The normalized resetting curve shows that stimuli given in the interference zone yielded points that fall on the dashed compensatory line, whereas resetting stimuli gave a flat part of the curve.

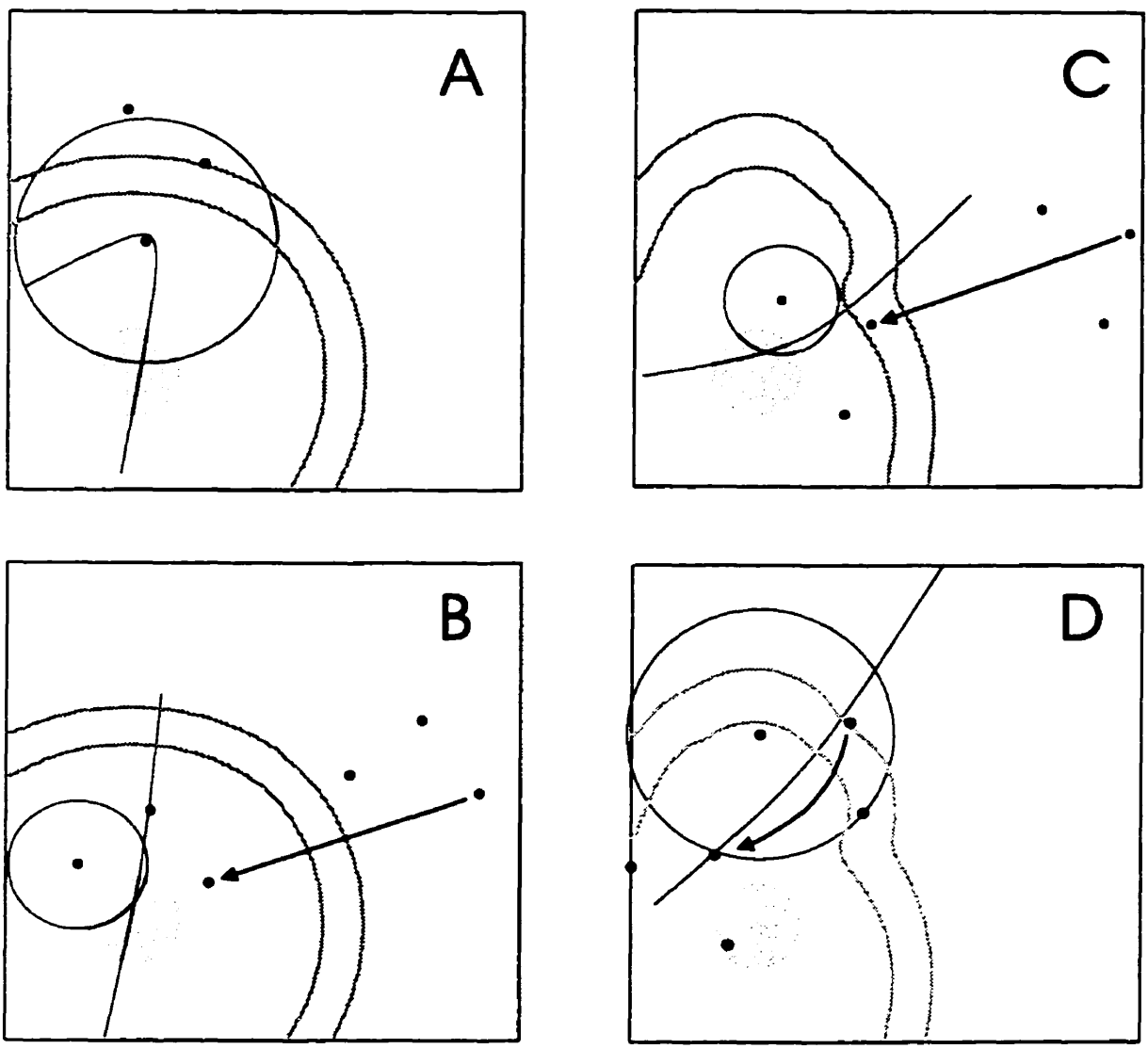

Figure 6.5: Localization by resetting in homogeneous isotropic (left column) and heterogeneous anisotropic (right column) media. a) Trial 1 in a homogeneous sheet where the pacemaker target (gray circle) was hit after one iterate. b) Trial 4 required two iterates to locate the pacemaker. c) Trial 1 converged after 2 iterates in an inhomogeneous anisotropic sheet. d) After the first iterate of trial 3, the catheter was moved so that the latest activated electrode was at the predicted pacemaker location (arrow). As a result, one of the other electrodes fell in the target region.

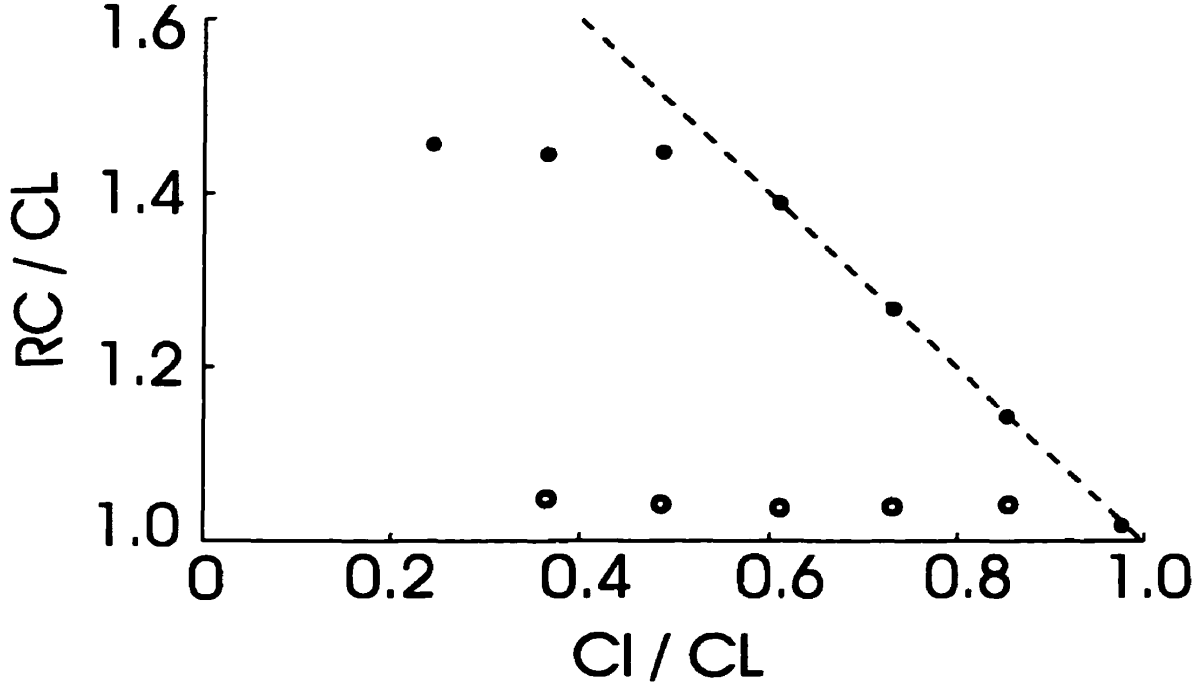

Figure 6.6: Confirmation strategy. Stimuli were applied to the earliest activated electrode in trial 2 of hyperbolic localization in an inhomogeneous anisotropic sheet (Fig. 2c). The resulting resetting curve (•) had a large interference zone, thereby ruling out the stimulus location as a possible pacemaker site. Stimuli applied to the predicted pacemaker location (hyperbolic intersection point in Fig. 2c) gave a resetting curve (o) with no interference zone, thereby confirming the correct pacemaker location.

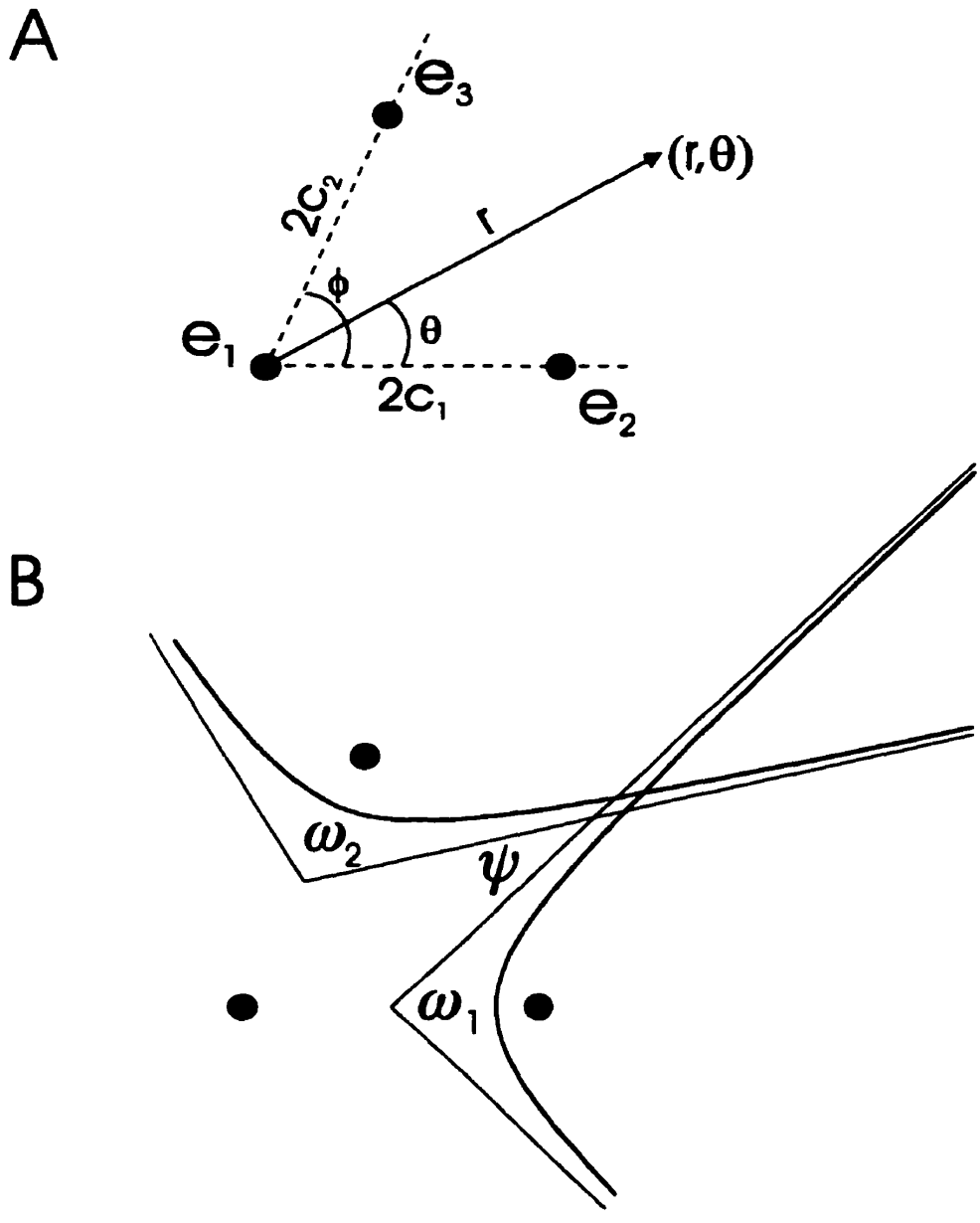

Figure 6.7: a) Polar coordinate system and relative positions of the electrodes. b) Geometry of intersecting hyperbolae.

CHAPTER 7

CONCLUSION

In this thesis, I have described several aspects of cardiac control. The first part of the thesis delt with characterizing the dynamics of an abnormal heart rhythm and using feedback control to suppress the arrhythmia. The second part of the thesis delt with diagnosis of an arrhythmia mechanism and developing methods to assist in the surgical control of arrhythmias caused by ectopic foci.

7.1 Dynamic Cardiac Control

The abnormal rhythm that was controlled in our experiments involved an alternating AV nodal conduction time. The alternation was caused by a period-doubling bifurcation consistent with a simple finite difference equation model of AV nodal recovery and facilitation properties, although the slow drift of the system due to fatigue remains poorly understood.

AV nodal alternans are not dangerous, but cardiac alternans occurring in other areas of the heart are a harbinger of sudden death. If the dangerous alternans are also caused by a period-doubling bifurcation, then a control algorithm similar to ours could suppress the alternans and possibly prevent serious illness.

The dynamic control experiments presented in Chapter 3 were the first example of biological control that tracked the evolution of a drifting fixed point. However, the degree to which tracking could be maintained was limited by the fixed feedback gain parameter. In Chapter 4, I presented a new control algorithm that adapts the feedback gain parameter based on the dynamics of the control perturbations. This algorithm may be especially useful for the control of nonstationary biological systems since it requires little information about the system other than the correct direction in which to apply the perturbations.

Using feedback algorithms to direct the timing of electrical stimuli is a promising approach to the control of abnormal heart rhythms. However, the techniques

based on feedback control of low-dimensional dynamics have yet to be used in a clinical situation or an *in vivo* experiment.

7.2 Diagnosis of Arrhythmia Mechanisms

The first step in the control of any cardiac arrhythmia is the accurate diagnosis of the arrhythmia mechanism. In Chapter 5, I described a procedure to distinguish a spiral wave pattern from a target pattern by delivering resetting stimuli and measuring activity at two electrode locations. Targets and spirals correspond to different arrhythmia mechanisms that are sometimes difficult to distinguish using standard clinical electrophysiological testing. Our technique exploits the different spatio-temporal symmetry properties of targets and spirals. Because our technique requires only standard intracardiac stimulation and recording procedures, our diagnostic method could easily be incorporated in a typical cardiac electrophysiology clinic.

7.3 Locating Sources of Abnormal Cardiac Electrical Activity

In Chapter 6, I presented two new methods to locate regions of abnormal pacemaker activity. The techniques were based on the geometry of wave propagation in an excitable medium like the heart.

Unlike the diagnostic method of Chapter 5, the localization procedures require new medical devices to help orient the intracardiac electrodes as well as compute their relative positions and activation delays. The predicted location of the ectopic focus must be computed on-line and a catheter must somehow be guided to that spot. Fortunately, new technology is currently being developed that will facilitate these requirements.

Nevertheless, the confirmation strategy presented in Chapter 6 requires no new technology and could be implemented immediately. All that is required is an

appropriately timed electrical stimulus in order to ensure that the stimulation electrode is at the correct location for ablation. The confirmation strategy is based on the properties of resetting curves when the stimuli are delivered away from the source of the rhythm.

7.4 Future Work

The material presented in this thesis suggests that methods from nonlinear dynamics and geometry can help control of abnormal heart rhythms. But much work remains to be done.

Dynamic control of cardiac arrhythmias should begin with an understanding of the dynamics of the abnormal rhythm. In our case, the AV nodal dynamics were well approximated by a slowly drifting one-dimensional map. But the nature of the drift is not well understood. New stimulation protocols that exploit the short-term dynamics of the AV node should be developed in order to rapidly assess AV nodal recovery and facilitation so that the evolution of these properties can be measured over the course of the drift.

The restricted control algorithm used in Chapter 3 and analysed in Chapter 4 should be studied in higher dimensional systems since it is likely that some cardiac arrhythmias are not described by one-dimensional maps. In particular, it would be interesting to know if the stability zones are also extended in higher dimensional systems when compared with unrestricted control. Also, does the adaptive algorithm extend to higher dimensions?

The phase resetting curves in Chapters 5 and 6 suggest that the dynamics of reentrant arrhythmias and ectopic pacemakers may also be described by one-dimensional maps. It would be interesting to study whether or not feedback control techniques could direct the timing of electrical stimuli in order to eliminate these arrhythmias.

Although the localization and confirmation procedures of Chapter 6 were developed for ectopic pacemakers, they could also be used to localize microreentrant

circuits or narrow reentrant pathways through damaged heart tissue. The localization methods should direct electrodes towards all point-like sources of electrical activity. These hypotheses should be tested in future numerical simulations and experiments since there are significant clinical implications for locating and confirming ablation sites to eliminate reentry.

APPENDIX A

The following C++ source code was used in the resetting simulations for Chapter 5 and Chapter 6:

```
/* Resetting of a reentrant spiral around an obstacle */

#include <stdio.h>
#include <stdlib.h>
#include <fstream.h>
#include <iostream.h>
#include <math.h>

#define ROW 80
#define COL 80     /* number of elements */
#define H 0.04     /* grid spacing (cm) */
#define K 0.05     /* time step size (msec)*/
#define D1 0.001   /* diffusion coefficient (cm^2/msec) in region 1*/
#define D2 0.001   /* diffusion coefficient (cm^2/msec) in region 2*/
#define Ic1 0.     /* constant current in region 1*/
#define Ic2 -5.0   /* constant current in region 2*/
#define W1_h 0.6   /* sigmoidal max amplitude in region 1 */
#define W1_l 0.4   /* sigmoidal min amplitude in region 1 */
#define W2_h 0.6   /* sigmoidal max amplitude in region 2 */
#define W2_l 0.4   /* sigmoidal min amplitude in region 2 */

#define Obst 40    /* obstacle center */
#define CN2 8      /* radius of CN2 are coupled with D2 and Ic2*/
#define Rstim 20   /* row position for stimulus */
#define Cstim 40   /* column position of stimulus */
#define Ssize 2    /* physical size of stimulus region */
#define Rmeas1 20 /* positions for measurments */
#define Cmeas1 40
#define Rmeas2 40
#define Cmeas2 15
#define Rmeas3 60
#define Cmeas3 60
#define Vthresh 0.0  /* threshold voltage for phase 0 */
#define nlearn 2     /* number of beats before stim */
#define nbtwn 7      /* number of beats for each resetting trial*/
#define maxdel 50000 /* maximum delay before restarting */
#define prestep 10   /* stepsize of coupling interval  */
#define strtpre 950  /* starting coupling interval  */
#define Iapp 1.0     /* applied current during stim */
#define Idur 20      /* duration of stim */
#define APDmin 40    /* minimum duration of action potential */

double v[2][ROW+2][COL+2]; /* array of variables in the grid */
double w[2][ROW+2][COL+2];
```

```
double vini[ROW+2][COL];  /* initial condition array */
double wini[ROW+2][COL];

int nstim = (strtpre / prestep) -1; /* number of stimuli */

double D = 0.0;     /* diffusion coefficient */
double Ic = 0.0;    /* constant current */
double W = 0.0;     /* amplitude of restitution in FHN */
double ct = 0.0;    /* conduction time between stim & meas */
double clm1 = 0.0; /* measured cycle lengths */
double clm2 = 0.0;
double clm3 = 0.0;

double vm1m0 = 0.0; /* current value of v at CNmeas1 */
double vm1m1 = 0.0; /* value of v at CNmeas1 at last time step */
double vm2m0 = 0.0;
double vm2m1 = 0.0;
double vm3m0 = 0.0;
double vm3m1 = 0.0;

double pottactm1 = 0.0; /* activation time if apd > APDmin */
double pottactm2 = 0.0;
double pottactm3 = 0.0;

double tactm1m0 = 0.0;  /* activation time at CNmeas1 */
double tactm1m1 = 0.0;  /* previous activation time at CNmeas1 */
double tactm2m0 = 0.0;
double tactm2m1 = 0.0;
double tactm3m0 = 0.0;
double tactm3m1 = 0.0;

double toffm1 = 0.0;     /* end of action potential at CNmeas1 */
double toffm2 = 0.0;
double toffm3 = 0.0;
double apdm1 = 0.0;      /* apd at meas1 */
double apdm2 = 0.0;
double apdm3 = 0.0;
int dm1count = 0; /* delay after activation at CNmeas1 */
int dm2count = 0;
int dm3count = 0;
int dscount = 0;         /* delay after activation at CNstim */
int ncount = 0;          /* action potential counter */
int dur = 0;             /* stimulus duration counter */

double clm1m0 = 0.0;     /* cycle length for this beat measured at
CNmeas1 */
double clm1m1 = 0.0;     /* cycle length for the previous beat */
double clm2m0 = 0.0;
double clm2m1 = 0.0;
double clm3m0 = 0.0;
double clm3m1 = 0.0;
double Del = strtpre;     /* stim delay time from CNmeas activation */
double Tm1 = 0;           /* activation times after stimulus */
double Tm2 = 0;
```

```
double Tm3 = 0;
double I = 0;            /* applied current */

double phase1 = 0;       /* phase of stimulus */
double phase2 = 0;
double phase3 = 0;

/* function declarations */

double f(double, double);
double g(double, double);


main () {
   /* connect input stream to files vinit.dat and winit.dat */

   ifstream vin ("vinit.dat");
   ifstream win ("winit.dat");

   if (!vin) cout << "error opening v input file" << endl;
   if (!win) cout << "error opening w input file" << endl;

   /* connect output streams to .dat files */

   ofstream ofile1 ("prc1.dat");    /* prc at CNmeas1 */
   ofstream ofile2 ("prc2.dat");
   ofstream ofile3 ("prc3.dat");
   ofstream ofile4 ("explog.dat");  /* log of the simulation */

   if (!ofile1) cout << "error opening prc1 output file" << endl;
   if (!ofile2) cout << "error opening prc2 output file" << endl;
   if (!ofile3) cout << "error opening prc3 output file" << endl;
   if (!ofile4) cout << "error opening explog output file" << endl;

   int old = 1;
   int neww = 0;

   /* read initial conditions */

   int i,j;
   for (i = 1; i<= ROW; i++){
      for (j = 1; j <= COL; j++) {
         vin >> vini[i][j];
         win >> wini[i][j];
         v[neww][i][j] = vini[i][j];
         w[neww][i][j] = wini[i][j];
       }
    }
```

```
/* no flux boundary conditions */

for (i=1;i<=ROW;i++){
   v[neww][i][0] = v[neww][i][1];
   v[neww][i][COL+1] = v[neww][i][COL];
}
for (i=1;i<=COL;i++){
   v[neww][0][i] = v[neww][1][i];
   v[neww][ROW+1][i] = v[neww][ROW][i];
}

/* start integrating equations */

int time = 0;
int k = 1;
int trial = k;

while (k <= nstim ) {      /* continue until finished protocol
   time++;
   if (dur > 0) dur++;
   int n = old;
   old = neww;
   neww = n;

   int i,j;
   for (i = 1; i <= ROW; i++) { /* cell loop */
      for (j = 1; j <= COL; j++) {

   /* record time of potential activation at CNmeas, c1, ct, */
   /* and compute the stimulation delay time Del */

      if (i == Rmeas1 && j == Cmeas1 && vm1m0 >= Vthresh &&
                  vm1m1 < Vthresh) {
         ncount++;
         dm1count = 0;
         pottactm1 = (Vthresh - vm1m1)/(vm1m0 - vm1m1) + time - 1;
         tactm1m1 = tactm1m0;
         tactm1m0 = pottactm1;
         c1m1 = tactm1m0 - tactm1m1;
         Tm1 += c1m1;
         c1m1m1 = c1m1m0;
         c1m1m0 = c1m1;
         ofile4 << "activation time at e1 = " << tactm1m0 << endl;
       }
```

```
if (i == Rmeas2 && j == Cmeas2 && vm2m0 >= Vthresh &&
            vm2m1 < Vthresh) {
  dm2count = 0;
  pottactm2 = (Vthresh - vm2m1)/(vm2m0 - vm2m1) + time - 1;
  tactm2m1 = tactm2m0;
  tactm2m0 = pottactm2;
  clm2 = tactm2m0 - tactm2m1;
  Tm2 += clm2;
  clm2m1 = clm2m0;
  clm2m0 = clm2;
  ofile4 << "activation time at e2 = " << tactm2m0 << endl;
}

if (i == Rmeas3 && j == Cmeas3 && vm3m0 >= Vthresh &&
            vm3m1 < Vthresh) {
  dm3count = 0;
  pottactm3 = (Vthresh - vm3m1)/(vm3m0 - vm3m1) + time - 1;
  tactm3m1 = tactm3m0;
  tactm3m0 = pottactm3;
  clm3 = tactm3m0 - tactm3m1;
  Tm3 += clm3;
  clm3m1 = clm3m0;
  clm3m0 = clm3;
  ofile4 << "activation time at e3 = " << tactm3m0 << endl;
}

/* increment duration above Vthresh */

if (i == Rmeas1 && j == Cmeas1 && vm1m0 >= Vthresh)
       dm1count++;
if (i == Rmeas2 && j == Cmeas2 && vm2m0 >= Vthresh)
       dm2count++;
if (i == Rmeas3 && j == Cmeas3 && vm3m0 >= Vthresh)
       dm3count++;

/* if the incursion above Vthresh was not an AP */
/* then make the necessary corrections */

if (i == Rmeas1 && j == Cmeas1 && vm1m0 <= Vthresh &&
            vm1m1 > Vthresh && dm1count < APDmin) {
  if (ncount != 0) ncount--;
  dm1count = 0;
  tactm1m0 = tactm1m1;
  Tm1 -= clm1;
}

if (i == Rmeas2 && j == Cmeas2 && vm2m0 <= Vthresh &&
            vm2m1 > Vthresh && dm2count < APDmin) {
  dm2count = 0;
  tactm2m0 = tactm2m1;
  Tm2 -= clm2;
}
```

```
if (i == Rmeas3 && j == Cmeas3 && vm3m0 <= Vthresh &&
          vm3m1 > Vthresh && dm3count < APDmin) {
  dm3count = 0;
  tactm3m0 = tactm3m1;
  Tm3 -= clm3;
}

/* determine apd at CNmeas and write cl & apd to files */

if (i == Rmeas1 && j == Cmeas1 & vm1m0 <= Vthresh &&
          vm1m1 > Vthresh && dm1count >= APDmin) {
  toffm1 = (Vthresh - vm1m1)/ (vm1m0 - vm1m1) + time -1;
  apdm1 = toffm1 - tactm1m0;
  ofile4 << ncount << "  cl = " << clm1 << " Del = "
       << Del << "  apd = " << apdm1 << endl;
  if (ncount > nlearn) {
       ofile1 << phase1 << "       " << Tm1 << endl;
  }
}

if (i == Rmeas2 && j == Cmeas2 & vm2m0 <= Vthresh &&
          vm2m1 > Vthresh && dm2count >= APDmin) {
  toffm2 = (Vthresh - vm2m1)/ (vm2m0 - vm2m1) + time-1;
  apdm2 = toffm2 - tactm2m0;
  if (ncount > nlearn) {
    ofile2 << phase2 << "       " << Tm2 << endl;
  }
}

if (i == Rmeas3 && j == Cmeas3 & vm3m0 <= Vthresh &&
  vm3m1 > Vthresh && dm3count >= APDmin) {
  toffm3 = (Vthresh - vm3m1)/ (vm3m0 - vm3m1) + time -1;
  apdm3 = toffm3 - tactm3m0;
  if (ncount > nlearn) {
    ofile3 << phase3 << "       " << Tm3 << endl;
  }
}

/* continue incrementing delay counter */

if (i == Rmeas1 && j == Cmeas1 && vm1m0 < Vthresh &&
          dm1count > APDmin) dm1count++;
if (i == Rmeas2 && j == Cmeas2 && vm2m0 < Vthresh &&
          dm2count > APDmin) dm2count++;
if (i == Rmeas3 && j == Cmeas3 && vm3m0 < Vthresh &&
          dm3count > APDmin) dm3count++;
if (i == Rstim && j == Cstim && ncount >= nlearn)
          dscount++;
```

```
/* STIMULATION */

if (i == Rstim && j == Cstim && ncount == nlearn &&
        trial == k && dscount >= Del && dscount < Del +1){
  trial++;
  phase1 = dm1count;
  phase2 = dm2count;
  phase3 = dm3count;
  Tm1 = 0;
  Tm2 = 0;
  Tm3 = 0;
  dur = 1;
  Del = strtpre - k * prestep;
  ofile4 << "delay = " << dscount << endl;
  dscount = 0;
}

if (i >= Rstim - Ssize  && i <= Rstim + Ssize &&
    j >= Cstim - Ssize && j <= Cstim + Ssize && dur > 0) {
  if (dur < Idur) I = Iapp;
  else dur = 0;
}
else I = 0;

/* COMPUTE ARRAY FOR NEXT TIMESTEP */

if (ncount == nbtwn || dm1count >= maxdel) {
  ncount = 0;
  dm1count = 0;
  dm2count = 0;
  dm3count = 0;
  int rlim, clim;
  for (rlim = 1; rlim<= ROW; rlim++){
     for (clim = 1; clim <= COL; clim++) {
        v[neww][rlim][clim] = vini[rlim][clim];
        v[old][rlim][clim] = vini[rlim][clim];
        w[neww][rlim][clim] = wini[rlim][clim];
        w[old][rlim][clim] = wini[rlim][clim];
     }
   }
   ofile4 << "return to initial conditions" << endl;
   k++;
   dscount = 0;
   time = 0;
}
```

```
            /* integration step */

            v[neww][i][j] = v[old][i][j] +
                K * f(v[old][i][j], w[old][i][j]) + K*(I + Ic) +
                    K * D * (v[old][i][j+1] + v[old][i][j-1] -
                       2*v[old][i][j])/(H * H) +
                         K * D * (v[old][i+1][j] + v[old][i-1][j] -
                           2*v[old][i][j])/(H * H);

            w[neww][i][j] = w[old][i][j] + K * g(v[old][i][j],
                w[old][i][j])* W;


            /* set parameters for obstacle */

            if ((i-Obst)*(i-Obst)+(j-Obst)*(j-Obst) < CN2*CN2) {
              D = D2;
              Ic = Ic2;
              W = (W2_h - W2_l)/(1 + exp(-v[neww][i][j])) +W2_l;
            }

            else {
              D = D1;
              Ic = Ic1;
              W = (W1_h - W1_l)/(1 + exp(-v[neww][i][j])) +W1_l;
            }

            if (i == Rmeas1 && j == Cmeas1) {vm1m1 = vm1m0;
              vm1m0 = v[neww][i][j];}
            if (i == Rmeas2 && j == Cmeas2) {vm2m1 = vm2m0;
              vm2m0 = v[neww][i][j];}
            if (i == Rmeas3 && j == Cmeas3) {vm3m1 = vm3m0;
              vm3m0 = v[neww][i][j];}
          }
        }

        /* boundary conditions */

        for (i=1;i<=ROW;i++){
           v[neww][i][0] = v[neww][i][1];
           v[neww][i][COL+1] = v[neww][i][COL];
        }

        for (i=1;i<=COL;i++){
           v[neww][0][i] = v[neww][1][i];
           v[neww][ROW+1][i] = v[neww][ROW][i];
        }
      }
    }
```

```
/* define the 2 dimensional differential equation */

double f(double v, double w) {
  double eps = 0.3;
  return (v - v*v*v/3.0 - w)/eps;
}

double g(double v, double w) {
  double eps = 0.3;
  double beta = 0.7;
  double gamma = 0.5;
  return eps * (v + beta - gamma*w);
}
```

APPENDIX B

The following C++ source code was used to assign random inhomogeneous anisotropic diffusion coefficients for the simulations in Chapter 5 and Chapter 6:

```
#include <stdio.h>
#include <stdlib.h>
#include <fstream.h>
#include <iostream.h>
#include <math.h>


#define ROW 80
#define COL 80          /* number of grid points */

#define Diffx 0.001     /* average diffusion coefficient in x
direction */
#define Diffy 0.0015    /* average diffusion coefficient in y
direction */

#define Nisl 5          /* number of square islands */
#define ILS 30.0        /* average island size */

double ns = 0.001;

double nsilsz = 5.0;

double Dx[ROW+2][COL];
double Dy[ROW+2][COL];

double dxtemp = Diffx;
double dytemp = Diffy;

int islsz = 0;
int isllocx=0;
int isllocy=0;

int i = 0;
int j = 0;
int isln = 0;


main () {

        /* connect output streams to *.dat files */

        ofstream ofile1 ("diffx.dat");
        ofstream ofile2 ("diffy.dat");
```

```
        if (!ofile1) cout << "error opening vinit output file" <<
endl;
        if (!ofile2) cout << "error opening winit output file" <<
endl;

      for (i = 1; i<= ROW; i++){
        for (j = 1; j <= COL; j++) {
          Dx[i][j] = Diffx;
          Dy[i][j] = Diffy;
        }
      }

      for (isln = 1; isln <= Nisl; isln++){
            islsz = ILS + nsilsz * (drand48()- 0.5);
            isllocx = 70 * (drand48());
            isllocy = 70 * (drand48());
            dxtemp = Diffx + ns * (drand48() - 0.5);
            dytemp = Diffy + ns * (drand48() - 0.5);
            cout << "location = " << isllocx << ",  " << isllocy << ",
size = " << islsz
                 << ",  diffusion coeff's = " << dxtemp << ",  " <<
dytemp << endl;
            for (i = 1; i<= ROW; i++){
            for (j = 1; j <= COL; j++) {
              if (i >= isllocx && i <= isllocx + islsz
                  && j >= isllocy && j <= isllocy + islsz){
                  Dx[i][j] = dxtemp;
                    Dy[i][j] = dytemp;
              }
            }
            }
      }

      for (i = 1; i<= ROW; i++){
        for (j = 1; j <= COL; j++) {
          ofile1 << Dx[i][j];
          ofile2 << Dy[i][j];
        }
      }

}
```

APPENDIX C

The following Matlab source code performs the hyperbolic localization procedure from Chapter 6.

```
% This M-file uses hyperbolic localization to compute and plot
% the coordinates of an ectopic pacemaker.

clear;

pmkr = input('input the PACEMAKER location "[row col]":');

% input electrode positions

e1 = input('input coordinates of ELECTRODE e1 "[row col]": ');
e2 = input('input coordinates of ELECTRODE e2 "[row col]": ');
e3 = input('input coordinates of ELECTRODE e3 "[row col]": ');

% compute interelectrode distances

d12 = sqrt((e1(1,1)-e2(1,1))^2 + (e1(1,2) - e2(1,2))^2);
d13 = sqrt((e1(1,1)-e3(1,1))^2 + (e1(1,2) - e3(1,2))^2);
d23 = sqrt((e3(1,1)-e2(1,1))^2 + (e3(1,2) - e2(1,2))^2);

% input activation times and velocity estimate

t1 = input('input TIME of activation for e1: ');
t2 = input('input TIME of activation for e2: ');
t3 = input('input TIME of activation for e3: ');

v = input('input an estimate of the conduction VELOCITY: ');

fail = 0;

% deterimine the electrode arrangement

ecc_12 = d12/(v* abs(t1 - t2));
ecc_13 = d13/(v* abs(t1 - t3));
ecc_23 = d23/(v* abs(t2 - t3));

[ecc, orderecc] = sort([ecc_12 ecc_13 ecc_23]);

if (orderecc(1) == 3)
      e_a = e1; t_a = t1;
      e_b = e2; t_b = t2;
      e_c = e3; t_c = t3;
      d_ab = d12; d_ac = d13; d_bc = d23;
elseif (orderecc(1) == 2)
      e_a = e2; t_a = t2;
```

```
      e_b = e1; t_b = t1;
      e_c = e3; t_c = t3;
      d_ab = d12; d_ac = d23; d_bc = d13;
elseif (orderecc(1) == 1)
      e_a = e3; t_a = t3;
      e_b = e1; t_b = t1;
      e_c = e2; t_c = t2;
      d_ab = d13; d_ac = d23; d_bc = d12;
end

% determine the hyperbola parameters

      c1 = 0.5*sqrt((e_a(1,1)-e_b(1,1))^2 + (e_a(1,2) - e_b(1,2))^2);
      a1 = 0.5*v*(t_b -t_a);
      ecc1 = abs(c1/a1);
      c2 = 0.5*sqrt((e_a(1,1)-e_c(1,1))^2 + (e_a(1,2) - e_c(1,2))^2);
      a2 = 0.5*v*(t_c - t_a);
      ecc2 = abs(c2/a2);
      A = (d_ab^2 + d_ac^2 - d_bc^2)/(2*d_ab*d_ac);

if ((ecc1 <= 1 | ecc2 <= 1))
      disp('Warning! At least one eccentricity is less than 1.');
pause(2);

end

% CASE #1: TWO HYPERBOLAS

% compute the intersection points first in polar coordinates

if (ecc1 > 1 & ecc2 > 1)
      B = sqrt(1 - A^2);

      alpha = c1/(c1^2 - a1^2) - c2*A/(c2^2 - a2^2);
      beta = c2*B/(c2^2 - a2^2);
      gamma = a2/(c2^2 - a2^2) - a1/(c1^2 - a1^2);

      costh1 = (alpha*gamma + beta*sqrt(alpha^2 + beta^2 -
                gamma^2))/(alpha^2 + beta^2);
      costh2 = (alpha*gamma - beta*sqrt(alpha^2 + beta^2 -
                gamma^2))/(alpha^2 + beta^2);

      r1 = (c1^2 - a1^2)/(c1*costh1 + a1);
      r2 = (c1^2 - a1^2)/(c1*costh2 + a1);

      % determine whether the angle is theta or 2 pi - theta

      eaxis = (e_b - e_a)/sqrt(dot(e_b-e_a,e_b-e_a));
      eoffaxis = (e_c - e_a)/sqrt(dot(e_c-e_a,e_c-e_a));

      if (eaxis(1,1) ~= 0)
            testperp = [-eaxis(1,2)/(eaxis(1,1)) 1];
            if (eaxis(1,1) > 0)
                  perpaxis = testperp / sqrt(dot(testperp,testperp));
```

```
      else
            perpaxis = - testperp /sqrt(dot(testperp,testperp));
      end
else
      if (eaxis(1,2) > 0)
            perpaxis = [-1 0];
      else
            perpaxis = [1 0];
      end
end
testvec = cross([eaxis(1,1) eaxis(1,2) 0], [eoffaxis(1,1)
          eoffaxis(1,2) 0]);

if (testvec(1,3) > 0)
      phi = acos(dot(eaxis,eoffaxis));
else
      phi = 2* pi - acos(dot(eaxis,eoffaxis));
end

if (r1 > 0 & imag(r1) == 0)
      d_theta1 = sqrt(r1^2 + d_ac^2 - 2*r1*d_ac*cos(acos(costh1)
                  - phi));
      d_2pimtheta1 = sqrt(r1^2 + d_ac^2 -
                        2*r1*d_ac*cos(acos(costh1) + phi));
      if (abs(v * (t_c - t_a) - (d_theta1-r1)) <
           abs(v * (t_c - t_a) - (d_2pimtheta1-r1)))
            theta1 = acos(costh1);

      else
            theta1 = 2 * pi - acos(costh1);

      end

      % now find estimated cartesian coordinates

      rvec1 = r1*[costh1 sin(theta1)];

      disp('the hyperbolae intersect at:');
      eloc1 = e_a + rvec1(1,1)*eaxis + rvec1(1,2)*perpaxis


      % compute the distance to the pacemaker

      disp('the distance to the pacemaker is: ');
      dist1 = sqrt(dot(eloc1-pmkr,eloc1-pmkr))

      pause(2);
end

% repeat for the other possible intersection point

if (r2 > 0 & imag(r2) == 0)
      d_theta2 = sqrt(r2^2 + d_ac^2 - 2*r2*d_ac*cos(acos(costh2)
                  - phi));
```

```
                d_2pimtheta2 = sqrt(r2^2 + d_ac^2 -
                                2*r2*d_ac*cos(acos(costh2) + phi));
                if (abs(v * (t_c - t_a) - (d_theta2-r2)) <
                     abs(v * (t_c - t_a) -(d_2pimtheta2-r2)))
                      theta2 = acos(costh2);

                else
                      theta2 = 2 * pi - acos(costh2);

                end

                % now find estimated coordinates

                rvec2 = r2*[costh2 sin(theta2)];

                disp('the hyperbolae intersect at:');
                eloc2 = e_a + rvec2(1,1)*eaxis + rvec2(1,2)*perpaxis

                % compute the distance to the pacemaker

                disp('the distance to the pacemaker is: ');
                dist2 = sqrt(dot(eloc2-pmkr,eloc2-pmkr))

                pause(2);
        end

        if (r1 > 0 & r2 > 0 & imag(r1) == 0 & imag(r2) == 0)
                disp('The hyperbolae intersect at two locations');
        end

        if ((r1 < 0 & r2 < 0) | (imag(r1) ~= 0 & imag(r2) ~= 0))
                disp('Localization failed: hyperbolae don't intersect');
                fail = 1;
        end

end

% CASE #2: ONE HYPERBOLA AND ONE LINE

if (ecc1 <= 1 & ecc2 > 1) disp('Warning: using only one hyperbola');
        eline3 = e_b - e_a;
        ehyp3 = e_c - e_a;
        costh3 =
dot(eline3,ehyp3)/(sqrt(dot(eline3,eline3))*sqrt(dot(ehyp3,ehyp3)));
        testvec3 = cross([ehyp3(1,1) ehyp3(1,2) 0], [eline3(1,1)
eline3(1,2) 0]);
        if (testvec3(1,3) > 0)
                r3 = (c2^2 - a2^2)/(-c2*costh3 + a2);

        else
                r3 = (c2^2 - a2^2)/(c2*costh3 + a2);

        end
```

```
        rvec3 = - r3 * eline3/sqrt(dot(eline3,eline3));

        disp('the estimated coordinates are (line + hyperbola):');
        eloc3 = e_a + rvec3

        % compute the distance to the pacemaker

        disp('the distance to the pacemaker is: ');
        dist3 = sqrt(dot(eloc3-pmkr,eloc3-pmkr))

        pause(2);
end

if (ecc2 <= 1 & ecc1 > 1) disp('Warning: using only one hyperbola');
        eline4 = e_c - e_a;
        ehyp4 = e_b - e_a;
        costh4 =
dot(eline4,ehyp4)/(sqrt(dot(eline4,eline4))*sqrt(dot(ehyp4,ehyp4)));
        testvec4 = cross([ehyp4(1,1) ehyp4(1,2) 0], [eline4(1,1)
eline4(1,2) 0]);
        if (testvec4(1,3) < 0)
                r4 = (c1^2 - a1^2)/(-c1*costh4 + a1);

        else
                r4 = (c1^2 - a1^2)/(c1*costh4 + a1);

        end

        rvec4 = - r4 * eline4/sqrt(dot(eline4,eline4));

        %disp('the estimated coordinates are (line + hyperbola):');
        eloc4 = e_a + rvec4

        % compute the distance to the pacemaker

        disp('the distance to the pacemaker is: ');
        dist4 = sqrt(dot(eloc4-pmkr,eloc4-pmkr))

        pause(2);
end

% plot the relative electrode positions and pacemaker estimate

% figure indicating loci

figure(1);axis([0 160 0 160]); axis square; hold;

plot(pmkr(1,1),pmkr(1,2),'*');
plot(e_a(1,1),e_a(1,2),'o');
plot(e_b(1,1),e_b(1,2),'o');
plot(e_c(1,1),e_c(1,2),'o');
```

```
if (fail == 0)
      if (ecc1 > 1 & ecc2 > 1)
            if (r1 > 0)
                  plot(eloc1(1,1),eloc1(1,2), '.');

            end
            if (r2 > 0)
                  plot(eloc2(1,1),eloc2(1,2), '.');

            end
      end

      if (ecc1 <= 1 & ecc2 > 1)
            plot(eloc3(1,1),eloc3(1,2), '.');

      end


      if (ecc2 <= 1 & ecc1 > 1)
            plot(eloc4(1,1),eloc4(1,2), '.');

      end
end

hold;
title('Pacemaker Localization (o = initial positions, . = pacemkr
estimate)');
xlabel('ROW'); ylabel('COLUMN');


% figure showing intersecting curves

figure(2); angle = (0:0.01:2 * pi);

% first get the angles right for plotting the electrode positions in
polar coordinates

if (eaxis(1,1) > 0 & eaxis(1,2) > 0)
      rot1 = atan(eaxis(1,2)/eaxis(1,1));
elseif (eaxis(1,1) < 0 & eaxis(1,2) > 0)
      rot1 = pi + atan(eaxis(1,2)/eaxis(1,1));
elseif (eaxis(1,1) < 0 & eaxis(1,2) < 0)
      rot1 = pi + atan(eaxis(1,2)/eaxis(1,1));
elseif (eaxis(1,1) > 0 & eaxis(1,2) < 0)
      rot1 = atan(eaxis(1,2)/eaxis(1,1));
elseif (eaxis(1,1) == 0 & eaxis(1,2) > 0)
      rot1 = pi/2;
elseif (eaxis(1,1) == 0 & eaxis(1,2) < 0)
      rot1 = 3 * pi/2;
elseif (eaxis(1,1) > 0 & eaxis(1,2) == 0)
      rot1 = 0;
elseif (eaxis(1,1) < 0 & eaxis(1,2) == 0)
      rot1 = pi;
end
```

```
if (eoffaxis(1,1) > 0 & eoffaxis(1,2) > 0)
      rot2 = atan(eoffaxis(1,2)/eoffaxis(1,1));
elseif (eoffaxis(1,1) < 0 & eoffaxis(1,2) > 0)
      rot2 = pi + atan(eoffaxis(1,2)/eoffaxis(1,1));
elseif (eoffaxis(1,1) < 0 & eoffaxis(1,2) < 0)
      rot2 = pi + atan(eoffaxis(1,2)/eoffaxis(1,1));
elseif (eoffaxis(1,1) > 0 & eoffaxis(1,2) < 0)
      rot2 = atan(eoffaxis(1,2)/eoffaxis(1,1));
elseif (eoffaxis(1,1) == 0 & eoffaxis(1,2) > 0)
      rot2 = pi/2;
elseif (eoffaxis(1,1) == 0 & eoffaxis(1,2) < 0)
      rot2 = 3 * pi/2;
elseif (eoffaxis(1,1) > 0 & eoffaxis(1,2) == 0)
      rot2 = 0;
elseif (eoffaxis(1,1) < 0 & eoffaxis(1,2) == 0)
      rot2 = pi;
end

% polar coordinate plot of hyperbolae

polar(rot2, 2*c2, 'o');hold; ax = axis; axis(2.5*ax);
polar(rot1,2*c1,'o'); polar(0,0,'o'); plot(pmkr-e_a(1,1),pmkr-
e_a(1,2),'*');

if (ecc1 > 1 & ecc2 > 1)
      polar(angle + rot1, (c1^2 - a1^2)./(c1*cos(angle) + a1),'r');
      polar(angle + rot1, (c2^2 - a2^2)./(c2*cos(angle-phi) +a2),'g');
end

if (ecc1 <= 1 & ecc2 > 1)
      polar((pi + rot1) * ones(1,1001), (0:0.1:100),'r');
      polar(angle + rot1, (c2^2 - a2^2)./(c2*cos(angle-phi) +a2),'g');
end

if (ecc2 <= 1 & ecc1 > 1)
      polar((rot2 + pi) * ones(1,1001), (0:0.1:100),'g');
      polar(angle + rot1, (c1^2 - a1^2)./(c1*cos(angle) + a1),'r');
end
hold;
```

APPENDIX D

The following Matlab source code performs the localization by resetting procedure from Chapter 6.

```
% This M-file uses localization by resetting to compute and plot the
% coordinates of an electrical source in a plane.

clear;

pmkr = input('input the PACEMAKER location "[row col]": ');
CL = input('input the CYCLE LENGTH of the rhythm: ');
CI = input('input the latest COUPLING INTERVAL giving resetting: ');

% input electrode positions

e1 = input('input coordinates of ELECTRODE e1 "[row col]": ');
e2 = input('input coordinates of ELECTRODE e2 "[row col]": ');
e3 = input('input coordinates of ELECTRODE e3 "[row col]": ');

% compute interelectrode distances

d12 = sqrt((e1(1,1)-e2(1,1))^2 + (e1(1,2) - e2(1,2))^2);
d13 = sqrt((e1(1,1)-e3(1,1))^2 + (e1(1,2) - e3(1,2))^2);
d23 = sqrt((e3(1,1)-e2(1,1))^2 + (e3(1,2) - e2(1,2))^2);

% input activation times and velocity estimate

t1 = input('input TIME of activation for e1: ');
t2 = input('input TIME of activation for e2: ');
t3 = input('input TIME of activation for e3: ');

v = input('input an estimate of the conduction VELOCITY: ');

% deterimine the electrode arrangement

ecc_12 = d12/(v* abs(t1 - t2));
ecc_13 = d13/(v* abs(t1 - t3));

if (ecc_12 > ecc_13)
      e_a = e1; t_a = t1;
      e_b = e2; t_b = t2;
      e_c = e3; t_c = t3;
      d_ab = d12; d_ac = d13; d_bc = d23;
else
      e_a = e1; t_a = t1;
      e_b = e3; t_b = t3;
      e_c = e2; t_c = t2;
      d_ab = d13; d_ac = d12; d_bc = d23;
```

```
end

% determine the distance to the pacemaker

r1 = 0.5 * v * CL * (1 - CI/CL);

% determine the hyperbola parameters

c1 = 0.5*d_ab;
a1 = 0.5*v*(t_b -t_a);

costh1 = (c1^2 - a1^2)/(c1*r1) - a1/c1;

% determine whether the angle is theta or 2 pi - theta

eaxis = (e_b - e_a)/sqrt(dot(e_b-e_a,e_b-e_a));
eoffaxis = (e_c - e_a)/sqrt(dot(e_c-e_a,e_c-e_a));

if (eaxis(1,1) ~= 0)
      testperp = [-eaxis(1,2)/(eaxis(1,1)) 1];
      if (eaxis(1,1) > 0)
            perpaxis = testperp / sqrt(dot(testperp,testperp));
      else
            perpaxis = - testperp / sqrt(dot(testperp,testperp));
      end
else
      if (eaxis(1,2) > 0)
            perpaxis = [-1 0];
      else
            perpaxis = [1 0];
      end
end

testvec = cross([eaxis(1,1) eaxis(1,2) 0], [eoffaxis(1,1)
eoffaxis(1,2) 0]);

if (testvec(1,3) > 0)
      phi = acos(dot(eaxis,eoffaxis));
else
      phi = 2* pi - acos(dot(eaxis,eoffaxis));
end


d_theta1 = sqrt(r1^2 + d_ac^2 - 2*r1*d_ac*cos(acos(costh1) - phi));
d_2pimtheta1 = sqrt(r1^2 + d_ac^2 - 2*r1*d_ac*cos(acos(costh1) +
phi));
if (abs(v * (t_c - t_a) - (d_theta1-r1)) < abs(v * (t_c - t_a) -
(d_2pimtheta1-r1)))
      theta1 = acos(costh1);

else
      theta1 = 2 * pi - acos(costh1);

end
```

```
% now find estimated cartesian coordinates

rvec1 = r1*[costh1 sin(theta1)];

disp('the estimated coordinates     of intersecting hyperbolae are:');
eloc1 = e_a + rvec1(1,1)*eaxis + rvec1(1,2)*perpaxis


% compute the distance to the pacemaker

disp('the distance to the pacemaker is: ');
dist1 = sqrt(dot(eloc1-pmkr,eloc1-pmkr))

pause(2);

% plot the relative electrode positions and pacemaker estimate

% figure indicating loci

figure(1);axis([0 80 0 80]); axis square; hold;

plot(pmkr(1,1),pmkr(1,2),'*');
plot(e_a(1,1),e_a(1,2),'o');
plot(e_b(1,1),e_b(1,2),'o');
plot(e_c(1,1),e_c(1,2),'o');

plot(eloc1(1,1),eloc1(1,2), '.');

hold;
title('Pacemaker Localization (o = initial positions, . = pacemkr
estimate)');
xlabel('ROW'); ylabel('COLUMN');


% figure showing intersecting curves

figure(2); angle = (0:0.01:2 * pi);

% first get the angles right for plotting the electrode positions in
polar coordinates

if (eaxis(1,1) > 0 & eaxis(1,2) > 0)
      rot1 = atan(eaxis(1,2)/eaxis(1,1));
elseif (eaxis(1,1) < 0 & eaxis(1,2) > 0)
      rot1 = pi + atan(eaxis(1,2)/eaxis(1,1));
elseif (eaxis(1,1) < 0 & eaxis(1,2) < 0)
      rot1 = pi + atan(eaxis(1,2)/eaxis(1,1));
elseif (eaxis(1,1) > 0 & eaxis(1,2) < 0)
      rot1 = atan(eaxis(1,2)/eaxis(1,1));
elseif (eaxis(1,1) == 0 & eaxis(1,2) > 0)
      rot1 = pi/2;
elseif (eaxis(1,1) == 0 & eaxis(1,2) < 0)
      rot1 = 3 * pi/2;
```

```
elseif (eaxis(1,1) > 0 & eaxis(1,2) == 0)
      rot1 = 0;
elseif (eaxis(1,1) < 0 & eaxis(1,2) == 0)
      rot1 = pi;
end

if (eoffaxis(1,1) > 0 & eoffaxis(1,2) > 0)
      rot2 = atan(eoffaxis(1,2)/eoffaxis(1,1));
elseif (eoffaxis(1,1) < 0 & eoffaxis(1,2) > 0)
      rot2 = pi + atan(eoffaxis(1,2)/eoffaxis(1,1));
elseif (eoffaxis(1,1) < 0 & eoffaxis(1,2) < 0)
      rot2 = pi + atan(eoffaxis(1,2)/eoffaxis(1,1));
elseif (eoffaxis(1,1) > 0 & eoffaxis(1,2) < 0)
      rot2 = atan(eoffaxis(1,2)/eoffaxis(1,1));
elseif (eoffaxis(1,1) == 0 & eoffaxis(1,2) > 0)
      rot2 = pi/2;
elseif (eoffaxis(1,1) == 0 & eoffaxis(1,2) < 0)
      rot2 = 3 * pi/2;
elseif (eoffaxis(1,1) > 0 & eoffaxis(1,2) == 0)
      rot2 = 0;
elseif (eoffaxis(1,1) < 0 & eoffaxis(1,2) == 0)
      rot2 = pi;
end

% polar coordinate plot of hyperbola and circle

polar(rot2, d_ac, 'o');hold; ax = axis; axis(2*ax);
polar(rot1,d_ab,'o'); polar(0,0,'o'); plot(pmkr-e_a(1,1),pmkr-
e_a(1,2),'*');


polar(angle + rot1, (c1^2 - a1^2)./(c1*cos(angle) + a1),'r');
polar(angle, r1*ones(1,629) ,'b');
hold;
```